Part II

Calculation and Measurement of Scattering and Absorption Characteristics of Small Particles

The scattering, absorption, and emission characteristics introduced in Part I are intimately related to the physical and geometrical parameters of particles such as size, shape, relative refractive index, and orientation. Therefore, understanding natural optical phenomena and developing remote sensing and laboratory techniques for particle characterization require accurate quantitative knowledge of the electromagnetic scattering interaction as a function of the particle parameters.

Electromagnetic scattering properties of small particles can be either computed theoretically or measured experimentally, both approaches having their strengths, weaknesses, and limitations. Theoretical modeling does not involve expensive instrumentation, can be used to find any scattering characteristic, and often allows switching to another particle shape, size, refractive index, or orientation by changing a few lines in a computer code. However, applying exact methods to realistic polydispersions of irregular particles can be very costly, and sometimes not even possible, and often must be replaced by computations for simplified model shapes. Approximate techniques can be more flexible, but often have poorly characterized accuracy and range of applicability.

Laboratory and field measurements employing visible or infrared light can deal with real small particles, either natural or artificial. However, such measurements require complex and expensive hardware, are often incapable of providing simultaneously and accurately all scattering characteristics, and may be difficult to interpret because of lack of independent information on sample microphysics and composition. The microwave analog technique allows a much greater degree of independent sample characterization and enables true controlled laboratory measurements, but it involves even costlier equipment and cannot be applied readily to realistic distributions of particle sizes, shapes, and orientations. It is thus clear that only a creative combination of various theoretical and experimental approaches can lead to a significantly improved knowledge of light scattering by small particles.

All exact techniques for calculating electromagnetic scattering are based on solving the differential Maxwell equations or their integral counterparts in the time or frequency domain, either analytically or numerically. The search for an analytical solution has been equated, traditionally, to solving the vector wave equations for the time-harmonic electric fields outside and inside the scatterer (Eqs. (2.3) and (2.4)) using the separation of variables technique in one of the few coordinate systems in which this type of equation is separable (Morse and Feshbach 1953). The incident and internal fields are expanded in wave functions that are regular inside the scatterer, whereas the external scattered field is expanded in wave functions that behave as outgoing waves at infinity. These expansions are double series in general; a reduction to single series occurs only for spheres and infinite cylinders. Subject to the requirement of continuity of the tangential component of the electric and magnetic fields at the particle boundary (Eqs. (1.13) and (1.15)), the unknown coefficients in the internal-field and scattered-field expansions are determined from the known expansion coefficients of the incident field.

Unfortunately, the separation of variables technique generates a manageable solution only in a few simple cases. Lorenz in 1890 and, independently, Love (1899), Mie

(1908), and Debye (1909) derived the solution for an isotropic homogeneous sphere (see the historical remarks in Section 3.4 of Kerker 1969). We will refer to this solution as the Lorenz–Mie theory. This approach was extended to concentric core-mantle spheres (Aden and Kerker 1951), concentric multilayered spheres (Wait 1963), and radially inhomogeneous spheres (Wyatt 1962). Wait (1955) gave a full solution for electromagnetic scattering by a homogeneous infinite circular cylinder, whereas Kim and Yeh (1991) solved the general problem for an infinite elliptical cylinder. Finally, Oguchi (1973), Asano and Yamamoto (1975), and Onaka (1980) derived a general solution for homogeneous and core-mantle spheroids.

It is unlikely that this list of exact analytical results will be extended significantly in the future. Indeed, the separation of variables solution for spheroids, perhaps the simplest finite nonspherical particle, is already so complex that it behaves like a numerical solution in many respects and offers no definitive practical advantage over other available approaches. Some exact numerical approaches, in turn, often behave like analytical solutions since they involve the expansion of the incident and scattered fields in complete sets of eigenfunctions with well-known and convenient mathematical properties. As a consequence, the formerly rigid distinction between exact analytical and numerical solutions for nonspherical particles has become semantic rather than practical.

In Part II of this book we describe several theoretical and experimental techniques that have found extensive practical usage. We begin with a chapter on the T-matrix method because this is one of the most efficient, accurate, and widely employed exact techniques for simple and aggregated particles, includes the Lorenz–Mie theory as a particular case, and has remarkable analytical ties with the formalism outlined in Sections 4.10–4.12. In Chapters 6 and 7 we describe several alternative exact techniques and approximations and compare their relative performance and ranges of applicability. The closing chapter of Part II is devoted to experimental techniques employing visible, infrared, or microwave wavelengths.

Chapter 5

T-matrix method and Lorenz–Mie theory

The *T*-matrix method was initially introduced by Waterman (1965, 1971) as a technique for computing electromagnetic scattering by single, homogeneous, arbitrarily shaped particles based on the Huygens principle (this technique is otherwise known as the extended boundary condition method, the Schelkunoff equivalent current method, the Ewald–Oseen extinction theorem, and the null-field method). However, the concept, perceived at the time as auxiliary, of expanding the incident and scattered waves in appropriate vector spherical wave functions and relating these expansions by means of a transition (or *T*) matrix has proved to be extremely powerful by itself and has dramatically expanded the realm of the *T*-matrix approach. The latter now includes electromagnetic, acoustic, and elastodynamic wave scattering by single and aggregated scatterers, multiple scattering in discrete random media, and scattering by gratings and periodically rough surfaces (Varadan and Varadan 1980; Tsang *et al.* 1985). An attractive feature of the *T*-matrix approach is that it reduces exactly to the Lorenz–Mie theory when the scattering particle is a homogeneous or layered sphere composed of isotropic materials. The analyticity of the *T*-matrix formulation reveals close mathematical ties with the formalism of expanding normalized scattering matrices in generalized spherical functions (Sections 4.11 and 4.12) and has led to the development of efficient techniques for calculating orientation-averaged scattering characteristics.

At present, the *T*-matrix approach is one of the most powerful and widely used tools for rigorously computing electromagnetic scattering by single and compounded particles. In many applications it surpasses other frequently used techniques in terms of efficiency and size parameter range and is the only method that has been used in systematic surveys of nonspherical scattering based on calculations for thousands of particles in random orientation. Recent improvements have made this method applicable to particles much

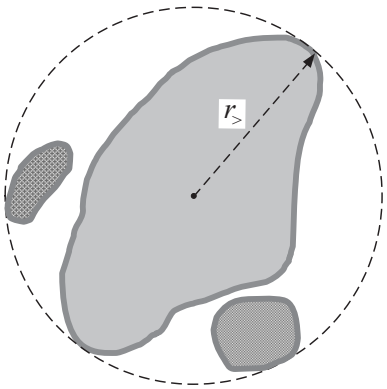

Figure 5.1. Cross section of an arbitrarily shaped, finite scattering object. $r_>$ is the radius of the smallest circumscribing sphere centered at the origin of the laboratory coordinate system.

larger than a wavelength and, therefore, suitable for checking the accuracy of the geometrical optics approximation and its modifications at lower frequencies (Section 7.4). Because of its high and readily controllable numerical accuracy, the *T*-matrix method is one of a very few sources of benchmark results for particles lacking spherical symmetry. Hence it appears natural to open Part II by a detailed survey of the *T*-matrix approach.

5.1 *T*-matrix ansatz

Consider scattering of a plane electromagnetic wave

$$\mathbf{E}^{\rm inc}(\mathbf{r}) = \mathbf{E}_0^{\rm inc} \exp(ik_1 \hat{\mathbf{n}}^{\rm inc} \cdot \mathbf{r}), \qquad \mathbf{E}_0^{\rm inc} \cdot \hat{\mathbf{n}}^{\rm inc} = 0, \tag{5.1}$$

by an arbitrary finite scattering object in the form of a single particle or a fixed aggregate, as described in Chapter 2. We expand the incident and scattered fields in vector spherical wave functions as follows:

$$\mathbf{E}^{\rm inc}(\mathbf{r}) = \sum_{n=1}^{\infty} \sum_{m=-n}^{n} [a_{mn} {\rm Rg}\mathbf{M}_{mn}(k_1\mathbf{r}) + b_{mn} {\rm Rg}\mathbf{N}_{mn}(k_1\mathbf{r})], \tag{5.2}$$

$$\mathbf{E}^{\rm sca}(\mathbf{r}) = \sum_{n=1}^{\infty} \sum_{m=-n}^{n} [p_{mn}\mathbf{M}_{mn}(k_1\mathbf{r}) + q_{mn}\mathbf{N}_{mn}(k_1\mathbf{r})], \qquad r > r_>, \tag{5.3}$$

where k_1 is the wave number in the surrounding medium and $r_>$ is the radius of the smallest circumscribing sphere of the scatterer centered at the origin of the laboratory coordinate system (Fig. 5.1). The properties of the vector spherical wave functions are summarized in Appendix C. The functions ${\rm Rg}\mathbf{M}_{mn}$ and ${\rm Rg}\mathbf{N}_{mn}$ are regular (finite) at the origin, while the use of the outgoing functions $\mathbf{M}_{mn}$ and $\mathbf{N}_{mn}$ in Eq. (5.3) ensures that the scattered field satisfies the so-called radiation condition at infinity (i.e., the transverse component of the scattered electric field decays as $1/r$, whereas

the radial component decays faster than $1/r$ with $r \to \infty$; see Section 2.2 and Eqs. (C.30) and (C.31)). The requirement $r > r_>$ in Eq. (5.3) means that the scattered field is expanded in the functions $\mathbf{M}_{mn}$ and $\mathbf{N}_{mn}$ only outside the smallest circumscribing sphere of the scatterer (Fig. 5.1). The so-called Rayleigh hypothesis (e.g., Bates 1975; Paulick 1990) conjectures that the scattered field can be expanded in the outgoing wave functions not only in the outside region but also in the region between the particle surface and the smallest circumscribing sphere. Because the range of validity of this hypothesis is poorly known and is in fact questionable, the requirement $r > r_>$ in Eq. (5.3) is important in order to make sure that the Rayleigh hypothesis is not implicitly invoked (Lewin 1970).

The expansion coefficients of the plane incident wave are given by Eqs. (C.57) and (C.58):

$$a_{mn} = 4\pi(-1)^m \mathrm{i}^n d_n \mathbf{E}_0^{\mathrm{inc}} \cdot \mathbf{C}_{mn}^*(\vartheta^{\mathrm{inc}}) \exp(-\mathrm{i}m\varphi^{\mathrm{inc}}), \tag{5.4}$$

$$b_{mn} = 4\pi(-1)^m \mathrm{i}^{n-1} d_n \mathbf{E}_0^{\mathrm{inc}} \cdot \mathbf{B}_{mn}^*(\vartheta^{\mathrm{inc}}) \exp(-\mathrm{i}m\varphi^{\mathrm{inc}}). \tag{5.5}$$

Owing to the linearity of the Maxwell equations and constitutive relations (see Section 2.2), the relation between the scattered-field expansion coefficients p_{mn} and q_{mn} on the one hand and the incident field expansion coefficients a_{mn} and b_{mn} on the other hand must be linear and is given by the so-called transition matrix (or T matrix) $\mathbf{T}$ as follows (Waterman 1971; Tsang *et al.* 1985):

$$p_{mn} = \sum_{n'=1}^{\infty} \sum_{m'=-n'}^{n'} (T_{mnm'n'}^{11} a_{m'n'} + T_{mnm'n'}^{12} b_{m'n'}), \tag{5.6}$$

$$q_{mn} = \sum_{n'=1}^{\infty} \sum_{m'=-n'}^{n'} (T_{mnm'n'}^{21} a_{m'n'} + T_{mnm'n'}^{22} b_{m'n'}). \tag{5.7}$$

In compact matrix notation, Eqs. (5.6) and (5.7) can be rewritten as

$$\begin{bmatrix} \mathbf{p} \\ \mathbf{q} \end{bmatrix} = \mathbf{T} \begin{bmatrix} \mathbf{a} \\ \mathbf{b} \end{bmatrix} = \begin{bmatrix} \mathbf{T}^{11} & \mathbf{T}^{12} \\ \mathbf{T}^{21} & \mathbf{T}^{22} \end{bmatrix} \begin{bmatrix} \mathbf{a} \\ \mathbf{b} \end{bmatrix}, \tag{5.8}$$

which means that the column vector of the expansion coefficients of the scattered field is obtained by multiplying the T matrix and the column vector of the expansion coefficients of the incident field.

Equation (5.8) is the cornerstone of the T-matrix approach. Indeed, if the T matrix is known, then Eqs. (5.6), (5.7), (5.4), (5.5), and (5.3) give the scattered field and, thus, the scattering dyad defined by Eq. (2.26). Indeed, substituting the asymptotic formulas (C.30) and (C.31) in Eq. (5.3) yields Eq. (2.24) with

$$\mathbf{E}_1^{\mathrm{sca}}(\hat{\mathbf{n}}^{\mathrm{sca}}) = \frac{1}{k_1} \sum_{n=1}^{\infty} \sum_{m=-n}^{n} \mathrm{i}^{-n} \gamma_{mn} [-\mathrm{i}p_{mn} \mathbf{C}_{mn}(\vartheta^{\mathrm{sca}}, \varphi^{\mathrm{sca}}) + q_{mn} \mathbf{B}_{mn}(\vartheta^{\mathrm{sca}}, \varphi^{\mathrm{sca}})]. \tag{5.9}$$

Finally, using Eqs. (5.4)–(5.7), we easily derive

$$\ddot{A}(\hat{\mathbf{n}}^{\rm sca},\hat{\mathbf{n}}^{\rm inc})=\frac{4\pi}{k_1}\sum_{nmn'm'}{\rm i}^{n'-n-1}(-1)^{m+m'}d_n d_{n'}\exp[{\rm i}(m\varphi^{\rm sca}-m'\varphi^{\rm inc})]$$
$$\times\{[T^{11}_{mnm'n'}\mathbf{C}_{mn}(\vartheta^{\rm sca})+{\rm i}T^{21}_{mnm'n'}\mathbf{B}_{mn}(\vartheta^{\rm sca})]\otimes\mathbf{C}^*_{m'n'}(\vartheta^{\rm inc})$$
$$+[-{\rm i}T^{12}_{mnm'n'}\mathbf{C}_{mn}(\vartheta^{\rm sca})+T^{22}_{mnm'n'}\mathbf{B}_{mn}(\vartheta^{\rm sca})]\otimes\mathbf{B}^*_{m'n'}(\vartheta^{\rm inc})\}. \tag{5.10}$$

Equations (2.31)–(2.34) and (5.10) then yield the amplitude matrix elements as follows:

$$S_{11}(\hat{\mathbf{n}}^{\rm sca},\hat{\mathbf{n}}^{\rm inc})=\frac{1}{k_1}\sum_{n=1}^{\infty}\sum_{n'=1}^{\infty}\sum_{m=-n}^{n}\sum_{m'=-n'}^{n'}\alpha_{mnm'n'}[T^{11}_{mnm'n'}\pi_{mn}(\vartheta^{\rm sca})\pi_{m'n'}(\vartheta^{\rm inc})$$
$$+T^{21}_{mnm'n'}\tau_{mn}(\vartheta^{\rm sca})\pi_{m'n'}(\vartheta^{\rm inc})+T^{12}_{mnm'n'}\pi_{mn}(\vartheta^{\rm sca})\tau_{m'n'}(\vartheta^{\rm inc})$$
$$+T^{22}_{mnm'n'}\tau_{mn}(\vartheta^{\rm sca})\tau_{m'n'}(\vartheta^{\rm inc})]\exp[{\rm i}(m\varphi^{\rm sca}-m'\varphi^{\rm inc})], \tag{5.11}$$

$$S_{12}(\hat{\mathbf{n}}^{\rm sca},\hat{\mathbf{n}}^{\rm inc})=\frac{1}{{\rm i}k_1}\sum_{n=1}^{\infty}\sum_{n'=1}^{\infty}\sum_{m=-n}^{n}\sum_{m'=-n'}^{n'}\alpha_{mnm'n'}[T^{11}_{mnm'n'}\pi_{mn}(\vartheta^{\rm sca})\tau_{m'n'}(\vartheta^{\rm inc})$$
$$+T^{21}_{mnm'n'}\tau_{mn}(\vartheta^{\rm sca})\tau_{m'n'}(\vartheta^{\rm inc})+T^{12}_{mnm'n'}\pi_{mn}(\vartheta^{\rm sca})\pi_{m'n'}(\vartheta^{\rm inc})$$
$$+T^{22}_{mnm'n'}\tau_{mn}(\vartheta^{\rm sca})\pi_{m'n'}(\vartheta^{\rm inc})]\exp[{\rm i}(m\varphi^{\rm sca}-m'\varphi^{\rm inc})], \tag{5.12}$$

$$S_{21}(\hat{\mathbf{n}}^{\rm sca},\hat{\mathbf{n}}^{\rm inc})=\frac{\rm i}{k_1}\sum_{n=1}^{\infty}\sum_{n'=1}^{\infty}\sum_{m=-n}^{n}\sum_{m'=-n'}^{n'}\alpha_{mnm'n'}[T^{11}_{mnm'n'}\tau_{mn}(\vartheta^{\rm sca})\pi_{m'n'}(\vartheta^{\rm inc})$$
$$+T^{21}_{mnm'n'}\pi_{mn}(\vartheta^{\rm sca})\pi_{m'n'}(\vartheta^{\rm inc})+T^{12}_{mnm'n'}\tau_{mn}(\vartheta^{\rm sca})\tau_{m'n'}(\vartheta^{\rm inc})$$
$$+T^{22}_{mnm'n'}\pi_{mn}(\vartheta^{\rm sca})\tau_{m'n'}(\vartheta^{\rm inc})]\exp[{\rm i}(m\varphi^{\rm sca}-m'\varphi^{\rm inc})], \tag{5.13}$$

$$S_{22}(\hat{\mathbf{n}}^{\rm sca},\hat{\mathbf{n}}^{\rm inc})=\frac{1}{k_1}\sum_{n=1}^{\infty}\sum_{n'=1}^{\infty}\sum_{m=-n}^{n}\sum_{m'=-n'}^{n'}\alpha_{mnm'n'}[T^{11}_{mnm'n'}\tau_{mn}(\vartheta^{\rm sca})\tau_{m'n'}(\vartheta^{\rm inc})$$
$$+T^{21}_{mnm'n'}\pi_{mn}(\vartheta^{\rm sca})\tau_{m'n'}(\vartheta^{\rm inc})+T^{12}_{mnm'n'}\tau_{mn}(\vartheta^{\rm sca})\pi_{m'n'}(\vartheta^{\rm inc})$$
$$+T^{22}_{mnm'n'}\pi_{mn}(\vartheta^{\rm sca})\pi_{m'n'}(\vartheta^{\rm inc})]\exp[{\rm i}(m\varphi^{\rm sca}-m'\varphi^{\rm inc})], \tag{5.14}$$

where

$$\alpha_{mnm'n'}={\rm i}^{n'-n-1}(-1)^{m+m'}\left[\frac{(2n+1)(2n'+1)}{n(n+1)n'(n'+1)}\right]^{1/2}, \tag{5.15}$$

$$\pi_{mn}(\vartheta)=\frac{md^n_{0m}(\vartheta)}{\sin\vartheta},\qquad \pi_{-mn}(\vartheta)=(-1)^{m+1}\pi_{mn}(\vartheta), \tag{5.16}$$

$$\tau_{mn}(\vartheta)=\frac{{\rm d}d^n_{0m}(\vartheta)}{{\rm d}\vartheta},\qquad \tau_{-mn}(\vartheta)=(-1)^m\tau_{mn}(\vartheta) \tag{5.17}$$

(see Eq. (B.5)). Knowledge of the amplitude matrix allows one to compute any of the scattering characteristics introduced in Chapter 2. Specifically, the Stokes phase and extinction matrices and the extinction cross section are given by Eqs. (2.106)–(2.121),

Eqs. (2.140)–(2.146), and Eq. (2.159), respectively. Alternatively, Eqs. (2.157), (5.9), (5.4) and (5.5) yield

$$C_{\rm ext} = -\frac{1}{k_1^2 |\mathbf{E}_0^{\rm inc}|^2} \,{\rm Re} \sum_{n=1}^{\infty} \sum_{m=-n}^{n} [a_{mn} (p_{mn})^* + b_{mn} (q_{mn})^*]. \tag{5.18a}$$

The formula for the scattering cross section follows from Eqs. (2.158) and (5.9) and the orthogonality and normalization conditions for the vector spherical harmonics, Eqs. (C.51) and (C.52):

$$\begin{aligned} C_{\rm sca} &= \frac{1}{|\mathbf{E}_0^{\rm inc}|^2} \int_0^{2\pi} {\rm d}\varphi^{\rm sca} \int_0^{\pi} {\rm d}\vartheta^{\rm sca} \sin\vartheta^{\rm sca} |\mathbf{E}_1^{\rm sca}(\vartheta^{\rm sca}, \varphi^{\rm sca})|^2 \\ &= \frac{1}{k_1^2 |\mathbf{E}_0^{\rm inc}|^2} \sum_{n=1}^{\infty} \sum_{m=-n}^{n} [|p_{mn}|^2 + |q_{mn}|^2]. \end{aligned} \tag{5.18b}$$

A fundamental feature of the *T*-matrix approach is that the *T* matrix depends only on the physical and geometrical characteristics of the scattering particle (such as particle size relative to the wavelength, shape (morphology), relative refractive index, and orientation with respect to the laboratory reference frame; see subsection 5.8.2 below) and is completely independent of the propagation directions and polarization states of the incident and scattered fields. This means that the *T* matrix need be computed only once and then can be used in calculations for any direction of incidence and scattering and for any polarization state of the incident field.

5.2 General properties of the *T* matrix

The special functions appearing in the *T*-matrix formulation have been studied thoroughly and result in convenient mathematical properties and symmetries of the *T* matrix. In this and later sections we will demonstrate how the analyticity of the *T*-matrix approach can be exploited in order to enhance significantly the efficiency of computations for individual scatterers as well as for particle ensembles.

5.2.1 Rotation transformation rule

We begin by deriving the rotation transformation rule for the *T* matrix. Consider laboratory (L) and particle (P) coordinate systems having a common origin inside the scattering object. Let α, β, and γ be the Euler angles of rotation transforming the laboratory coordinate system into the particle coordinate system (cf. Section 2.4), and let (ϑ_L, φ_L) and (ϑ_P, φ_P) be the spherical angles of the same position vector $\mathbf{r}$ in the two coordinate systems, respectively. We now rewrite Eqs. (5.2) and (5.3) as follows:

$$\mathbf{E}^{\rm inc}(\mathbf{r}) = \sum_{n=1}^{\infty} \sum_{m=-n}^{n} [a_{mn}(L) {\rm Rg}\mathbf{M}_{mn}(k_1 r, \vartheta_L, \varphi_L) + b_{mn}(L) {\rm Rg}\mathbf{N}_{mn}(k_1 r, \vartheta_L, \varphi_L)], \tag{5.19}$$

$$\mathbf{E}^{\rm sca}(\mathbf{r}) = \sum_{n=1}^{\infty}\sum_{m=-n}^{n}[p_{mn}(L)\mathbf{M}_{mn}(k_1 r, \vartheta_L, \varphi_L) + q_{mn}(L)\mathbf{N}_{mn}(k_1 r, \vartheta_L, \varphi_L)], \quad r > r_>, \tag{5.20}$$

$$\mathbf{E}^{\rm inc}(\mathbf{r}) = \sum_{n=1}^{\infty}\sum_{m=-n}^{n}[a_{mn}(P)\mathrm{Rg}\mathbf{M}_{mn}(k_1 r, \vartheta_P, \varphi_P) + b_{mn}(P)\mathrm{Rg}\mathbf{N}_{mn}(k_1 r, \vartheta_P, \varphi_P)], \tag{5.21}$$

$$\mathbf{E}^{\rm sca}(\mathbf{r}) = \sum_{n=1}^{\infty}\sum_{m=-n}^{n}[p_{mn}(P)\mathbf{M}_{mn}(k_1 r, \vartheta_P, \varphi_P) + q_{mn}(P)\mathbf{N}_{mn}(k_1 r, \vartheta_P, \varphi_P)], \quad r > r_>. \tag{5.22}$$

According to Eqs. (C.64) and (C.65), we can use Wigner D-functions to write

$$\mathbf{M}_{mn}(k_1 r, \vartheta_P, \varphi_P) = \sum_{m'=-n}^{n}\mathbf{M}_{m'n}(k_1 r, \vartheta_L, \varphi_L)D^n_{m'm}(\alpha, \beta, \gamma), \tag{5.23}$$

$$\mathbf{M}_{mn}(k_1 r, \vartheta_L, \varphi_L) = \sum_{m'=-n}^{n}\mathbf{M}_{m'n}(k_1 r, \vartheta_P, \varphi_P)D^n_{m'm}(-\gamma, -\beta, -\alpha), \tag{5.24}$$

and similarly for Rg$\mathbf{M}$, $\mathbf{N}$, and Rg$\mathbf{N}$. Therefore, we immediately get

$$\begin{matrix} a_{mn}(P) \\ b_{mn}(P) \end{matrix} = \sum_{m'=-n}^{n}\begin{matrix} a_{m'n}(L) \\ b_{m'n}(L) \end{matrix} D^n_{mm'}(-\gamma, -\beta, -\alpha), \tag{5.25}$$

$$\begin{matrix} p_{mn}(L) \\ q_{mn}(L) \end{matrix} = \sum_{m'=-n}^{n}\begin{matrix} p_{m'n}(P) \\ q_{m'n}(P) \end{matrix} D^n_{mm'}(\alpha, \beta, \gamma). \tag{5.26}$$

Note that in Eqs. (5.25) and (5.26) we use a compact way of writing two formulas (for a_{mn} and b_{mn} and for p_{mn} and q_{mn}) as a single equation. Finally, from

$$\begin{bmatrix} \mathbf{p}(P) \\ \mathbf{q}(P) \end{bmatrix} = \begin{bmatrix} \mathbf{T}^{11}(P) & \mathbf{T}^{12}(P) \\ \mathbf{T}^{21}(P) & \mathbf{T}^{22}(P) \end{bmatrix}\begin{bmatrix} \mathbf{a}(P) \\ \mathbf{b}(P) \end{bmatrix}, \tag{5.27}$$

$$\begin{bmatrix} \mathbf{p}(L) \\ \mathbf{q}(L) \end{bmatrix} = \begin{bmatrix} \mathbf{T}^{11}(L;\alpha,\beta,\gamma) & \mathbf{T}^{12}(L;\alpha,\beta,\gamma) \\ \mathbf{T}^{21}(L;\alpha,\beta,\gamma) & \mathbf{T}^{22}(L;\alpha,\beta,\gamma) \end{bmatrix}\begin{bmatrix} \mathbf{a}(L) \\ \mathbf{b}(L) \end{bmatrix}, \tag{5.28}$$

and Eqs. (5.25) and (5.26), we derive (Tsang *et al.* 1985)

$$T^{kl}_{mnm'n'}(L;\alpha,\beta,\gamma) = \sum_{m_1=-n}^{n}\sum_{m_2=-n'}^{n'} D^n_{mm_1}(\alpha,\beta,\gamma)T^{kl}_{m_1 n m_2 n'}(P)\,D^{n'}_{m_2 m'}(-\gamma,-\beta,-\alpha), \quad k,l = 1,2. \tag{5.29}$$

When $\alpha = \beta = \gamma = 0$, Eq. (5.29) must give

$$T^{kl}_{mnm'n'}(L;0,0,0) \equiv T^{kl}_{mnm'n'}(P). \tag{5.30}$$

It is easy to verify that this identity indeed follows from Eqs. (B.38) and (B.6).

If we now assume that the matrix $\mathbf{T}(P)$ is already known and use the Euler angles of rotation α, β, and γ to specify the orientation of the particle with respect to the laboratory coordinate system, then Eq. (5.29) gives the T matrix in the laboratory co-

ordinate system. Therefore, Eqs. (5.11)–(5.14) and (5.29) are ideally suited for computing analytically orientation-averaged scattering characteristics using a single precalculated $\mathbf{T}(P)$ matrix (see Sections 5.3–5.6 below).

5.2.2 Symmetry relations

According to the reciprocity relation (2.64), we must have

$$\begin{aligned}&\mathbf{S}(\pi-\vartheta^{\rm inc},\pi+\varphi^{\rm inc};\pi-\vartheta^{\rm sca},\pi+\varphi^{\rm sca})\\&=\begin{bmatrix}S_{11}(\vartheta^{\rm sca},\varphi^{\rm sca};\vartheta^{\rm inc},\varphi^{\rm inc}) & -S_{21}(\vartheta^{\rm sca},\varphi^{\rm sca};\vartheta^{\rm inc},\varphi^{\rm inc})\\ -S_{12}(\vartheta^{\rm sca},\varphi^{\rm sca};\vartheta^{\rm inc},\varphi^{\rm inc}) & S_{22}(\vartheta^{\rm sca},\varphi^{\rm sca};\vartheta^{\rm inc},\varphi^{\rm inc})\end{bmatrix}.\end{aligned} \tag{5.31}$$

Equations (5.16), (5.17), (B.7), and (B.25) give

$$\pi_{mn}(\pi-\vartheta)=(-1)^{n+1}\pi_{-mn}(\vartheta), \tag{5.32}$$

$$\tau_{mn}(\pi-\vartheta)=(-1)^{n+1}\tau_{-mn}(\vartheta). \tag{5.33}$$

Using Eqs. (5.11)–(5.15) and (5.32)–(5.33), it is straightforward to show that for Eq. (5.31) to be valid for any $\vartheta^{\rm inc}$, $\varphi^{\rm inc}$, $\vartheta^{\rm sca}$, and $\varphi^{\rm sca}$, the T matrix must obey the following general symmetry relation:

$$T^{lk}_{-m'n',-mn}=(-1)^{m+m'}T^{kl}_{mnm'n'},\quad k,l=1,2 \tag{5.34}$$

(Waterman 1971).

An appropriate choice of the particle reference frame can often result in useful symmetries of the $\mathbf{T}(P)$ matrix. For example, the z-axis of the particle coordinate system for a rotationally symmetric body should be directed along the axis of rotation. Because any rotation about the symmetry axis gives the same particle, we must have

$$T^{kl}_{mnm'n'}(L;\alpha,0,0)\equiv T^{kl}_{mnm'n'}(L;0,0,0)=T^{kl}_{mnm'n'}(P), \tag{5.35}$$

which, in view of Eqs. (5.29), (B.38), and (B.6), gives

$$T^{kl}_{mnm'n'}(P)=\delta_{mm'}T^{kl}_{mnmn'}(P). \tag{5.36}$$

Thus, the T matrix becomes diagonal with respect to the azimuthal indices m and m'. If the axis of rotation is directed along the z-axis of the laboratory reference frame, then mirroring the particle with respect to the xz-plane gives the same particle; therefore, the amplitude matrix $\mathbf{S}(\vartheta^{\rm sca},0;\vartheta^{\rm inc},0)$ must be diagonal (see Eq. (4.2c)). We thus have from Eqs. (5.12), (5.13), (5.16), (5.17), (5.30), and (5.36)

$$T^{kl}_{-mn,-mn'}(P)=(-1)^{k+l}T^{kl}_{mnmn'}(P),\qquad T^{12}_{0n0n'}(P)\equiv 0,\qquad T^{21}_{0n0n'}(P)\equiv 0. \tag{5.37}$$

Furthermore, if the rotationally symmetric particle has a plane of symmetry perpendicular to the axis of rotation, then rotating the particle through an angle π around the y-axis of the laboratory reference frame gives the same particle, and we must have

$$T^{kl}_{mnm'n'}(L;\,0,\,\pi,\,0) \equiv T^{kl}_{mnm'n'}(L;\,0,\,0,\,0) = T^{kl}_{mnm'n'}(P). \tag{5.38}$$

Equations (5.29), (B.38), (B.6), (B.7), and (5.36)–(5.38) then imply that

$$T^{11}_{mnmn'}(P) = T^{22}_{mnmn'}(P) = 0 \quad \text{unless} \quad (-1)^{n+n'} = 1 \tag{5.39}$$

and

$$T^{12}_{mnmn'}(P) = T^{21}_{mnmn'}(P) = 0 \quad \text{unless} \quad (-1)^{n+n'} = -1. \tag{5.40}$$

Any rotation of a spherically symmetric particle renders the same particle, and we must have

$$T^{kl}_{mnm'n'}(L;\,\alpha,\,\beta,\,\gamma) \equiv T^{kl}_{mnm'n'}(L;\,0,\,0,\,0) = T^{kl}_{mnm'n'}(P). \tag{5.41}$$

Equations (5.29), (5.36), (5.37), and (B.47) then force us to conclude that the $\mathbf{T}(P)$ matrix for a spherically symmetric scatterer must be diagonal and independent of the azimuthal indices m and m':

$$T^{12}_{mnm'n'}(P) \equiv 0, \quad T^{21}_{mnm'n'}(P) \equiv 0, \tag{5.42}$$

$$T^{11}_{mnm'n'}(P) = -\delta_{mm'}\delta_{nn'}b_n, \tag{5.43}$$

$$T^{22}_{mnm'n'}(P) = -\delta_{mm'}\delta_{nn'}a_n. \tag{5.44}$$

We will see later that the quantities a_n and b_n coincide with expansion coefficients appearing in the Lorenz–Mie solution for homogeneous or radially inhomogeneous spheres. It is, therefore, natural to refer to these quantities as Lorenz–Mie coefficients.

The analytical symmetry relations for the T matrix can be used to test numerical codes as well as to simplify considerably many equations of the T-matrix method and develop efficient numerical procedures. Additional properties of the T matrix for particles with specific symmetries are discussed in Schulz *et al.* (1999a) and in Kahnert *et al.* (2001a).

5.2.3 Unitarity

We will now derive the unitarity property of the T matrix for nonabsorbing scatterers (i.e., with the imaginary part of the relative refractive index equal to zero) as a consequence of energy conservation. We begin by defining the so-called S matrix $\boldsymbol{S}$:

$$\boldsymbol{S} = \mathbf{E} + 2\mathbf{T} = \mathbf{E} + 2\begin{bmatrix} \mathbf{T}^{11} & \mathbf{T}^{12} \\ \mathbf{T}^{21} & \mathbf{T}^{22} \end{bmatrix}, \tag{5.45}$$

where $\mathbf{E}$ is a unit matrix. (Note that we use a sloping $\boldsymbol{S}$ to distinguish the S matrix from the amplitude matrix $\mathbf{S}$.) As follows from Eqs. (C.1) and (C.2), we can write

$$\begin{matrix} \mathrm{Rg}\mathbf{M}_{mn} \\ \mathrm{Rg}\mathbf{N}_{mn} \end{matrix}(k_1 r,\,\vartheta,\,\varphi) = \frac{1}{2}\left[\begin{matrix} \mathbf{M}_{mn} \\ \mathbf{N}_{mn} \end{matrix}(k_1 r,\,\vartheta,\,\varphi) + \begin{matrix} \mathbf{M}^{(2)}_{mn} \\ \mathbf{N}^{(2)}_{mn} \end{matrix}(k_1 r,\,\vartheta,\,\varphi) \right], \tag{5.46}$$

where the superscript (2) labels vector spherical wave functions given by Eqs. (C.14) and (C.15) but with $h_n^{(1)}(\mathrm{k}r)$ replaced by $h_n^{(2)}(\mathrm{k}r)$. The total electric field is the vector sum of the incident and scattered fields. From Eqs. (5.2), (5.3), (5.6), (5.7), (5.45), and (5.46), we obtain

$$\begin{aligned}\mathbf{E}(\mathbf{r}) = \tfrac{1}{2}\sum_{nmn'm'} \{&[S^{11}_{mnm'n'}a_{m'n'} + S^{12}_{mnm'n'}b_{m'n'}]\mathbf{M}_{mn}(k_1 r, \vartheta, \varphi) \\ &+ [S^{21}_{mnm'n'}a_{m'n'} + S^{22}_{mnm'n'}b_{m'n'}]\mathbf{N}_{mn}(k_1 r, \vartheta, \varphi)\} \\ + \tfrac{1}{2}\sum_{nm} &[a_{mn}\mathbf{M}^{(2)}_{mn}(k_1 r, \vartheta, \varphi) + b_{mn}\mathbf{N}^{(2)}_{mn}(k_1 r, \vartheta, \varphi)]. \end{aligned} \tag{5.47}$$

Since $h_n^{(2)}(k_1 r) = [h_n^{(1)}(k_1 r)]^*$, we have by analogy with Eqs. (C.30) and (C.31)

$$\mathbf{M}^{(2)}_{mn}(k_1 r, \vartheta, \varphi) \underset{\substack{k_1 r\to\infty \\ k_1 r \gg n^2}}{=} \frac{\mathrm{i}^{n+1}\mathrm{e}^{-\mathrm{i}k_1 r}}{k_1 r}\gamma_{mn}\mathbf{C}_{mn}(\vartheta, \varphi), \tag{5.48}$$

$$\mathbf{N}^{(2)}_{mn}(k_1 r, \vartheta, \varphi) \underset{\substack{k_1 r\to\infty \\ k_1 r \gg n^2}}{=} \frac{\mathrm{i}^{n}\mathrm{e}^{-\mathrm{i}k_1 r}}{k_1 r}\gamma_{mn}\mathbf{B}_{mn}(\vartheta, \varphi). \tag{5.49}$$

Using Eqs. (5.47)–(5.49) and (C.30), (C.31), we can represent the total field in the far-field zone as a superposition of outgoing and incoming transverse spherical waves:

$$\mathbf{E}(\mathbf{r}) \underset{k_1 r\to\infty}{=} \frac{\mathrm{e}^{\mathrm{i}k_1 r}}{r}\mathbf{E}_1(\vartheta, \varphi) + \frac{\mathrm{e}^{-\mathrm{i}k_1 r}}{r}\mathbf{E}_2(\vartheta, \varphi), \tag{5.50}$$

where

$$\begin{aligned}\mathbf{E}_1(\vartheta, \varphi) = \frac{1}{2k_1}\sum_{nmn'm'} \gamma_{mn}\mathrm{i}^{-n-1}\{&[S^{11}_{mnm'n'}a_{m'n'} + S^{12}_{mnm'n'}b_{m'n'}]\mathbf{C}_{mn}(\vartheta, \varphi) \\ &+ \mathrm{i}[S^{21}_{mnm'n'}a_{m'n'} + S^{22}_{mnm'n'}b_{m'n'}]\mathbf{B}_{mn}(\vartheta, \varphi)\},\end{aligned} \tag{5.51}$$

$$\mathbf{E}_2(\vartheta, \varphi) = \frac{1}{2k_1}\sum_{nm}\gamma_{mn}\mathrm{i}^{n+1}[a_{mn}\mathbf{C}_{mn}(\vartheta, \varphi) - \mathrm{i}b_{mn}\mathbf{B}_{mn}(\vartheta, \varphi)]. \tag{5.52}$$

Since the first relation of Eq. (2.1) and Eqs. (2.21), (2.40), and (2.49) give

$$\mathbf{H}(\mathbf{r}) \underset{k_1 r\to\infty}{=} \sqrt{\frac{\varepsilon_1}{\mu_0}}\left\{\frac{\mathrm{e}^{\mathrm{i}k_1 r}}{r}\hat{\mathbf{r}}\times\mathbf{E}_1(\vartheta, \varphi) - \frac{\mathrm{e}^{-\mathrm{i}k_1 r}}{r}\hat{\mathbf{r}}\times\mathbf{E}_2(\vartheta, \varphi)\right\}, \tag{5.53}$$

the time-averaged Poynting vector is

$$\begin{aligned}\langle\mathbf{S}(\mathbf{r})\rangle &= \tfrac{1}{2}\mathrm{Re}[\mathbf{E}(\mathbf{r})\times\mathbf{H}^*(\mathbf{r})] \\ &\underset{k_1 r\to\infty}{=} \hat{\mathbf{r}}\,\frac{1}{2r^2}\sqrt{\frac{\varepsilon_1}{\mu_0}}\,\{|\mathbf{E}_1(\vartheta, \varphi)|^2 - |\mathbf{E}_2(\vartheta, \varphi)|^2\}\end{aligned} \tag{5.54}$$

(cf. Eq. (1.40)).

If the scattering object is nonabsorbing, the integral of $\langle \mathbf{S}(\mathbf{r}) \rangle \cdot \hat{\mathbf{r}}$ over a spherical surface at infinity must vanish:

$$\int_0^{2\pi} \mathrm{d}\varphi \int_0^{\pi} \mathrm{d}\vartheta \sin\vartheta \{|\mathbf{E}_1(\vartheta, \varphi)|^2 - |\mathbf{E}_2(\vartheta, \varphi)|^2\} = 0. \tag{5.55}$$

Recalling the orthogonality relations for vector spherical harmonics, Eqs. (C.51) and (C.52), we obtain

$$\begin{aligned}\int_0^{2\pi} \mathrm{d}\varphi \int_0^{\pi} \mathrm{d}\vartheta \sin\vartheta |\mathbf{E}_2(\vartheta, \varphi)|^2 &= \frac{1}{4k_1^2} \sum_{nm} \{|a_{mn}|^2 + |b_{mn}|^2\} \\ &= \frac{1}{4k_1^2} [\mathbf{a}^{*\mathrm{T}} \quad \mathbf{b}^{*\mathrm{T}}] \begin{bmatrix} \mathbf{a} \\ \mathbf{b} \end{bmatrix},\end{aligned} \tag{5.56}$$

where $[\mathbf{a}^{\mathrm{T}} \quad \mathbf{b}^{\mathrm{T}}]$ denotes the string of the expansion coefficients of the incident field. Similarly,

$$\begin{aligned}\int_0^{2\pi} \mathrm{d}\varphi \int_0^{\pi} \mathrm{d}\vartheta \sin\vartheta |\mathbf{E}_1(\vartheta, \varphi)|^2 &= \frac{1}{4k_1^2} \sum_{nm} \left\{ \left| \sum_{n'm'} [S^{11}_{mnm'n'} a_{m'n'} + S^{12}_{mnm'n'} b_{m'n'}] \right|^2 \right. \\ &\qquad \left. + \left| \sum_{n'm'} [S^{21}_{mnm'n'} a_{m'n'} + S^{22}_{mnm'n'} b_{m'n'}] \right|^2 \right\} \\ &= \frac{1}{4k_1^2} [\mathbf{a}^{*\mathrm{T}} \quad \mathbf{b}^{*\mathrm{T}}] \boldsymbol{S}^{*\mathrm{T}} \boldsymbol{S} \begin{bmatrix} \mathbf{a} \\ \mathbf{b} \end{bmatrix}.\end{aligned} \tag{5.57}$$

Since Eq. (5.55) must hold for any incident field, we finally derive the unitarity condition for nonabsorbing scatterers (Waterman 1971; Tsang *et al.* 1985),

$$\boldsymbol{S}^{*\mathrm{T}} \boldsymbol{S} = \mathbf{E}. \tag{5.58}$$

In terms of the T matrix, Eq. (5.58) becomes

$$\mathbf{T}^{*\mathrm{T}} \mathbf{T} = -\tfrac{1}{2}(\mathbf{T}^{*\mathrm{T}} + \mathbf{T}) \tag{5.59}$$

or

$$\sum_{j=1}^{2} \sum_{n_1=1}^{\infty} \sum_{m_1=-n_1}^{n_1} (T^{jk}_{m_1 n_1 mn})^* T^{jl}_{m_1 n_1 m'n'} = -\tfrac{1}{2}[(T^{lk}_{m'n'mn})^* + T^{kl}_{mnm'n'}]. \tag{5.60a}$$

Obviously, for absorbing particles (i.e., with a non-zero imaginary part of the relative refractive index) the integral in Eq. (5.55) must be negative, thereby leading to the inequality

$$\sum_{j=1}^{2} \sum_{n_1=1}^{\infty} \sum_{m_1=-n_1}^{n_1} (T^{jk}_{m_1 n_1 mn})^* T^{jl}_{m_1 n_1 m'n'} < -\tfrac{1}{2}[(T^{lk}_{m'n'mn})^* + T^{kl}_{mnm'n'}]. \tag{5.60b}$$

This condition is equivalent to the "contractivity" of the matrix $\boldsymbol{S}$ (cf. Eq. (5.45)), i.e.,

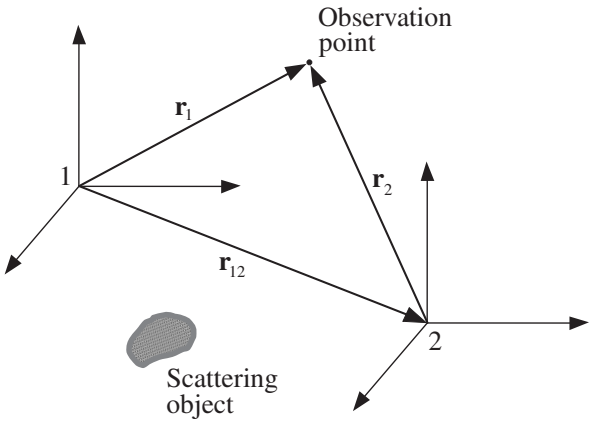

Figure 5.2. The vector $\mathbf{r}_{12}$ translates coordinate system 1 into coordinate system 2.

to the requirement that $\boldsymbol{S}$ map all nontrivial vectors into vectors with a smaller Euclidean norm. This in turn is equivalent to the requirement that $\mathbf{E}-\boldsymbol{S}^{*\mathrm{T}}\boldsymbol{S}$ must have only positive eigenvalues (see also Eq. (5.58)). Equations (5.58)–(5.60) are valid for any particle orientation with respect to the laboratory reference frame. Taking the trace of both sides of Eqs. (5.60a) and (5.60b) over the indices $\{k,l\}$ and $\{n,n'\}$, and making use of Eq. (5.36), we derive a consequence of the unitarity condition for a rotationally symmetric object provided that the *z*-axis of the particle reference frame is directed along the axis of rotation:

$$\sum_{k=1}^{2}\sum_{l=1}^{2}\sum_{n=\max(1,|m|)}^{\infty}\sum_{n'=\max(1,|m|)}^{\infty}|T_{mnmn'}^{kl}(P)|^2$$

$$\le -\mathrm{Re}\sum_{n=\max(1,|m|)}^{\infty}[T_{mnmn}^{11}(P)+T_{mnmn}^{22}(P)],\qquad m=0,\pm1,\ldots, \tag{5.61}$$

where the equality holds only for nonabsorbing scatterers (Wielaard *et al.* 1997).

5.2.4 Translation transformation rule

We saw in subsection 5.2.1 that the rotation transformation rule for vector spherical wave functions leads to a simple rotation transformation rule for the *T* matrix. Similarly, the translation addition theorem for vector spherical wave functions (Appendix C) can be used to derive a translation transformation rule for the *T* matrix (Mishchenko *et al.* 1996b).

Consider the same scattering problem in two coordinate systems that have identical spatial orientations but different origins (Fig. 5.2). Vectors $\mathbf{r}_1$ and $\mathbf{r}_2$ are position vectors of the same observation point in coordinate systems 1 and 2, respectively. The vector $\mathbf{r}_{12}$ connects the origin of coordinate system 1 with the origin of coordinate system 2, so that $\mathbf{r}_1=\mathbf{r}_{12}+\mathbf{r}_2$. The expansions of the incident field and the scattered field in the two coordinate systems are

$$\mathbf{E}^{\rm inc}(\mathbf{r}_1)=\sum_{n=1}^{\infty}\sum_{m=-n}^{n}[a_{mn}^{(1)}{\rm Rg}\mathbf{M}_{mn}(k_1\mathbf{r}_1)+b_{mn}^{(1)}{\rm Rg}\mathbf{N}_{mn}(k_1\mathbf{r}_1)], \tag{5.62}$$

$$\mathbf{E}^{\rm sca}(\mathbf{r}_1)=\sum_{n=1}^{\infty}\sum_{m=-n}^{n}[p_{mn}^{(1)}\mathbf{M}_{mn}(k_1\mathbf{r}_1)+q_{mn}^{(1)}\mathbf{N}_{mn}(k_1\mathbf{r}_1)], \quad r_1>r_>^{(1)}, \tag{5.63}$$

$$\mathbf{E}^{\rm inc}(\mathbf{r}_2)=\sum_{n=1}^{\infty}\sum_{m=-n}^{n}[a_{mn}^{(2)}{\rm Rg}\mathbf{M}_{mn}(k_1\mathbf{r}_2)+b_{mn}^{(2)}{\rm Rg}\mathbf{N}_{mn}(k_1\mathbf{r}_2)], \tag{5.64}$$

$$\mathbf{E}^{\rm sca}(\mathbf{r}_2)=\sum_{n=1}^{\infty}\sum_{m=-n}^{n}[p_{mn}^{(2)}\mathbf{M}_{mn}(k_1\mathbf{r}_2)+q_{mn}^{(2)}\mathbf{N}_{mn}(k_1\mathbf{r}_2)], \quad r_2>r_>^{(2)}, \tag{5.65}$$

where the superscripts (1) and (2) label quantities pertaining to coordinate systems 1 and 2, respectively. In Eqs. (5.63) and (5.65), $r_>^{(1)}$ and $r_>^{(2)}$ are the radii of the respective smallest circumscribing spheres of the scattering object centered at origins 1 and 2. According to the translation addition theorem (cf. Eqs. (C.66) and (C.67) of Appendix C),

$$\begin{aligned}{\rm Rg}\begin{matrix}\mathbf{M}_{mn}\\ \mathbf{N}_{mn}\end{matrix}(k_1\mathbf{r}_2)=\sum_{\nu=1}^{\infty}\sum_{\mu=-\nu}^{\nu}\Bigg[&{\rm Rg}\begin{matrix}A_{\mu\nu mn}\\ B_{\mu\nu mn}\end{matrix}(-k_1\mathbf{r}_{12}){\rm Rg}\mathbf{M}_{\mu\nu}(k_1\mathbf{r}_1)\\ &+{\rm Rg}\begin{matrix}B_{\mu\nu mn}\\ A_{\mu\nu mn}\end{matrix}(-k_1\mathbf{r}_{12}){\rm Rg}\mathbf{N}_{\mu\nu}(k_1\mathbf{r}_1)\Bigg],\end{aligned} \tag{5.66}$$

$$\begin{aligned}\begin{matrix}\mathbf{M}_{mn}\\ \mathbf{N}_{mn}\end{matrix}(k_1\mathbf{r}_1)=\sum_{\nu=1}^{\infty}\sum_{\mu=-\nu}^{\nu}\Bigg[&{\rm Rg}\begin{matrix}A_{\mu\nu mn}\\ B_{\mu\nu mn}\end{matrix}(k_1\mathbf{r}_{12})\mathbf{M}_{\mu\nu}(k_1\mathbf{r}_2)\\ &+{\rm Rg}\begin{matrix}B_{\mu\nu mn}\\ A_{\mu\nu mn}\end{matrix}(k_1\mathbf{r}_{12})\mathbf{N}_{\mu\nu}(k_1\mathbf{r}_2)\Bigg], \quad r_1>r_{12}.\end{aligned} \tag{5.67}$$

The incident field and the scattered field at the observation point are, of course, independent of the choice of coordinate system. Therefore, the right-hand sides of Eqs. (5.62) and (5.64) and Eqs. (5.63) and (5.65) must be equal. Assuming for simplicity that both r_1 and r_2 in Eqs. (5.63) and (5.65) are greater than $\max(r_>^{(1)}, r_>^{(2)}, r_{12})$, we easily derive from the above equations

$$\begin{matrix}a_{\mu\nu}^{(1)}\\ b_{\mu\nu}^{(1)}\end{matrix}=\sum_{n=1}^{\infty}\sum_{m=-n}^{n}\left[{\rm Rg}\begin{matrix}A_{\mu\nu mn}\\ B_{\mu\nu mn}\end{matrix}(-k_1\mathbf{r}_{12})\,a_{mn}^{(2)}+{\rm Rg}\begin{matrix}B_{\mu\nu mn}\\ A_{\mu\nu mn}\end{matrix}(-k_1\mathbf{r}_{12})\,b_{mn}^{(2)}\right], \tag{5.68}$$

$$\begin{matrix}p_{\mu\nu}^{(2)}\\ q_{\mu\nu}^{(2)}\end{matrix}=\sum_{n=1}^{\infty}\sum_{m=-n}^{n}\left[{\rm Rg}\begin{matrix}A_{\mu\nu mn}\\ B_{\mu\nu mn}\end{matrix}(k_1\mathbf{r}_{12})\,p_{mn}^{(1)}+{\rm Rg}\begin{matrix}B_{\mu\nu mn}\\ A_{\mu\nu mn}\end{matrix}(k_1\mathbf{r}_{12})\,q_{mn}^{(1)}\right], \tag{5.69}$$

or

$$\begin{bmatrix}\mathbf{a}^{(1)}\\ \mathbf{b}^{(1)}\end{bmatrix}=\begin{bmatrix}{\rm Rg}\mathbf{A}(-k_1\mathbf{r}_{12}) & {\rm Rg}\mathbf{B}(-k_1\mathbf{r}_{12})\\ {\rm Rg}\mathbf{B}(-k_1\mathbf{r}_{12}) & {\rm Rg}\mathbf{A}(-k_1\mathbf{r}_{12})\end{bmatrix}\begin{bmatrix}\mathbf{a}^{(2)}\\ \mathbf{b}^{(2)}\end{bmatrix}, \tag{5.70}$$

$$\begin{bmatrix} \mathbf{p}^{(2)} \\ \mathbf{q}^{(2)} \end{bmatrix} = \begin{bmatrix} \mathrm{Rg}\mathbf{A}(k_1\mathbf{r}_{12}) & \mathrm{Rg}\mathbf{B}(k_1\mathbf{r}_{12}) \\ \mathrm{Rg}\mathbf{B}(k_1\mathbf{r}_{12}) & \mathrm{Rg}\mathbf{A}(k_1\mathbf{r}_{12}) \end{bmatrix} \begin{bmatrix} \mathbf{p}^{(1)} \\ \mathbf{q}^{(1)} \end{bmatrix}. \tag{5.71}$$

Since

$$\begin{bmatrix} \mathbf{p}^{(1)} \\ \mathbf{q}^{(1)} \end{bmatrix} = \begin{bmatrix} \mathbf{T}^{11}(1) & \mathbf{T}^{12}(1) \\ \mathbf{T}^{21}(1) & \mathbf{T}^{22}(1) \end{bmatrix} \begin{bmatrix} \mathbf{a}^{(1)} \\ \mathbf{b}^{(1)} \end{bmatrix}, \tag{5.72}$$

$$\begin{bmatrix} \mathbf{p}^{(2)} \\ \mathbf{q}^{(2)} \end{bmatrix} = \begin{bmatrix} \mathbf{T}^{11}(2) & \mathbf{T}^{12}(2) \\ \mathbf{T}^{21}(2) & \mathbf{T}^{22}(2) \end{bmatrix} \begin{bmatrix} \mathbf{a}^{(2)} \\ \mathbf{b}^{(2)} \end{bmatrix}, \tag{5.73}$$

we finally have

$$\begin{bmatrix} \mathbf{T}^{11}(2) & \mathbf{T}^{12}(2) \\ \mathbf{T}^{21}(2) & \mathbf{T}^{22}(2) \end{bmatrix} = \begin{bmatrix} \mathrm{Rg}\mathbf{A}(k_1\mathbf{r}_{12}) & \mathrm{Rg}\mathbf{B}(k_1\mathbf{r}_{12}) \\ \mathrm{Rg}\mathbf{B}(k_1\mathbf{r}_{12}) & \mathrm{Rg}\mathbf{A}(k_1\mathbf{r}_{12}) \end{bmatrix} \begin{bmatrix} \mathbf{T}^{11}(1) & \mathbf{T}^{12}(1) \\ \mathbf{T}^{21}(1) & \mathbf{T}^{22}(1) \end{bmatrix} \times \begin{bmatrix} \mathrm{Rg}\mathbf{A}(-k_1\mathbf{r}_{12}) & \mathrm{Rg}\mathbf{B}(-k_1\mathbf{r}_{12}) \\ \mathrm{Rg}\mathbf{B}(-k_1\mathbf{r}_{12}) & \mathrm{Rg}\mathbf{A}(-k_1\mathbf{r}_{12}) \end{bmatrix}. \tag{5.74}$$

Note that unlike the asymptotic far-field translation transformation rule for the amplitude matrix (Eq. (2.191)), Eq. (5.74) is exact and does not involve the assumption of far-field scattering.

5.3 Extinction matrix for axially oriented particles

The rotation transformation rule for the T matrix can be used to develop efficient analytical procedures for averaging scattering characteristics over particle orientations. We begin by calculating the extinction matrix for nonspherical particles axially oriented by an external force (Mishchenko 1991b). As mentioned earlier, typical examples of axially oriented particles are interstellar dust grains oriented by cosmic magnetic fields (Martin 1978; Dolginov *et al*. 1995) and nonspherical hydrometeors in the earth atmosphere oriented by the aerodynamical force (Oguchi 1983; Liou 1992). The orientation distribution of interstellar dust grains is symmetric with respect to the direction of the local magnetic field, whereas the orientation distribution of hydrometeors is symmetric with respect to the vector of the particle velocity relative to the surrounding air mass.

By directing the z-axis of the laboratory reference frame along the axis of symmetry, we arrive at the orientation distribution function given by Eq. (3.28). Equations (2.140)–(2.146) and (5.11)–(5.14) show that in order to find the orientation-averaged extinction matrix, we must first calculate the orientation-averaged T matrix with respect to the laboratory reference frame. Assuming for simplicity that all particles have the same size and shape and taking into account that

$$\int_0^{2\pi} \mathrm{d}\alpha \exp[-\mathrm{i}(m-m')\alpha] = 2\pi\delta_{mm'}, \tag{5.75}$$

we have from Eqs. (3.28), (5.29), and (B.6)

$$\langle T^{kl}_{mnm'n'}(L)\rangle = \int_0^{2\pi} \mathrm{d}\alpha \int_0^{\pi} \mathrm{d}\beta \sin\beta \int_0^{2\pi} \mathrm{d}\gamma p_{\mathrm{o}}(\alpha, \beta, \gamma) T^{kl}_{mnm'n'}(L; \alpha, \beta, \gamma)$$

$$= \delta_{mm'} \sum_{m_1=-\min(n, n')}^{\min(n, n')} T^{kl}_{m_1 n m_1 n'}(P) \int_0^{\pi} \mathrm{d}\beta \sin\beta\, p_{\mathrm{o}}(\beta) d^{n}_{mm_1}(\beta) d^{n'}_{mm_1}(\beta), \qquad (5.76)$$

where $\mathbf{T}(P)$ is the T matrix in the particle reference frame. The Clebsch–Gordan expansion (B.50) and Eqs. (B.5) and (B.27) give

$$d^{n}_{mm_1}(\beta) d^{n'}_{mm_1}(\beta) = (-1)^{m+m_1} \sum_{n_1=|n-n'|}^{n+n'} C^{n_1 0}_{nm\, n'-m} P_n(\cos\beta) C^{n_1 0}_{nm_1\, n'-m_1}, \qquad (5.77)$$

where $C^{nm}_{n_1 m_1\, n_2 m_2}$ are Clebsch–Gordan coefficients (Appendix D). Thus

$$\langle T^{kl}_{mnm'n'}(L)\rangle = \delta_{mm'} T^{kl}_{mnn'}, \qquad k, l = 1, 2, \qquad (5.78)$$

where

$$T^{kl}_{mnn'} = \sum_{m_1=-\min(n, n')}^{\min(n, n')} \sum_{n_1=|n-n'|}^{n+n'} (-1)^{m+m_1} p_{n_1} C^{n_1 0}_{nm\, n'-m} C^{n_1 0}_{nm_1\, n'-m_1} T^{kl}_{m_1 n m_1 n'}(P) \qquad (5.79)$$

and

$$p_n = \int_0^{\pi} \mathrm{d}\beta \sin\beta\, P_n(\cos\beta) p_{\mathrm{o}}(\beta). \qquad (5.80)$$

In other words, the quantities p_n are coefficients in the expansion of the function $p_{\mathrm{o}}(\beta)$ in Legendre polynomials (cf. Eqs. (B.19) and (B.21)):

$$p_{\mathrm{o}}(\beta) = \sum_{n=0}^{\infty} \frac{2n+1}{2} p_n P_n(\cos\beta). \qquad (5.81)$$

Equations (5.78) and (5.79) provide a simple analytical expression of the orientation-averaged T matrix in terms of the T matrix computed in an arbitrarily chosen particle reference frame.

Substituting Eq. (5.78) in Eqs. (5.11)–(5.14) gives

$$\langle S_{11}(\hat{\mathbf{n}}, \hat{\mathbf{n}})\rangle = \frac{1}{k_1} \sum_{n=1}^{\infty} \sum_{n'=1}^{\infty} \sum_{m=-\min(n, n')}^{\min(n, n')} \mathrm{i}^{n'-n-1} \left[\frac{(2n+1)(2n'+1)}{n(n+1)n'(n'+1)}\right]^{1/2} [T^{11}_{mnn'} \pi_{mn}(\vartheta) \pi_{mn'}(\vartheta)$$

$$+ T^{21}_{mnn'} \tau_{mn}(\vartheta) \pi_{mn'}(\vartheta) + T^{12}_{mnn'} \pi_{mn}(\vartheta) \tau_{mn'}(\vartheta) + T^{22}_{mnn'} \tau_{mn}(\vartheta) \tau_{mn'}(\vartheta)], \quad (5.82)$$

$$\langle S_{12}(\hat{\mathbf{n}}, \hat{\mathbf{n}})\rangle = \frac{1}{\mathrm{i}k_1} \sum_{n=1}^{\infty} \sum_{n'=1}^{\infty} \sum_{m=-\min(n, n')}^{\min(n, n')} \mathrm{i}^{n'-n-1} \left[\frac{(2n+1)(2n'+1)}{n(n+1)n'(n'+1)}\right]^{1/2} [T^{11}_{mnn'} \pi_{mn}(\vartheta) \tau_{mn'}(\vartheta)$$

$$+ T^{21}_{mnn'} \tau_{mn}(\vartheta) \tau_{mn'}(\vartheta) + T^{12}_{mnn'} \pi_{mn}(\vartheta) \pi_{mn'}(\vartheta) + T^{22}_{mnn'} \tau_{mn}(\vartheta) \pi_{mn'}(\vartheta)], \quad (5.83)$$

$$\langle S_{21}(\hat{\mathbf{n}},\hat{\mathbf{n}})\rangle = \frac{\mathrm{i}}{k_1}\sum_{n=1}^{\infty}\sum_{n'=1}^{\infty}\sum_{m=-\min(n,n')}^{\min(n,n')} \mathrm{i}^{n'-n-1}\left[\frac{(2n+1)(2n'+1)}{n(n+1)n'(n'+1)}\right]^{1/2} [T_{mnn'}^{11}\tau_{mn}(\vartheta)\pi_{mn'}(\vartheta)$$
$$+ T_{mnn'}^{21}\pi_{mn}(\vartheta)\pi_{mn'}(\vartheta) + T_{mnn'}^{12}\tau_{mn}(\vartheta)\tau_{mn'}(\vartheta) + T_{mnn'}^{22}\pi_{mn}(\vartheta)\tau_{mn'}(\vartheta)], \quad (5.84)$$

$$\langle S_{22}(\hat{\mathbf{n}},\hat{\mathbf{n}})\rangle = \frac{1}{k_1}\sum_{n=1}^{\infty}\sum_{n'=1}^{\infty}\sum_{m=-\min(n,n')}^{\min(n,n')} \mathrm{i}^{n'-n-1}\left[\frac{(2n+1)(2n'+1)}{n(n+1)n'(n'+1)}\right]^{1/2} [T_{mnn'}^{11}\tau_{mn}(\vartheta)\tau_{mn'}(\vartheta)$$
$$+ T_{mnn'}^{21}\pi_{mn}(\vartheta)\tau_{mn'}(\vartheta) + T_{mnn'}^{12}\tau_{mn}(\vartheta)\pi_{mn'}(\vartheta) + T_{mnn'}^{22}\pi_{mn}(\vartheta)\pi_{mn'}(\vartheta)]. \quad (5.85)$$

The orientation-averaged Stokes extinction matrix per particle is obtained by substituting Eqs. (5.82)–(5.85) in Eqs. (2.140)–(2.146). Quite naturally, the axial symmetry of the particle orientation distribution makes the extinction matrix in the laboratory reference frame independent of the azimuthal angle of the incident beam.

The above equations become simpler and computationally more efficient for rotationally symmetric particles. Directing the z-axis of the particle reference frame along the axis of rotation yields symmetry relations (5.36) and (5.37). Taking into account the symmetry relation (D.7), we obtain from Eqs. (5.79), (5.82)–(5.85), (5.16), and (5.17)

$$T_{mnn'}^{kl} = (-1)^m \sum_{n_1=|n-n'|}^{n+n'} [1+(-1)^{n+n'+n_1+k+l}]p_{n_1} C_{nm\,n'-m}^{n_1 0}$$
$$\times \sum_{m_1=0}^{\min(n,n')} (-1)^{m_1}(1-\tfrac{1}{2}\delta_{m_1 0}) C_{nm_1\,n'-m_1}^{n_1 0} T_{m_1 n m_1 n'}^{kl}(P), \quad (5.86)$$

$$T_{-mnn'}^{kl} = (-1)^{k+l} T_{mnn'}^{kl}, \quad (5.87)$$

$$\langle S_{11}(\hat{\mathbf{n}},\hat{\mathbf{n}})\rangle = \frac{1}{k_1}\sum_{n=1}^{\infty}\sum_{n'=1}^{\infty}\sum_{m=0}^{\min(n,n')} (2-\delta_{m0})\mathrm{i}^{n'-n-1}\left[\frac{(2n+1)(2n'+1)}{n(n+1)n'(n'+1)}\right]^{1/2}$$
$$\times [T_{mnn'}^{11}\pi_{mn}(\vartheta)\pi_{mn'}(\vartheta) + T_{mnn'}^{21}\tau_{mn}(\vartheta)\pi_{mn'}(\vartheta)$$
$$+ T_{mnn'}^{12}\pi_{mn}(\vartheta)\tau_{mn'}(\vartheta) + T_{mnn'}^{22}\tau_{mn}(\vartheta)\tau_{mn'}(\vartheta)], \quad (5.88)$$

$$\langle S_{12}(\hat{\mathbf{n}},\hat{\mathbf{n}})\rangle = \langle S_{21}(\hat{\mathbf{n}},\hat{\mathbf{n}})\rangle = 0, \quad (5.89)$$

$$\langle S_{22}(\hat{\mathbf{n}},\hat{\mathbf{n}})\rangle = \frac{1}{k_1}\sum_{n=1}^{\infty}\sum_{n'=1}^{\infty}\sum_{m=0}^{\min(n,n')} (2-\delta_{m0})\mathrm{i}^{n'-n-1}\left[\frac{(2n+1)(2n'+1)}{n(n+1)n'(n'+1)}\right]^{1/2}$$
$$\times [T_{mnn'}^{11}\tau_{mn}(\vartheta)\tau_{mn'}(\vartheta) + T_{mnn'}^{21}\pi_{mn}(\vartheta)\tau_{mn'}(\vartheta)$$
$$+ T_{mnn'}^{12}\tau_{mn}(\vartheta)\pi_{mn'}(\vartheta) + T_{mnn'}^{22}\pi_{mn}(\vartheta)\pi_{mn'}(\vartheta)]. \quad (5.90)$$

Finally, Eqs. (5.88)–(5.90) and (2.140)–(2.146) yield the average extinction matrix per particle:

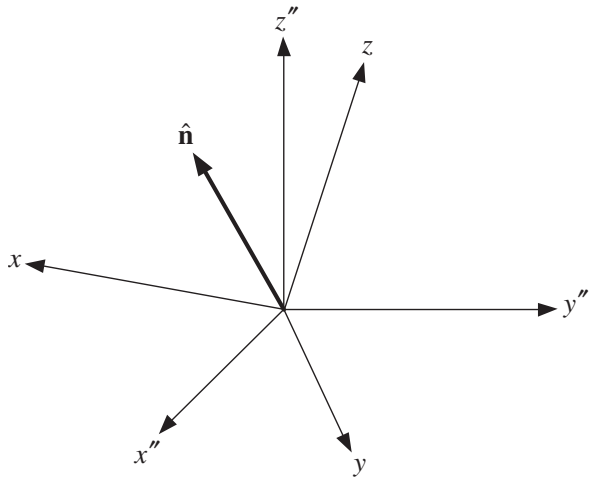

Figure 5.3. The laboratory reference frame $L\{x, y, z\}$ and the device reference frame $D\{x'', y'', z''\}$. The z-axis of the laboratory reference frame is directed along the axis of symmetry of the particle orientation distribution.

$$\langle \mathbf{K}(\vartheta)\rangle = \begin{bmatrix} \langle K_{11}(\vartheta)\rangle & \langle K_{12}(\vartheta)\rangle & 0 & 0 \\ \langle K_{12}(\vartheta)\rangle & \langle K_{11}(\vartheta)\rangle & 0 & 0 \\ 0 & 0 & \langle K_{11}(\vartheta)\rangle & \langle K_{34}(\vartheta)\rangle \\ 0 & 0 & -\langle K_{34}(\vartheta)\rangle & \langle K_{11}(\vartheta)\rangle \end{bmatrix}, \tag{5.91}$$

where

$$\langle K_{11}(\vartheta)\rangle = \frac{2\pi}{k_1}\,\mathrm{Im}[\langle S_{11}(\hat{\mathbf{n}}, \hat{\mathbf{n}})\rangle + \langle S_{22}(\hat{\mathbf{n}}, \hat{\mathbf{n}})\rangle], \tag{5.92}$$

$$\langle K_{12}(\vartheta)\rangle = \frac{2\pi}{k_1}\,\mathrm{Im}[\langle S_{11}(\hat{\mathbf{n}}, \hat{\mathbf{n}})\rangle - \langle S_{22}(\hat{\mathbf{n}}, \hat{\mathbf{n}})\rangle], \tag{5.93}$$

$$\langle K_{34}(\vartheta)\rangle = \frac{2\pi}{k_1}\,\mathrm{Re}[\langle S_{22}(\hat{\mathbf{n}}, \hat{\mathbf{n}})\rangle - \langle S_{11}(\hat{\mathbf{n}}, \hat{\mathbf{n}})\rangle]. \tag{5.94}$$

The reference frame associated with the measuring device (e.g., a telescope or an antenna) does not necessarily coincide with the laboratory reference frame having its z-axis directed along the axis of symmetry of the particle orientation distribution. Let $L\{x, y, z\}$ be the laboratory reference frame and $D\{x'', y'', z''\}$ the reference frame associated with the measuring device (see Fig. 5.3). Let η be the non-negative angle of rotation around $\hat{\mathbf{n}}$ that transforms the $\hat{\mathbf{n}}z$-plane into the $\hat{\mathbf{n}}z''$-plane. This angle is measured in the *clockwise* direction, when looking in the direction of $\hat{\mathbf{n}}$. Obviously, η is the angle between the meridional planes of the beam in the laboratory and device reference frames, respectively, and hence the angle between the unit vectors $\hat{\boldsymbol{\vartheta}}$ and $\hat{\boldsymbol{\vartheta}}''$ and the unit vectors $\hat{\boldsymbol{\varphi}}$ and $\hat{\boldsymbol{\varphi}}''$. We thus have for the average extinction matrix in the device reference frame:

$$\langle \mathbf{K}_{\mathrm{D}}(\hat{\mathbf{n}})\rangle = \mathbf{L}(\eta)\langle \mathbf{K}(\vartheta)\rangle \mathbf{L}(-\eta), \tag{5.95}$$

where the rotation matrix $\mathbf{L}$ is defined by Eq. (1.97).

The actual computer calculation of the orientationally averaged extinction matrix involves the following steps.

1. computation of the *T* matrix in the particle reference frame;
2. computation of the expansion coefficients p_n for a given orientation distribution function $p_o(\beta)$;
3. computation of the Clebsch–Gordan coefficients in Eq. (5.79) or Eq. (5.86);
4. computation of the orientation-averaged *T* matrix with respect to the laboratory reference frame via Eq. (5.79) for arbitrarily shaped particles or via Eq. (5.86) for rotationally symmetric particles;
5. computation of the angular functions $\pi_{mn}(\vartheta)$ and $\tau_{mn}(\vartheta)$;
6. computation of the orientation-averaged forward-scattering amplitude matrix via Eqs. (5.82)–(5.85) for arbitrarily shaped particles or via Eqs. (5.88)–(5.90) for rotationally symmetric particles;
7. computation of the orientation-averaged extinction matrix in the laboratory reference frame via Eq. (2.140)–(2.146) for arbitrarily shaped particles or via Eqs. (5.91)–(5.94) for rotationally symmetric particles;
8. computation of the orientation-averaged extinction matrix in the device reference frame via Eq. (5.95).

The computation of the *T* matrix for different types of particles will be discussed later in this chapter. Convenient and numerically stable and efficient recurrence formulas for computing the angular functions and the Clebsch–Gordan coefficients are given in Appendices B and D, respectively.

The analytical approach to computing orientation-averaged optical characteristics is a unique feature of the *T*-matrix method. It requires the *T* matrix to be computed only once, with respect to the particle reference frame, and then yields the average characteristics of a particle ensemble with respect to the laboratory reference frame by virtue of simple analytical formulas. It is not surprising, therefore, that the analytical method works much faster than the standard approach based on the numerical averaging of results computed for many discrete orientations of a nonspherical particle. Extensive timing tests have shown that the analytical averaging procedure (steps 2 through 8) is indeed very efficient and requires only a small fraction of the computer time spent on calculating the *T* matrix in the particle reference frame (step 1). This means that the *T*-matrix calculations of the extinction matrix for an axially symmetric distribution of particle orientations are nearly as fast as those for a single particle in a fixed orientation.

The analytical method for computing the orientation-averaged extinction matrix has been applied to interstellar dust grains (Mishchenko 1991b), nonspherical hydrometeors (Mishchenko 1992a), and bacterial cells and clusters of dielectric particles axially oriented by an external electrostatic field (Fucile *et al.* 1995; Khlebtsov *et al.* 1999).

5.4 Extinction cross section for randomly oriented particles

The orientation distribution function for randomly oriented particles is given by $p_o(\beta) \equiv 1/2$ (cf. Eqs. (3.27) and (3.28)). Equations (5.76) and (B.17) then yield (Mishchenko 1990b)

$$\langle T^{kl}_{mnm'n'}(L)\rangle = \frac{\delta_{nn'}\delta_{mm'}}{2n+1}\sum_{m_1=-n}^{n} T^{kl}_{m_1nm_1n}(P), \qquad k, l = 1, 2. \tag{5.96}$$

Note that the averaged $T^{kl}(L)$ matrices are diagonal and that their elements are independent of the azimuthal indices m and m'.

Assume for simplicity that the scattering particles have a plane of symmetry. Then the extinction matrix for particles in random orientation is given by Eq. (4.32) with

$$\langle C_{\rm ext}\rangle = \frac{2\pi}{k_1}\,{\rm Im}[\langle S_{11}(\hat{\mathbf{n}}, \hat{\mathbf{n}})\rangle + \langle S_{22}(\hat{\mathbf{n}}, \hat{\mathbf{n}})\rangle]. \tag{5.97}$$

Using Eqs. (B.5), (B.6), and (B.25), it is straightforward to show that

$$\pi_{mn}(\vartheta) = \tfrac{1}{2}\sqrt{n(n+1)}[d^n_{1m}(\vartheta) + d^n_{-1m}(\vartheta)], \tag{5.98}$$

$$\tau_{mn}(\vartheta) = \tfrac{1}{2}\sqrt{n(n+1)}[d^n_{1m}(\vartheta) - d^n_{-1m}(\vartheta)]. \tag{5.99}$$

Therefore, the unitarity condition (B.47) yields

$$\sum_{m=-n}^{n}[\pi_{mn}(\vartheta)]^2 = \sum_{m=-n}^{n}[\tau_{mn}(\vartheta)]^2 = \tfrac{1}{2}n(n+1), \tag{5.100}$$

$$\sum_{m=-n}^{n}\pi_{mn}(\vartheta)\tau_{mn}(\vartheta) = 0. \tag{5.101}$$

Inserting Eqs. (5.96), (5.100), and (5.101) in Eqs. (5.11) and (5.14), we finally derive

$$\langle C_{\rm ext}\rangle = -\frac{2\pi}{k_1^2}\,{\rm Re}\sum_{n=1}^{\infty}\sum_{m=-n}^{n}[T^{11}_{mnmn}(P) + T^{22}_{mnmn}(P)] \tag{5.102}$$

(Mishchenko 1990b). This remarkably simple formula shows that the extinction cross section per particle averaged over the uniform orientation distribution is proportional to the real part of the sum of the diagonal elements of the T matrix computed in the particle reference frame.

The extinction cross section for randomly oriented particles must be invariant with respect to rotations of the coordinate system. Since the choice of the particle and laboratory reference frames is, in principle, arbitrary, we must have

$$\mathrm{Re}\sum_{n=1}^{\infty}\sum_{m=-n}^{n}[T^{11}_{mnmn}(L;\alpha,\beta,\gamma)+T^{22}_{mnmn}(L;\alpha,\beta,\gamma)]$$
$$=\mathrm{Re}\sum_{n=1}^{\infty}\sum_{m=-n}^{n}[T^{11}_{mnmn}(P)+T^{22}_{mnmn}(P)] \tag{5.103}$$

for any (α, β, γ). Indeed, Eqs. (5.29) and (B.41) yield the invariant

$$\sum_{m=-n}^{n}T^{kl}_{mnmn}(L;\alpha,\beta,\gamma)=\sum_{m=-n}^{n}T^{kl}_{mnmn}(P), \tag{5.104}$$

which leads to Eq. (5.103). The invariance of the extinction cross section with respect to translations of the coordinate system (Section 2.11) and Eq. (5.102) yield another invariant of the *T* matrix (see subsection 5.2.4):

$$\mathrm{Re}\sum_{nmk}T^{kk}_{mnmn}(2)=\mathrm{Re}\sum_{nmk}T^{kk}_{mnmn}(1). \tag{5.105}$$

If the scattering particles are rotationally symmetric and the *z*-axis of the particle reference frame is directed along the axis of rotation, then Eq. (5.37) applies, and we have

$$\langle T^{kl}_{mnm'n'}(L)\rangle=\frac{\delta_{nn'}\delta_{mm'}\delta_{kl}}{2n+1}\sum_{m_1=0}^{n}(2-\delta_{m_1 0})T^{kl}_{m_1 n m_1 n}(P), \qquad k,l=1,2, \tag{5.106}$$

$$\langle C_{\mathrm{ext}}\rangle=-\frac{2\pi}{k_1^2}\mathrm{Re}\sum_{n=1}^{\infty}\sum_{m=0}^{n}(2-\delta_{m0})[T^{11}_{mnmn}(P)+T^{22}_{mnmn}(P)]. \tag{5.107}$$

5.5 Scattering matrix for randomly oriented particles

Consider now the computation of the scattering matrix for randomly oriented particles. Following Section 4.2, we will assume that the incident wave propagates along the positive direction of the *z*-axis of the laboratory reference frame and that the *xz*-plane with $x \geq 0$ is the scattering plane. We will also assume that all particles are identical and have a plane of symmetry. Our ultimate task is to find the orientation-averaged scattering cross section per particle $\langle C_{\mathrm{sca}}\rangle$ and the elements of the normalized Stokes scattering matrix $\widetilde{\mathbf{F}}(\Theta)$. We will defer the computation of $\langle C_{\mathrm{sca}}\rangle$ to the following section and will focus now on computing the normalized scattering matrix given by Eq. (4.51), in which

$$\langle\mathbf{F}(\Theta)\rangle=\frac{1}{8\pi^2}\int_0^{2\pi}\mathrm{d}\alpha\int_0^{\pi}\mathrm{d}\beta\sin\beta\int_0^{2\pi}\mathrm{d}\gamma\,\mathbf{Z}(\vartheta^{\mathrm{sca}}=\Theta,\varphi^{\mathrm{sca}}=0;\vartheta^{\mathrm{inc}}=0,\varphi^{\mathrm{inc}}=0;\alpha,\beta,\gamma); \tag{5.108}$$

here the Euler angles of rotation α, β, and γ specify the particle orientation with respect to the laboratory reference frame (cf. Eq. (3.27)). The most straightforward

way to compute $\langle \mathbf{F}(\Theta) \rangle$ is to evaluate the integrals in Eq. (5.108) numerically by applying appropriate quadrature formulas and recomputing $\mathbf{Z}(\Theta, 0; 0, 0; \alpha, \beta, \gamma)$ for each new scattering angle and each new combination of the Euler angles (α, β, γ) (Wiscombe and Mugnai 1986; Barber and Hill 1990). However, we will demonstrate in Chapter 10 that $\mathbf{Z}(\Theta, 0; 0, 0; \alpha, \beta, \gamma)$ is a strongly oscillating function of (α, β, γ), thereby necessitating large numbers of quadrature division points in the numerical integrations. This makes the numerical averaging procedure very time-consuming, especially when results for many scattering angles are required.

We have seen in Section 4.11 that convenient representations of the elements of the normalized scattering matrix are expansions in the generalized spherical functions (4.75)–(4.80). The expansion coefficients appearing in these series are independent of the scattering angle and the polarization state of the incident and scattered beams and are functions of only the particle morphology, the size relative to the wavelength, and the relative refractive index (see subsection 5.8.2). Similarly, the particle T matrix is also a quantity independent of the incident and scattered waves and is fully determined by the particle geometry and composition. Therefore, one may expect a direct analytical relationship between the expansion coefficients and the T matrix that does not involve any angular or polarization variable. Mishchenko (1991a) showed that this relationship does exist and facilitates the development of an efficient analytical orientation-averaging procedure that avoids the time-consuming numerical integrations in Eq. (5.108).

Since many formulas become noticeably simpler in the circular-polarization representation, we begin by considering the normalized circular-polarization phase matrix defined by Eq. (4.98). By analogy with Eq. (5.108), the orientation-averaged circular-polarization phase matrix per particle $\langle \mathbf{Z}^{\rm CP}(\Theta, 0; 0, 0) \rangle$ is given by

$$\langle \mathbf{Z}^{\rm CP}(\Theta, 0; 0, 0) \rangle = \frac{1}{8\pi^2} \int_0^{2\pi} \mathrm{d}\alpha \int_0^{\pi} \mathrm{d}\beta \sin\beta \int_0^{2\pi} \mathrm{d}\gamma \, \mathbf{Z}^{\rm CP}(\Theta, 0; 0, 0; \alpha, \beta, \gamma) \tag{5.109}$$

and can be calculated using Eq. (4.97). It follows from Eqs. (5.98), (5.99), and (B.6) that

$$\pi_{mn}(0) = \delta_{m,\pm 1} \tfrac{1}{2} \sqrt{n(n+1)}, \tag{5.110}$$

$$\tau_{mn}(0) = m \delta_{m,\pm 1} \tfrac{1}{2} \sqrt{n(n+1)}. \tag{5.111}$$

Therefore, Eqs. (4.95), (5.11)–(5.14), (5.98), and (5.99) yield

$$C_{++}(\Theta, 0; 0, 0; \alpha, \beta, \gamma) = \sum_{n=1}^{\infty} \sum_{n'=1}^{\infty} \sum_{m=-n}^{n} t_{mnn'} d^n_{-1m}(\Theta) [T^{11}_{mn,-1n'}(L; \alpha, \beta, \gamma)$$
$$- T^{12}_{mn,-1n'}(L; \alpha, \beta, \gamma) - T^{21}_{mn,-1n'}(L; \alpha, \beta, \gamma) + T^{22}_{mn,-1n'}(L; \alpha, \beta, \gamma)], \tag{5.112}$$

$$C_{+-}(\Theta, 0; 0, 0; \alpha, \beta, \gamma) = \sum_{n=1}^{\infty} \sum_{n'=1}^{\infty} \sum_{m=-n}^{n} t_{mnn'} d^n_{-1m}(\Theta) [T^{11}_{mn1n'}(L; \alpha, \beta, \gamma)$$
$$+ T^{12}_{mn1n'}(L; \alpha, \beta, \gamma) - T^{21}_{mn1n'}(L; \alpha, \beta, \gamma) - T^{22}_{mn1n'}(L; \alpha, \beta, \gamma)], \tag{5.113}$$

$$C_{-+}(\Theta, 0; 0, 0; \alpha, \beta, \gamma) = \sum_{n=1}^{\infty}\sum_{n'=1}^{\infty}\sum_{m=-n}^{n} t_{mnn'} d_{1m}^{n}(\Theta)[T_{mn,-1n'}^{11}(L; \alpha, \beta, \gamma)$$
$$- T_{mn,-1n'}^{12}(L; \alpha, \beta, \gamma) + T_{mn,-1n'}^{21}(L; \alpha, \beta, \gamma) - T_{mn,-1n'}^{22}(L; \alpha, \beta, \gamma)], \quad (5.114)$$

$$C_{--}(\Theta, 0; 0, 0; \alpha, \beta, \gamma) = \sum_{n=1}^{\infty}\sum_{n'=1}^{\infty}\sum_{m=-n}^{n} t_{mnn'} d_{1m}^{n}(\Theta)[T_{mn1n'}^{11}(L; \alpha, \beta, \gamma)$$
$$+ T_{mn1n'}^{12}(L; \alpha, \beta, \gamma) + T_{mn1n'}^{21}(L; \alpha, \beta, \gamma) + T_{mn1n'}^{22}(L; \alpha, \beta, \gamma)], \quad (5.115)$$

where

$$t_{mnn'} = \frac{1}{2k_1} \mathrm{i}^{n'-n-1}(-1)^{m+1}\sqrt{(2n+1)(2n'+1)}. \quad (5.116)$$

From this point on, we will assume for simplicity that the scattering particles are rotationally symmetric, so that Eqs. (5.36) and (5.37) apply. We then use Eq. (5.29), (B.5), (B.50), (D.6), and (D.7) to derive

$$C_{++}(\Theta, 0; 0, 0; \alpha, \beta, \gamma) = \sum_{n=1}^{\infty}\sum_{m=-n}^{n}\sum_{n_1=|m-1|}^{\infty} f_{nn_1} d_{-1,-m}^{n}(\Theta) d_{1-m,0}^{n_1}(\beta) \exp[-\mathrm{i}\alpha(1-m)] B_{mnn_1}^{1}, \quad (5.117)$$

$$C_{+-}(\Theta, 0; 0, 0; \alpha, \beta, \gamma) = \sum_{n=1}^{\infty}\sum_{m=-n}^{n}\sum_{n_1=|m-1|}^{\infty} f_{nn_1} d_{-1m}^{n}(\Theta) d_{m-1,0}^{n_1}(\beta) \exp[-\mathrm{i}\alpha(m-1)] B_{mnn_1}^{2}, \quad (5.118)$$

$$C_{-+}(\Theta, 0; 0, 0; \alpha, \beta, \gamma) = \sum_{n=1}^{\infty}\sum_{m=-n}^{n}\sum_{n_1=|m-1|}^{\infty} f_{nn_1} d_{1,-m}^{n}(\Theta) d_{1-m,0}^{n_1}(\beta) \exp[-\mathrm{i}\alpha(1-m)] B_{mnn_1}^{2}, \quad (5.119)$$

$$C_{--}(\Theta, 0; 0, 0; \alpha, \beta, \gamma) = \sum_{n=1}^{\infty}\sum_{m=-n}^{n}\sum_{n_1=|m-1|}^{\infty} f_{nn_1} d_{1m}^{n}(\Theta) d_{m-1,0}^{n_1}(\beta) \exp[-\mathrm{i}\alpha(m-1)] B_{mnn_1}^{1}, \quad (5.120)$$

where

$$f_{nn_1} = \frac{1}{2\mathrm{i}k_1}(2n_1+1)\sqrt{2n+1}, \quad (5.121)$$

$$B_{mnn_1}^{j} = \sum_{n'=\max(1,|n-n_1|)}^{n+n_1} C_{nm\,n_1,1-m}^{n'1} A_{nn'n_1}^{j}, \qquad j = 1, 2, \quad (5.122)$$

$$A_{nn'n_1}^{j} = \frac{\mathrm{i}^{n'-n}}{\sqrt{2n'+1}} \sum_{m_1=-\min(n,n')}^{\min(n,n')} C_{nm_1\,n_1 0}^{n'm_1} T_{m_1nn'}^{j}, \qquad j = 1, 2, \quad (5.123)$$

$$T_{mnn'}^{1} = T_{mnmn'}^{11}(P) + T_{mnmn'}^{12}(P) + T_{mnmn'}^{21}(P) + T_{mnmn'}^{22}(P), \quad (5.124)$$

$$T_{mnn'}^{2} = T_{mnmn'}^{11}(P) + T_{mnmn'}^{12}(P) - T_{mnmn'}^{21}(P) - T_{mnmn'}^{22}(P). \quad (5.125)$$

Here, the $T_{mnmn'}^{kl}(P)$ are elements of the T matrix computed in the particle reference frame with the z-axis directed along the axis of particle symmetry and the

$C^{nm}_{n_1m_1\,n_2m_2}$ are the Clebsch–Gordan coefficients (Appendix D). Finally, using Eqs. (4.97), (5.108), (4.98), (4.104), (B.17), and (B.30), we derive the following formulas that can be used in practical computer calculations:

$$g^s_{00} = \sum_{n=1}^{\infty} \sum_{i=\max(1,\,|n-s|)}^{n+s} h_{sni}\, C^{i1}_{n1\,s0} \sum_{m=-\min(n,\,i)}^{\min(n,\,i)} C^{im}_{nm\,s0}\, D^{00}_{mni}, \tag{5.126}$$

$$g^s_{0,-0} = \sum_{n=1}^{\infty} \sum_{i=\max(1,\,|n-s|)}^{n+s} h_{sni}(-1)^{n+i+s}\, C^{i1}_{n1\,s0} \sum_{m=-\min(n,\,i)}^{\min(n,\,i)} C^{im}_{nm\,s0}\, D^{0,-0}_{mni}, \tag{5.127}$$

$$g^s_{22} = \sum_{n=1}^{\infty} \sum_{i=\max(1,\,|n-s|)}^{n+s} h_{sni}\, C^{i1}_{n,-1\,s2} \sum_{m=m_{\min}}^{m_{\max}} C^{i,2-m}_{n,-m\,s2}\, D^{22}_{mni}, \tag{5.128}$$

$$g^s_{2,-2} = \sum_{n=1}^{\infty} \sum_{i=\max(1,\,|n-s|)}^{n+s} h_{sni}(-1)^{n+i+s}\, C^{i1}_{n,-1\,s2} \sum_{m=m_{\min}}^{m_{\max}} C^{i,2-m}_{n,-m\,s2}\, D^{2,-2}_{mni}, \tag{5.129}$$

$$g^s_{02} = -\sum_{n=1}^{\infty} \sum_{i=\max(1,\,|n-s|)}^{n+s} h_{sni}\, C^{i1}_{n1\,s0} \sum_{m=m_{\min}}^{m_{\max}} C^{i,2-m}_{n,-m\,s2}\, D^{02}_{mni}, \tag{5.130}$$

where

$$h_{sni} = \frac{(2s+1)\pi}{k_1^2 \langle C_{\rm sca}\rangle} \sqrt{\frac{2n+1}{2i+1}}, \tag{5.131}$$

$$D^{00}_{mni} = \sum_{n_1=|m-1|}^{\infty} (2n_1+1)\, B^1_{mnn_1} (B^1_{min_1})^*, \tag{5.132}$$

$$D^{0,-0}_{mni} = \sum_{n_1=|m-1|}^{\infty} (2n_1+1)\, B^2_{mnn_1} (B^2_{min_1})^*, \tag{5.133}$$

$$D^{22}_{mni} = \sum_{n_1=|m-1|}^{\infty} (2n_1+1)\, B^1_{mnn_1} (B^1_{2-m,in_1})^*, \tag{5.134}$$

$$D^{2,-2}_{mni} = \sum_{n_1=|m-1|}^{\infty} (2n_1+1)\, B^2_{mnn_1} (B^2_{2-m,in_1})^*, \tag{5.135}$$

$$D^{02}_{mni} = \sum_{n_1=|m-1|}^{\infty} (2n_1+1)\, B^2_{mnn_1} (B^1_{2-m,in_1})^*, \tag{5.136}$$

$$m_{\min} = \max(-n, -i+2), \qquad m_{\max} = \min(n, i+2), \tag{5.137}$$

and $\langle C_{\rm sca}\rangle$ is the orientation-averaged scattering cross section per particle.

Thus the computation of the expansion coefficients appearing in Eqs. (4.75)–(4.80) and the normalized Stokes scattering matrix involves the following steps:

1. computation of the T matrix of an axially symmetric scatterer in the particle reference frame, i.e., the matrix $\mathbf{T}(P)$;
2. computation of the orientation-averaged scattering cross section per particle

$\langle C_{\rm sca} \rangle$ (Section 5.6);

3. computation of the quantities $T^j_{mnn'}$ via Eqs. (5.124) and (5.125);
4. computation of the quantities $A^j_{nn'n_1}$ via Eq. (5.123);
5. computation of the quantities $B^j_{mnn_1}$ via Eq. (5.122);
6. computation of the quantities D^{pq}_{mni} via Eqs. (5.132)–(5.136);
7. computation of the circular-polarization expansion coefficients g^s_{pq} via Eqs. (5.126)–(5.130);
8. computation of the Stokes-representation expansion coefficients via Eqs. (4.109)–(4.114);
9. computation of the elements of the normalized Stokes scattering matrix via Eqs. (4.75)–(4.80).

The most time-consuming part of any computations based on the *T*-matrix method is the evaluation of multiply nested summations. An important advantage of the analytical averaging procedure is that the maximal order of nested summations is only three, thereby making this procedure ideally suited to the development of an efficient computer code. Detailed timing tests have shown that the analytical averaging over orientations (steps 2–9) requires only a small fraction of the computer time needed to compute the $\mathbf{T}(P)$ matrix (Mishchenko 1991a, 1993; Mackowski and Mishchenko 1996; Wielaard *et al.* 1997). It comes as no surprise, therefore, that direct comparisons of the performance of the analytical and numerical methods indicate that the former is faster by a factor of several tens (Mishchenko 1991a; W. M. F. Wauben, personal communication). An equally rewarding feature of the analytical averaging procedure is the demonstration of the close connection between the *T*-matrix method and the concept of expanding the elements of the normalized scattering matrix in generalized spherical functions (or Wigner *d*-functions).

The analytical averaging method has been applied to a wide class of rotationally symmetric scatterers, such as spheroids, finite circular cylinders, osculating spheres, so-called Chebyshev particles, and linear chains of spheres (Sections 5.11 and 5.13). Mackowski and Mishchenko (1996) extended the method to asymmetric particles.

Khlebtsov (1992) and Fucile *et al.* (1993) developed theoretical formalisms that exploit the rotation transformation property of the *T* matrix, but are not based on expanding the normalized scattering matrix in generalized spherical functions and do not exploit the advantage of performing as much work analytically as possible. Borghese *et al.* (2001) considered several simple analytical orientation distribution functions other than the uniform orientation distribution. Paramonov (1995) straightforwardly extended the analytical orientation-averaging approach to arbitrary quadratically integrable orientation distribution functions. However, the resulting formulas involve highly nested summations, and their efficient numerical implementation may often be problematic. In such cases the standard averaging approach employing numerical integrations over Euler orientation angles in Eq. (3.19) and based on formulas of Section 2.4 may prove to be more efficient (cf. Battaglia *et al.* 2001).

5.6 Scattering cross section for randomly oriented particles

The scattering cross section per particle for randomly oriented particles with a plane of symmetry is given by Eq. (4.40), in which $\langle \mathbf{F}(\Theta) \rangle$ is given by Eq. (5.108). Rewriting Eq. (2.123) as

$$\mathbf{Z}(\hat{\mathbf{n}}^{\rm sca}, \hat{\mathbf{n}}^{\rm inc}) = \mathbf{A}^{-1}\mathbf{Z}^{\rm CP}(\hat{\mathbf{n}}^{\rm sca}, \hat{\mathbf{n}}^{\rm inc})\mathbf{A}, \tag{5.138}$$

we have

$$\begin{aligned} Z_{11}(\Theta, 0; 0, 0; \alpha, \beta, \gamma) = \tfrac{1}{2}[&Z_{00}^{\rm CP}(\Theta, 0; 0, 0; \alpha, \beta, \gamma) + Z_{0,-0}^{\rm CP}(\Theta, 0; 0, 0; \alpha, \beta, \gamma) \\ &+ Z_{-00}^{\rm CP}(\Theta, 0; 0, 0; \alpha, \beta, \gamma) + Z_{-0,-0}^{\rm CP}(\Theta, 0; 0, 0; \alpha, \beta, \gamma)]. \end{aligned} \tag{5.139}$$

Recall that Eqs. (5.112)–(5.115) are valid for arbitrary particles. Therefore, using Eqs. (4.97), (5.29), (B.17), and (B.47) and taking into account Eq. (5.75), we derive

$$\langle C_{\rm sca} \rangle = \frac{2\pi}{k_1^2} \sum_{n=1}^{\infty} \sum_{m=-n}^{n} \sum_{n'=1}^{\infty} \sum_{m'=-n'}^{n'} \sum_{k=1}^{2} \sum_{l=1}^{2} |T_{mnm'n'}^{kl}(P)|^2 \tag{5.140}$$

(Mishchenko 1991c). Thus the scattering cross section per particle averaged over the uniform orientation distribution is proportional to the sum of the squares of the absolute values of the T-matrix elements computed in the particle reference frame. This formula is as simple as Eq. (5.102) for the orientation-averaged extinction cross section. If the scattering particles are rotationally symmetric and the z-axis of the particle reference frame coincides with the axis of rotation, then Eqs. (5.36), (5.37), and (5.140) yield

$$\langle C_{\rm sca} \rangle = \frac{2\pi}{k_1^2} \sum_{n=1}^{\infty} \sum_{n'=1}^{\infty} \sum_{m=0}^{\min(n, n')} \sum_{k=1}^{2} \sum_{l=1}^{2} (2 - \delta_{m0}) \, |T_{mnmn'}^{kl}(P)|^2. \tag{5.141}$$

After the average extinction and scattering cross sections per particle have been calculated, the average absorption cross section and the single-scattering albedo can be found from Eqs. (4.44) and (4.45).

Like the extinction cross section, the scattering cross section for randomly oriented particles must be invariant with respect to rotations of the coordinate system. Since the choice of the particle and laboratory reference frames is arbitrary, Eq. (5.140) implies that

$$\sum_{mm'} |T_{mnm'n'}^{kl}(L; \alpha, \beta, \gamma)|^2 = \sum_{mm'} |T_{mnm'n'}^{kl}(P)|^2 \tag{5.142}$$

for any (α, β, γ). This invariant indeed follows from Eqs. (5.29) and (B.41). The invariance of the scattering cross section with respect to translations of the coordinate system (Section 2.11) and Eq. (5.140) yield yet another invariant of the T matrix (cf. subsection 5.2.4):

$$\sum_{nmn'm'kl} |T^{kl}_{mnm'n'}(2)|^2 = \sum_{nmn'm'kl} |T^{kl}_{mnm'n'}(1)|^2. \tag{5.143}$$

The energy conservation law implies that $\langle C_{\rm sca}\rangle \le \langle C_{\rm ext}\rangle$, and we have from Eqs. (5.102) and (5.140)

$$\sum_{n=1}^{\infty}\sum_{m=-n}^{n}\sum_{n'=1}^{\infty}\sum_{m'=-n'}^{n'}\sum_{k=1}^{2}\sum_{l=1}^{2} |T^{kl}_{mnm'n'}(P)|^2 \le -\mathrm{Re}\sum_{n=1}^{\infty}\sum_{m=-n}^{n}[T^{11}_{mnmn}(P)+T^{22}_{mnmn}(P)], \tag{5.144}$$

where the equality holds only for nonabsorbing particles. This formula can also be derived by taking the trace of both sides of Eqs. (5.60a) and (5.60b) over the indices $\{n, n'\}$, $\{m, m'\}$, and $\{k, l\}$.

5.7 Spherically symmetric scatterers (Lorenz–Mie theory)

All *T*-matrix equations become considerably simpler and reduce to the corresponding equations of the Lorenz–Mie theory when the scattering particle is spherically symmetric and Eqs. (5.42)–(5.44) apply. Specifically, Eqs. (5.11)–(5.14) become

$$S_{11}(\hat{\mathbf{n}}^{\rm sca}, \hat{\mathbf{n}}^{\rm inc}) = \frac{\mathrm{i}}{k_1}\sum_{n=1}^{\infty}\sum_{m=-n}^{n}\frac{2n+1}{n(n+1)}\exp[\mathrm{i}m(\varphi^{\rm sca}-\varphi^{\rm inc})]$$
$$\times[b_n\pi_{mn}(\vartheta^{\rm sca})\pi_{mn}(\vartheta^{\rm inc})+a_n\tau_{mn}(\vartheta^{\rm sca})\tau_{mn}(\vartheta^{\rm inc})], \tag{5.145}$$

$$S_{12}(\hat{\mathbf{n}}^{\rm sca}, \hat{\mathbf{n}}^{\rm inc}) = \frac{1}{k_1}\sum_{n=1}^{\infty}\sum_{m=-n}^{n}\frac{2n+1}{n(n+1)}\exp[\mathrm{i}m(\varphi^{\rm sca}-\varphi^{\rm inc})]$$
$$\times[b_n\pi_{mn}(\vartheta^{\rm sca})\tau_{mn}(\vartheta^{\rm inc})+a_n\tau_{mn}(\vartheta^{\rm sca})\pi_{mn}(\vartheta^{\rm inc})], \tag{5.146}$$

$$S_{21}(\hat{\mathbf{n}}^{\rm sca}, \hat{\mathbf{n}}^{\rm inc}) = -\frac{1}{k_1}\sum_{n=1}^{\infty}\sum_{m=-n}^{n}\frac{2n+1}{n(n+1)}\exp[\mathrm{i}m(\varphi^{\rm sca}-\varphi^{\rm inc})]$$
$$\times[b_n\tau_{mn}(\vartheta^{\rm sca})\pi_{mn}(\vartheta^{\rm inc})+a_n\pi_{mn}(\vartheta^{\rm sca})\tau_{mn}(\vartheta^{\rm inc})], \tag{5.147}$$

$$S_{22}(\hat{\mathbf{n}}^{\rm sca}, \hat{\mathbf{n}}^{\rm inc}) = \frac{\mathrm{i}}{k_1}\sum_{n=1}^{\infty}\sum_{m=-n}^{n}\frac{2n+1}{n(n+1)}\exp[\mathrm{i}m(\varphi^{\rm sca}-\varphi^{\rm inc})]$$
$$\times[b_n\tau_{mn}(\vartheta^{\rm sca})\tau_{mn}(\vartheta^{\rm inc})+a_n\pi_{mn}(\vartheta^{\rm sca})\pi_{mn}(\vartheta^{\rm inc})]. \tag{5.148}$$

Quite naturally, now the amplitude matrix depends only on the difference of the azimuthal angles of the incident and scattered waves rather than on their specific values. The amplitude matrix becomes especially simple when the incident wave propagates along the positive direction of the *z*-axis of the laboratory reference frame and $\varphi^{\rm sca} = \varphi^{\rm inc}$:

$$S_{11}(\vartheta^{\rm sca}, \varphi^{\rm inc}; 0, \varphi^{\rm inc}) = \frac{\rm i}{k_1}\sum_{n=1}^{\infty}\frac{2n+1}{\sqrt{n(n+1)}}[b_n\pi_{1n}(\vartheta^{\rm sca}) + a_n\tau_{1n}(\vartheta^{\rm sca})]$$

$$= \frac{\rm i}{k_1}\sum_{n=1}^{\infty}\frac{2n+1}{n(n+1)}[b_n\pi_n(\vartheta^{\rm sca}) + a_n\tau_n(\vartheta^{\rm sca})], \qquad (5.149)$$

$$S_{12}(\vartheta^{\rm sca}, \varphi^{\rm inc}; 0, \varphi^{\rm inc}) = S_{21}(\vartheta^{\rm sca}, \varphi^{\rm inc}; 0, \varphi^{\rm inc}) \equiv 0, \qquad (5.150)$$

$$S_{22}(\vartheta^{\rm sca}, \varphi^{\rm inc}; 0, \varphi^{\rm inc}) = \frac{\rm i}{k_1}\sum_{n=1}^{\infty}\frac{2n+1}{\sqrt{n(n+1)}}[b_n\tau_{1n}(\vartheta^{\rm sca}) + a_n\pi_{1n}(\vartheta^{\rm sca})]$$

$$= \frac{\rm i}{k_1}\sum_{n=1}^{\infty}\frac{2n+1}{n(n+1)}[b_n\tau_n(\vartheta^{\rm sca}) + a_n\pi_n(\vartheta^{\rm sca})] \qquad (5.151)$$

(cf. Eqs. (5.16)–(5.17) and (5.110)–(5.111)), where $\pi_n = \sqrt{n(n+1)}\,\pi_{1n}$ and $\tau_n = \sqrt{n(n+1)}\,\tau_{1n}$. If we take into account that the definition of associated Legendre functions adopted by Bohren and Huffman (1983) differs from ours by a factor $(-1)^m$ and use Eqs. (B.5) and (B.28), it becomes obvious that Eqs. (5.149)–(5.151) are equivalent to Eqs. (4.74) and (4.75) of Bohren and Huffman. In view of Eq. (5.150), we can easily show that the normalized Stokes scattering matrix for a spherically symmetric particle is given by Eq. (4.65) with

$$a_1(\Theta) \equiv a_2(\Theta) = \frac{2\pi}{C_{\rm sca}}\{|S_{11}(\Theta, 0; 0, 0)|^2 + |S_{22}(\Theta, 0; 0, 0)|^2\}, \qquad (5.152)$$

$$a_3(\Theta) \equiv a_4(\Theta) = \frac{4\pi}{C_{\rm sca}}{\rm Re}\{S_{11}(\Theta, 0; 0, 0)\,S_{22}^*(\Theta, 0; 0, 0)\}, \qquad (5.153)$$

$$b_1(\Theta) = \frac{2\pi}{C_{\rm sca}}\{|S_{11}(\Theta, 0; 0, 0)|^2 - |S_{22}(\Theta, 0; 0, 0)|^2\}, \qquad (5.154)$$

$$b_2(\Theta) = \frac{4\pi}{C_{\rm sca}}{\rm Im}\{S_{11}(\Theta, 0; 0, 0)\,S_{22}^*(\Theta, 0; 0, 0)\}. \qquad (5.155)$$

Equations (5.102) and (5.140) yield

$$C_{\rm ext} = \frac{2\pi}{k_1^2}{\rm Re}\sum_{n=1}^{\infty}(2n+1)(b_n + a_n), \qquad (5.156)$$

$$C_{\rm sca} = \frac{2\pi}{k_1^2}\sum_{n=1}^{\infty}(2n+1)\{|b_n|^2 + |a_n|^2\}. \qquad (5.157)$$

One way of calculating the coefficients in the expansions (4.75)–(4.80) is to evaluate numerically the integrals in Eqs. (4.81)–(4.86) after substituting Eqs. (5.152)–(5.155). One can also use closed-form analytical formulas that directly ex-

press the expansion coefficients in terms of the Lorenz–Mie coefficients a_n and b_n and so bypass the numerical angular integration. These formulas are a special case of the general formulation outlined in Section 5.5 and are derived as follows. We first write

$$C_{++}(\Theta, 0; 0, 0) = C_{--}(\Theta, 0; 0, 0) = \frac{\mathrm{i}}{2k_1}\sum_{n=1}^{\infty}(2n+1)(b_n + a_n)d_{11}^n(\Theta), \qquad (5.158)$$

$$C_{+-}(\Theta, 0; 0, 0) = C_{-+}(\Theta, 0; 0, 0) = \frac{\mathrm{i}}{2k_1}\sum_{n=1}^{\infty}(2n+1)(b_n - a_n)d_{-11}^n(\Theta) \qquad (5.159)$$

(cf. Eqs. (4.95), (5.98), (5.99), and (5.149)–(5.151)). We then substitute Eqs. (5.158) and (5.159) into Eq. (4.97) and expand the products of two *d*-functions in the Clebsch–Gordan series of Eq. (B.50). Finally, using Eqs. (4.98), (4.105), (B.5), (B.30), and (B.33) and switching from Clebsch–Gordan coefficients to 3*j* symbols (Appendix D), which are more symmetric, we obtain

$$g_{jj}^s = \frac{\pi(2s+1)}{k_1^2 C_{\mathrm{sca}}}\left\{2\,\mathrm{Re}\sum_{n=1}^{\infty}\sum_{m=M}^{s+n}\begin{pmatrix} s & m & n \\ j & -1 & 1-j\end{pmatrix}^2(2n+1)(2m+1)(a_n^* + b_n^*)(a_m + b_m)\right.$$
$$\left. + \sum_{n=1}^{\infty}\begin{pmatrix} s & n & n \\ j & -1 & 1-j\end{pmatrix}^2(2n+1)^2|a_n + b_n|^2\right\}, \qquad j = 0, 2, \qquad (5.160)$$

$$g_{j,-j}^s = \frac{\pi(2s+1)}{k_1^2 C_{\mathrm{sca}}}\left\{2\,\mathrm{Re}\sum_{n=1}^{\infty}\sum_{m=M}^{s+n}\begin{pmatrix} s & m & n \\ j & -1 & 1-j\end{pmatrix}^2(-1)^{s+m+n}\right.$$
$$\times(2n+1)(2m+1)(a_n^* - b_n^*)(a_m - b_m)$$
$$\left. + (-1)^s\sum_{n=1}^{\infty}\begin{pmatrix} s & n & n \\ j & -1 & 1-j\end{pmatrix}^2(2n+1)^2|a_n - b_n|^2\right\}, \quad j = 0, 2, \quad (5.161)$$

$$g_{02}^s = \frac{\pi(2s+1)}{k_1^2 C_{\mathrm{sca}}}\left\{\sum_{n=1}^{\infty}\sum_{m=M}^{s+n}\begin{pmatrix} s & m & n \\ 0 & -1 & 1\end{pmatrix}\begin{pmatrix} s & m & n \\ 2 & -1 & -1\end{pmatrix}(2n+1)(2m+1)\right.$$
$$\times[(a_m^* + b_m^*)(a_n - b_n) + (-1)^{s+m+n}(a_n^* + b_n^*)(a_m - b_m)]$$
$$\left. + \sum_{n=1}^{\infty}\begin{pmatrix} s & n & n \\ 0 & -1 & 1\end{pmatrix}\begin{pmatrix} s & n & n \\ 2 & -1 & -1\end{pmatrix}(2n+1)^2(a_n^* + b_n^*)(a_n - b_n)\right\}, \quad (5.162)$$

where $M = \max(s-n, n+1)$. These formulas were first derived by Domke (1975) and later corrected by Mishchenko (1990c). Finally, the Stokes-representation expansion coefficients are calculated using Eqs. (4.109)–(4.114). An alternative analytical method for computing the expansion coefficients was developed by Bugaenko (1976).

Taking into account that

$$\begin{pmatrix} 1 & m & n \\ 0 & -1 & 1 \end{pmatrix}$$

$$= (-1)^{n+1}[(n-1)(n+2) - m(m+1)]$$

$$\times \left[\frac{n(n+1)}{(n+m)(n+m+1)(n+m+2)m(m+1)(n-m+1)!(m-n+1)!} \right]^{1/2} \tag{5.163}$$

(cf. Eq. (45) in Section 8.5 of Varshalovich *et al*. (1988) and Eq. (D.8)) and using Eqs. (4.92) and (4.109), we derive, after somewhat tedious but simple algebra,

$$\langle \cos\Theta \rangle = \frac{4\pi}{k_1^2 C_{\rm sca}} \operatorname{Re} \sum_{n=1}^{\infty} \left[\frac{n(n+2)}{n+1} (a_n a_{n+1}^* + b_n b_{n+1}^*) + \frac{2n+1}{n(n+1)} a_n b_n^* \right] \tag{5.164}$$

(Debye 1909). The radiation force exerted on the spherical particle and the cross section for radiation pressure can be found from Eqs. (4.42), (4.43), (5.156), (5.157), and (5.164).

5.8 Extended boundary condition method

The attractive mathematical formalism outlined in the previous sections would serve little practical purpose if there were no efficient numerical techniques for computing the T matrix for various kinds of particles. Fortunately, several such techniques have been developed for both simple single-body particles and clusters composed of simple monomers. In this section we will discuss the computation of the T matrix for simple particles, while the following section will deal with clusters.

5.8.1 General formulation

The standard scheme for computing the T matrix for simple particles is based on the extended boundary condition method (EBCM) developed by Waterman (1965, 1971). Consider a finite scattering object in the form of a single homogeneous body occupying a region $V_{\rm INT}$ bounded by a closed surface S and imbedded in an infinite homogeneous, isotropic, nonmagnetic, and nonabsorbing medium (Fig. 5.4). The region $V_{\rm INT}$ is filled with an isotropic nonmagnetic material and is centered at the origin of the particle reference frame. The infinite region exterior to the particle is denoted by $V_{\rm EXT}$. The electric fields in the regions $V_{\rm EXT}$ and $V_{\rm INT}$ satisfy Eqs. (2.3) and (2.4), respectively.

The vector Green's theorem for a regular surface S_1 bounding a volume V_1 is (Morse and Feshbach 1953)

$$\int_{V_1} dV [\mathbf{a} \cdot (\nabla \times \nabla \times \mathbf{b}) - \mathbf{b} \cdot (\nabla \times \nabla \times \mathbf{a})] = \int_{S_1} dS\, \hat{\mathbf{n}} \cdot [\mathbf{b} \times (\nabla \times \mathbf{a}) - \mathbf{a} \times (\nabla \times \mathbf{b})], \tag{5.165}$$

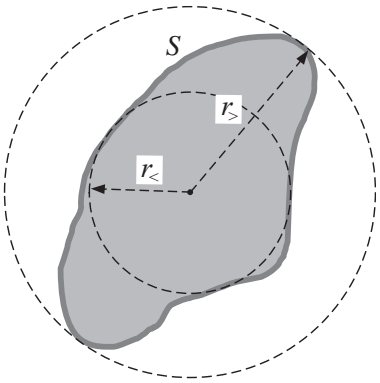

Figure 5.4. Cross section of an arbitrarily shaped, homogeneous scattering object bounded by a closed surface *S*. $r_>$ is the radius of the smallest circumscribing sphere centered at the origin of the particle coordinate system and $r_<$ is the radius of the largest concentric inscribed sphere.

where $\hat{\mathbf{n}}$ is the unit vector along the local outward normal to the surface. We apply Eq. (5.165) to the exterior region V_{EXT} and insert $\mathbf{a} = \mathbf{E}$ and $\mathbf{b} = \ddot{G}(\mathbf{r}, \mathbf{r}') \cdot \mathbf{c}$, where $\ddot{G}(\mathbf{r}, \mathbf{r}')$ is the free space dyadic Green's function, Eq. (2.13), and $\mathbf{c}$ is an arbitrary constant vector. The surface integral on the right-hand side of Eq. (5.165) is the sum of two integrals, an integral over the spherical surface S_∞ bounding the exterior region at infinity and an integral over the particle surface *S*. In view of Eqs. (2.3) and (2.8), Eq. (5.165) becomes

$$\left.\begin{array}{ll} \mathbf{E}(\mathbf{r}') \cdot \mathbf{c} & \text{if } \mathbf{r}' \in V_{\mathrm{EXT}} \\ 0 & \text{if } \mathbf{r}' \in V_{\mathrm{INT}} \end{array}\right\} = \left[-\int_{S_\infty} + \int_S \right] \mathrm{d}S\, \hat{\mathbf{n}} \cdot \big([\nabla \times \mathbf{E}(\mathbf{r})] \times [\ddot{G}(\mathbf{r}, \mathbf{r}') \cdot \mathbf{c}] + \mathbf{E}(\mathbf{r}) \times \{\nabla \times [\ddot{G}(\mathbf{r}, \mathbf{r}') \cdot \mathbf{c}]\} \big), \quad (5.166)$$

where $\hat{\mathbf{n}}$ is the local normal at either S_∞ or *S*; it is directed away from the particle. Since $\mathbf{c}$ is arbitrary, it can be cancelled out on both sides of Eq. (5.166). In view of Eqs. (2.20), (2.21), and (2.24), the contribution of the scattered field to the integral over S_∞ on the right-hand side of Eq. (5.166) vanishes. Therefore, the integral over S_∞ is independent of the presence of the particle and thus supplies the incident field at $\mathbf{r}'$. Hence we have for $\mathbf{r}' \in V_{\mathrm{EXT}}$

$$\mathbf{E}(\mathbf{r}') = \mathbf{E}^{\mathrm{inc}}(\mathbf{r}') + \mathbf{E}^{\mathrm{sca}}(\mathbf{r}'), \quad (5.167)$$

$$\mathbf{E}^{\mathrm{sca}}(\mathbf{r}') = \int_S \mathrm{d}S \{ \mathrm{i}\omega\mu_0 [\hat{\mathbf{n}} \times \mathbf{H}_+(\mathbf{r})] \cdot \ddot{G}(\mathbf{r}, \mathbf{r}') + [\hat{\mathbf{n}} \times \mathbf{E}_+(\mathbf{r})] \cdot [\nabla \times \ddot{G}(\mathbf{r}, \mathbf{r}')] \}, \quad (5.168)$$

where we have used Eq. (2.1) with $\mu_1 = \mu_0$ and the identities

$$\mathbf{a} \cdot (\mathbf{b} \times \mathbf{c}) = (\mathbf{a} \times \mathbf{b}) \cdot \mathbf{c}, \quad (5.169)$$

$$\mathbf{a} \cdot (\mathbf{b} \times \ddot{C}) = (\mathbf{a} \times \mathbf{b}) \cdot \ddot{C}. \quad (5.170)$$

The subscript plus in Eq. (5.168) indicates that the electric and magnetic fields inside the integral are those on the *exterior* side of the surface *S*. For $\mathbf{r}' \in V_{\mathrm{INT}}$,

$$\mathbf{E}^{\rm inc}(\mathbf{r}') = -\int_S {\rm d}S\{{\rm i}\omega\mu_0[\hat{\mathbf{n}}\times\mathbf{H}_+(\mathbf{r})]\cdot\ddot{G}(\mathbf{r},\mathbf{r}') + [\hat{\mathbf{n}}\times\mathbf{E}_+(\mathbf{r})]\cdot[\nabla\times\ddot{G}(\mathbf{r},\mathbf{r}')]\}. \tag{5.171}$$

Equation (5.171) is called the extended boundary condition because it analytically extends $\mathbf{r}'$ to the interior region. The gist of the extended boundary condition method is that one finds the fields $\mathbf{E}_+(\mathbf{r})$ and $\mathbf{H}_+(\mathbf{r})$ on the exterior side of the particle surface using Eq. (5.171) and, assuming that the incident field is known, then calculates the scattered field using Eq. (5.168).

The free space dyadic Green's function can be expressed in terms of vector spherical wave functions according to Eq. (C.61). Let $r_>$ be the radius of the smallest circumscribing sphere of the scattering particle centered at the origin and $r_<$ be the radius of the largest concentric inscribed sphere (cf. Fig. 5.4). For all $r' < r_<$ and all r on S, we have $r' < r$. Therefore, substituting Eq. (C.61) in Eq. (5.171), we obtain

$$\mathbf{E}^{\rm inc}(\mathbf{r}') = \sum_{n=1}^{\infty}\sum_{m=-n}^{n}[a_{mn}{\rm Rg}\mathbf{M}_{mn}(k_1\mathbf{r}') + b_{mn}{\rm Rg}\mathbf{N}_{mn}(k_1\mathbf{r}')], \quad r' < r_<, \tag{5.172}$$

$$\begin{aligned}\begin{matrix}a_{mn}\\ b_{mn}\end{matrix} = k_1(-1)^m\int_S {\rm d}S\Bigg\{&\omega\mu_0[\hat{\mathbf{n}}\times\mathbf{H}_+(\mathbf{r})]\cdot\begin{matrix}\mathbf{M}_{-mn}(k_1r,\vartheta,\varphi)\\ \mathbf{N}_{-mn}(k_1r,\vartheta,\varphi)\end{matrix}\\ &-{\rm i}k_1[\hat{\mathbf{n}}\times\mathbf{E}_+(\mathbf{r})]\cdot\begin{matrix}\mathbf{N}_{-mn}(k_1r,\vartheta,\varphi)\\ \mathbf{M}_{-mn}(k_1r,\vartheta,\varphi)\end{matrix}\Bigg\}.\end{aligned} \tag{5.173}$$

Similarly, for all $r' > r_>$ and all r on S, we have $r < r'$. Therefore, substituting Eq. (C.61) into Eq. (5.168) yields

$$\mathbf{E}^{\rm sca}(\mathbf{r}') = \sum_{n=1}^{\infty}\sum_{m=-n}^{n}[p_{mn}\mathbf{M}_{mn}(k_1\mathbf{r}') + q_{mn}\mathbf{N}_{mn}(k_1\mathbf{r}')], \quad r' > r_>, \tag{5.174}$$

$$\begin{aligned}\begin{matrix}p_{mn}\\ q_{mn}\end{matrix} = -k_1(-1)^m\int_S {\rm d}S\Bigg\{&\omega\mu_0[\hat{\mathbf{n}}\times\mathbf{H}_+(\mathbf{r})]\cdot\begin{matrix}{\rm Rg}\mathbf{M}_{-mn}(k_1r,\vartheta,\varphi)\\ {\rm Rg}\mathbf{N}_{-mn}(k_1r,\vartheta,\varphi)\end{matrix}\\ &-{\rm i}k_1[\hat{\mathbf{n}}\times\mathbf{E}_+(\mathbf{r})]\cdot\begin{matrix}{\rm Rg}\mathbf{N}_{-mn}(k_1r,\vartheta,\varphi)\\ {\rm Rg}\mathbf{M}_{-mn}(k_1r,\vartheta,\varphi)\end{matrix}\Bigg\}.\end{aligned} \tag{5.175}$$

In order to compute the expansion coefficients of the scattered field via Eq. (5.175), we need first to find the electric and magnetic fields on the exterior side of the particle surface from Eq. (5.173). We will assume that the electric field everywhere inside the scattering object can be expanded in regular vector spherical wave functions of the *interior* wave equation:

$$\mathbf{E}(\mathbf{r}) = \sum_{n'=1}^{\infty}\sum_{m'=-n'}^{n'}[c_{m'n'}{\rm Rg}\mathbf{M}_{m'n'}(k_2\mathbf{r}) + d_{m'n'}{\rm Rg}\mathbf{N}_{m'n'}(k_2\mathbf{r})], \quad \mathbf{r}\in V_{\rm INT}, \tag{5.176}$$

where k_2 is the wave number in the interior region. In view of Eq. (2.2) with $\mu_2(\mathbf{r}) \equiv \mu_0$ and Eqs. (C.14) and (C.15), the matching magnetic field expansion is

$$\mathbf{H}(\mathbf{r}) = \frac{k_2}{{\rm i}\omega\mu_0}\sum_{n'=1}^{\infty}\sum_{m'=-n'}^{n'}[d_{m'n'}{\rm Rg}\mathbf{M}_{m'n'}(k_2\mathbf{r}) + c_{m'n'}{\rm Rg}\mathbf{N}_{m'n'}(k_2\mathbf{r})], \quad \mathbf{r}\in V_{\rm INT}. \tag{5.177}$$

The boundary conditions require continuity of the tangential components of the electric and magnetic fields, i.e.,

$$\left.\begin{aligned}\hat{\mathbf{n}}\times\mathbf{E}_{+}(\mathbf{r})&=\hat{\mathbf{n}}\times\mathbf{E}_{-}(\mathbf{r})\\ \hat{\mathbf{n}}\times\mathbf{H}_{+}(\mathbf{r})&=\hat{\mathbf{n}}\times\mathbf{H}_{-}(\mathbf{r})\end{aligned}\right\},\qquad \mathbf{r}\in S, \tag{5.178}$$

where the subscript minus labels the fields on the *interior* side of the particle surface (cf. Eqs. (1.13) and (1.15)). Substituting Eqs. (5.176)–(5.178) into Eq. (5.173) and using Eq. (5.169), we have

$$\begin{bmatrix}\mathbf{a}\\ \mathbf{b}\end{bmatrix}=\mathbf{Q}\begin{bmatrix}\mathbf{c}\\ \mathbf{d}\end{bmatrix}=\begin{bmatrix}\mathbf{Q}^{11} & \mathbf{Q}^{12}\\ \mathbf{Q}^{21} & \mathbf{Q}^{22}\end{bmatrix}\begin{bmatrix}\mathbf{c}\\ \mathbf{d}\end{bmatrix}, \tag{5.179}$$

where

$$Q^{11}_{mnm'n'}=-\mathrm{i}k_1k_2J^{21}_{mnm'n'}-\mathrm{i}k_1^2J^{12}_{mnm'n'}, \tag{5.180}$$

$$Q^{12}_{mnm'n'}=-\mathrm{i}k_1k_2J^{11}_{mnm'n'}-\mathrm{i}k_1^2J^{22}_{mnm'n'}, \tag{5.181}$$

$$Q^{21}_{mnm'n'}=-\mathrm{i}k_1k_2J^{22}_{mnm'n'}-\mathrm{i}k_1^2J^{11}_{mnm'n'}, \tag{5.182}$$

$$Q^{22}_{mnm'n'}=-\mathrm{i}k_1k_2J^{12}_{mnm'n'}-\mathrm{i}k_1^2J^{21}_{mnm'n'}, \tag{5.183}$$

and

$$\begin{bmatrix}J^{11}_{mnm'n'}\\ J^{12}_{mnm'n'}\\ J^{21}_{mnm'n'}\\ J^{22}_{mnm'n'}\end{bmatrix}=(-1)^m\int_S \mathrm{d}S\,\hat{\mathbf{n}}\cdot\begin{bmatrix}\mathrm{Rg}\mathbf{M}_{m'n'}(k_2r,\vartheta,\varphi)\times\mathbf{M}_{-mn}(k_1r,\vartheta,\varphi)\\ \mathrm{Rg}\mathbf{M}_{m'n'}(k_2r,\vartheta,\varphi)\times\mathbf{N}_{-mn}(k_1r,\vartheta,\varphi)\\ \mathrm{Rg}\mathbf{N}_{m'n'}(k_2r,\vartheta,\varphi)\times\mathbf{M}_{-mn}(k_1r,\vartheta,\varphi)\\ \mathrm{Rg}\mathbf{N}_{m'n'}(k_2r,\vartheta,\varphi)\times\mathbf{N}_{-mn}(k_1r,\vartheta,\varphi)\end{bmatrix}. \tag{5.184}$$

Similarly, substituting Eqs. (5.176)–(5.178) into Eq. (5.175) yields

$$\begin{bmatrix}\mathbf{p}\\ \mathbf{q}\end{bmatrix}=-\mathrm{Rg}\mathbf{Q}\begin{bmatrix}\mathbf{c}\\ \mathbf{d}\end{bmatrix}=-\begin{bmatrix}\mathrm{Rg}\mathbf{Q}^{11} & \mathrm{Rg}\mathbf{Q}^{12}\\ \mathrm{Rg}\mathbf{Q}^{21} & \mathrm{Rg}\mathbf{Q}^{22}\end{bmatrix}\begin{bmatrix}\mathbf{c}\\ \mathbf{d}\end{bmatrix}, \tag{5.185}$$

where

$$\mathrm{Rg}Q^{11}_{mnm'n'}=-\mathrm{i}k_1k_2\mathrm{Rg}J^{21}_{mnm'n'}-\mathrm{i}k_1^2\,\mathrm{Rg}J^{12}_{mnm'n'}, \tag{5.186}$$

$$\mathrm{Rg}Q^{12}_{mnm'n'}=-\mathrm{i}k_1k_2\mathrm{Rg}J^{11}_{mnm'n'}-\mathrm{i}k_1^2\,\mathrm{Rg}J^{22}_{mnm'n'}, \tag{5.187}$$

$$\mathrm{Rg}Q^{21}_{mnm'n'}=-\mathrm{i}k_1k_2\mathrm{Rg}J^{22}_{mnm'n'}-\mathrm{i}k_1^2\,\mathrm{Rg}J^{11}_{mnm'n'}, \tag{5.188}$$

$$\mathrm{Rg}Q^{22}_{mnm'n'}=-\mathrm{i}k_1k_2\mathrm{Rg}J^{12}_{mnm'n'}-\mathrm{i}k_1^2\,\mathrm{Rg}J^{21}_{mnm'n'}, \tag{5.189}$$

and

$$\begin{bmatrix}\mathrm{Rg}J^{11}_{mnm'n'}\\ \mathrm{Rg}J^{12}_{mnm'n'}\\ \mathrm{Rg}J^{21}_{mnm'n'}\\ \mathrm{Rg}J^{22}_{mnm'n'}\end{bmatrix}=(-1)^m\int_S \mathrm{d}S\,\hat{\mathbf{n}}\cdot\begin{bmatrix}\mathrm{Rg}\mathbf{M}_{m'n'}(k_2r,\vartheta,\varphi)\times\mathrm{Rg}\mathbf{M}_{-mn}(k_1r,\vartheta,\varphi)\\ \mathrm{Rg}\mathbf{M}_{m'n'}(k_2r,\vartheta,\varphi)\times\mathrm{Rg}\mathbf{N}_{-mn}(k_1r,\vartheta,\varphi)\\ \mathrm{Rg}\mathbf{N}_{m'n'}(k_2r,\vartheta,\varphi)\times\mathrm{Rg}\mathbf{M}_{-mn}(k_1r,\vartheta,\varphi)\\ \mathrm{Rg}\mathbf{N}_{m'n'}(k_2r,\vartheta,\varphi)\times\mathrm{Rg}\mathbf{N}_{-mn}(k_1r,\vartheta,\varphi)\end{bmatrix}. \tag{5.190}$$

Comparing Eqs. (5.8), (5.179), and (5.185), we finally derive

$$\mathbf{T}(P) = -(\mathrm{Rg}\mathbf{Q})\,\mathbf{Q}^{-1}. \tag{5.191}$$

This formula expresses the elements of the T matrix in terms of integrals of vector products of vector spherical wave functions over the particle surface. The surface integrals in Eqs. (5.184) and (5.190) are usually calculated using appropriate coordinate systems and quadrature formulas. For example, in spherical coordinates the surface S is defined by the formula

$$\mathbf{r}(\vartheta, \varphi) = r(\vartheta, \varphi)\hat{\mathbf{r}}, \tag{5.192}$$

and we have (cf. Guggenheimer 1977)

$$\begin{aligned} \mathrm{d}S\hat{\mathbf{n}}(\mathbf{r}) &= \left[\frac{\partial \mathbf{r}}{\partial \vartheta} \times \frac{\partial \mathbf{r}}{\partial \varphi}\right] \mathrm{d}\vartheta\,\mathrm{d}\varphi \\ &= \left[r^2 \sin\vartheta\,\hat{\mathbf{r}} - r\sin\vartheta \frac{\partial r}{\partial \vartheta}\hat{\boldsymbol{\vartheta}} - r\frac{\partial r}{\partial \varphi}\hat{\boldsymbol{\varphi}}\right] \mathrm{d}\vartheta\,\mathrm{d}\varphi. \end{aligned} \tag{5.193}$$

Our derivation of the EBCM is similar to those given by Waterman (1971) and Tsang *et al.* (1985) and explicitly avoids invoking the Rayleigh hypothesis (cf. Section 5.1). Alternative derivations and formulations have been discussed by Barber and Yeh (1975), Ström (1975), Agarwal (1976), Bates and Wall (1977), Morita (1979), and Ström and Zheng (1987). The derivation given by Waterman (1979) made it especially clear that the EBCM is not based on the Rayleigh hypothesis and that the scattering objects need not be convex and close to spherical in order to ensure the validity of the method. It is interesting that in fact the EBCM can be derived from the Rayleigh hypothesis (Bates 1975; Chew 1995; Schmidt *et al.* 1998). This does not mean, however, that the EBCM is equivalent to the Rayleigh hypothesis or requires it to be valid (Lewin 1970). The equivalence of the two approaches would follow from a reciprocal derivation of the Rayleigh hypothesis from the EBCM, but it remains unclear whether such a derivation exists.

Peterson and Ström (1974) extended the EBCM to layered scatterers (see also Bringi and Seliga 1977; Wang and Barber 1979). Scattering by more general composite objects was considered by Ström and Zheng (1988) and Zheng and Ström (1989). Lakhtakia *et al.* (1985b) and Lakhtakia (1991) applied the EBCM to light scattering by chiral particles embedded in an achiral isotropic or chiral host medium.

The EBCM is a quite general technique and is applicable to arbitrarily shaped homogeneous and composite particles. However, relatively few attempts have been made to compute light scattering by bodies lacking rotational symmetry such as triaxial ellipsoids (Schneider and Peden 1988; Schneider *et al.* 1991), cubes (Laitinen and Lumme 1998; Wriedt and Comberg 1998; Wriedt and Doicu 1998a), finite hexagonal cylinders (Baran *et al.* 2001a,b; Havemann and Baran 2001), and general polyhedral cylinders of finite length (Kahnert 2001a). As we will show in subsection 5.8.3, Eqs. (5.180)–(5.184) and (5.186)–(5.190) become much simpler for bodies with

rotation symmetry and result in more efficient computer algorithms. Furthermore, we have seen in earlier sections of this chapter that the computation of scattering and absorption characteristics for rotationally symmetric particles in fixed, partial, and random orientations is also significantly less involved, owing to the symmetry relations (5.36) and (5.37). This explains why many EBCM codes have been specifically designed to deal with rotationally symmetric scatterers (e.g., Wiscombe and Mugnai 1986; Barber and Hill 1990; Mishchenko and Travis 1998; Quirantes 1999).

5.8.2 Scale invariance rule

Examination of Eqs. (5.180)–(5.184) and (5.186)–(5.191) leads to an important result, as follows. If we multiply all particle dimensions by a constant factor f (thereby not changing the particle shape) and multiply the wave numbers k_1 and k_2 for the exterior and interior regions, respectively, by the factor $1/f$ then the elements of the T matrix do not change. This "scale invariance" rule can be reformulated as follows. If the particle geometry is characterized by the shape and a typical dimension a (for example, the largest or the smallest particle dimension or the radius of a surface- or volume-equivalent sphere) then the elements of the T matrix do not depend on specific values of a, k_1, and k_2, but rather depend on the product of a and k_1, traditionally called the size parameter x, and the ratio of k_2 to k_1, which is simply the relative refractive index $m = k_2/k_1 = m_2/m_1$. (The size parameter can also be expressed, in terms of the wavelength of the incident wave in the exterior region $\lambda_1 = 2\pi/k_1$, as $x = 2\pi a/\lambda_1$.) Obviously, all scattering characteristics that involve only the elements of the T matrix also obey the scale invariance rule. Equations (5.11)–(5.14) show that the products of k_1 and the elements of the amplitude matrix are such characteristics. As a consequence, the scale invariance rule is also obeyed by: the products of k_1^2 and the elements of the phase and scattering matrices; the products of k_1^2 and the optical cross sections; the products of k_1^2 and the extinction matrix elements; the efficiency factors; the elements of the normalized scattering matrix; the coefficients in the expansions of the elements of the normalized scattering matrix in generalized spherical functions; the single-scattering albedo; and the asymmetry parameter. In general, the scale invariance rule applies to any dimensionless scattering characteristic. Although we have explicitly derived the scale invariance rule only for homogeneous particles, it can be shown to follow from Eqs. (2.18) and (2.27) for particles with arbitrary morphology (Mishchenko 2005).

The scale invariance rule can be very helpful in practice because it makes a single computation or measurement applicable to all couplets {size, wavelength} with the same ratio of size to wavelength, provided that the relative refractive index does not change. In particular, we will see in Section 8.2 that this rule underlies the basic idea of the microwave analog technique for laboratory measurements of electromagnetic scattering by small particles.

5.8.3 Rotationally symmetric particles

If the scattering particle is rotationally symmetric and the z-axis of the particle reference frame is directed along the axis of rotation then

$$\mathbf{r}(\vartheta,\varphi) = r(\vartheta)\hat{\mathbf{r}}, \tag{5.194}$$

$$\mathrm{d}S\hat{\mathbf{n}}(\mathbf{r}) = r^2\sin\vartheta\left(\hat{\mathbf{r}} - \frac{r_\vartheta}{r}\hat{\boldsymbol{\vartheta}}\right)\mathrm{d}\vartheta\,\mathrm{d}\varphi, \tag{5.195}$$

where $r_\vartheta = \partial r/\partial\vartheta$. Therefore, the φ-integration in Eq. (5.184) gives simply $2\pi\delta_{mm'}$ (cf. Eq. (5.75)). Using Appendix C and Eqs. (5.16) and (5.17), we get

$$J^{11}_{mnm'n'} = -\frac{\mathrm{i}}{2}\delta_{mm'}\left[\frac{(2n+1)(2n'+1)}{n(n+1)n'(n'+1)}\right]^{1/2}$$
$$\times\int_{-1}^{+1}\mathrm{d}(\cos\vartheta)r^2 h_n^{(1)}(k_1r)\,j_{n'}(k_2r)[\pi_{mn}(\vartheta)\tau_{mn'}(\vartheta)+\tau_{mn}(\vartheta)\pi_{mn'}(\vartheta)], \tag{5.196}$$

$$J^{12}_{mnm'n'} = \frac{1}{2}\delta_{mm'}\left[\frac{(2n+1)(2n'+1)}{n(n+1)n'(n'+1)}\right]^{1/2}$$
$$\times\int_{-1}^{+1}\mathrm{d}(\cos\vartheta)r^2\,j_{n'}(k_2r)\left\{\frac{1}{k_1r}\frac{\mathrm{d}}{\mathrm{d}(k_1r)}[k_1rh_n^{(1)}(k_1r)]\right.$$
$$\left.\times[\pi_{mn}(\vartheta)\pi_{mn'}(\vartheta)+\tau_{mn}(\vartheta)\tau_{mn'}(\vartheta)]+\frac{r_\vartheta}{r}n(n+1)\frac{h_n^{(1)}(k_1r)}{k_1r}d^n_{0m}(\vartheta)\tau_{mn'}(\vartheta)\right\}, \tag{5.197}$$

$$J^{21}_{mnm'n'} = -\frac{1}{2}\delta_{mm'}\left[\frac{(2n+1)(2n'+1)}{n(n+1)n'(n'+1)}\right]^{1/2}$$
$$\times\int_{-1}^{+1}\mathrm{d}(\cos\vartheta)r^2h_n^{(1)}(k_1r)\left\{\frac{1}{k_2r}\frac{\mathrm{d}}{\mathrm{d}(k_2r)}[k_2rj_{n'}(k_2r)]\right.$$
$$\left.\times[\pi_{mn}(\vartheta)\pi_{mn'}(\vartheta)+\tau_{mn}(\vartheta)\tau_{mn'}(\vartheta)]+\frac{r_\vartheta}{r}n'(n'+1)\frac{j_{n'}(k_2r)}{k_2r}\tau_{mn}(\vartheta)d^{n'}_{0m}(\vartheta)\right\}, \tag{5.198}$$

$$J^{22}_{mnm'n'} = -\frac{\mathrm{i}}{2}\delta_{mm'}\left[\frac{(2n+1)(2n'+1)}{n(n+1)n'(n'+1)}\right]^{1/2}$$
$$\times\int_{-1}^{+1}\mathrm{d}(\cos\vartheta)r^2\left(\frac{1}{k_1r}\frac{\mathrm{d}}{\mathrm{d}(k_1r)}[k_1rh_n^{(1)}(k_1r)]\frac{1}{k_2r}\frac{\mathrm{d}}{\mathrm{d}(k_2r)}[k_2rj_{n'}(k_2r)]\right.$$
$$\times[\pi_{mn}(\vartheta)\tau_{mn'}(\vartheta)+\tau_{mn}(\vartheta)\pi_{mn'}(\vartheta)]$$
$$+\frac{r_\vartheta}{r}\left\{n(n+1)\frac{h_n^{(1)}(k_1r)}{k_1r}\frac{1}{k_2r}\frac{\mathrm{d}}{\mathrm{d}(k_2r)}[k_2rj_{n'}(k_2r)]\right.$$
$$\left.\left.+\frac{1}{k_1r}\frac{\mathrm{d}}{\mathrm{d}(k_1r)}[k_1rh_n^{(1)}(k_1r)]n'(n'+1)\frac{j_{n'}(k_2r)}{k_2r}\right\}\pi_{mn}(\vartheta)d^{n'}_{0m}(\vartheta)\right). \tag{5.199}$$

Corresponding formulas for $\mathrm{Rg}J^{kl}_{mnm'n'}$ are obtained from Eqs. (5.196)–(5.199) by replacing $h_n^{(1)}(k_1 r)$ with $j_n(k_1 r)$. Equations (5.196)–(5.199) are equivalent to Eqs. (39a)–(39d) on pp. 187 and 188 of Tsang *et al.* (1985), but we use Wigner *d*-functions instead of associated Legendre functions. As discussed in Appendix B, the computation of the Wigner *d*-functions using the recurrence relation of Eq. (B.22) is numerically stable and accurate, whereas the corresponding recurrence relation for the associated Legendre functions leads to computer overflows for large n and $|m|$.

Equations (5.179)–(5.191) and (5.196)–(5.199) show that the matrices $\mathbf{Q}$, $\mathrm{Rg}\mathbf{Q}$, and $\mathbf{T}(P)$ can be regrouped such that they become block-diagonal with each block corresponding to a different m. Since there is no coupling between the different m indices, each block is independent of all other blocks and can be computed separately. This results in significant savings of computer resources, especially for particles larger than the wavelength. An additional saving of computer time can be achieved by restricting the computer calculations to non-negative m and using the symmetry relation (5.37). Since $\pi_{0n}(\vartheta) \equiv 0$ (cf. Eq. (5.16)), Eqs. (5.196) and (5.199) yield

$$Q^{12}_{0n0n'} \equiv 0, \qquad Q^{21}_{0n0n'} \equiv 0, \tag{5.200}$$

$$\mathrm{Rg}Q^{12}_{0n0n'} \equiv 0, \qquad \mathrm{Rg}Q^{21}_{0n0n'} \equiv 0. \tag{5.201}$$

Therefore, $T^{12}_{0n0n'}(P) \equiv 0$ and $T^{21}_{0n0n'}(P) \equiv 0$, in agreement with Eq. (5.37).

The integrals in Eqs. (5.196)–(5.199) are usually evaluated by means of a Gauss quadrature applied to the interval $[-1, +1]$:

$$\int_{-1}^{+1} \mathrm{d}x\, f(x) \approx \sum_{p=1}^{N_\mathrm{G}} w_p f(x_p), \tag{5.202}$$

where x_p and w_p are quadrature division points and weights, respectively (e.g., Krylov 1962; Abramowitz and Stegun 1964). The quadrature must contain a large enough number N_G of division points to resolve the angular variation of the integrands, which may be very rapid for highly aspherical particles.

For particles with a plane of symmetry perpendicular to the axis of rotation, such as spheroids and circular cylinders,

$$r(\pi - \vartheta) = r(\vartheta), \tag{5.203}$$

$$r_\vartheta(\pi - \vartheta) = -r_\vartheta(\vartheta). \tag{5.204}$$

Therefore, the symmetry relations (cf. Eqs. (5.16), (5.17), (5.32), (5.33), and (B.7))

$$\pi_{mn}(\pi - \vartheta) = (-1)^{m+n} \pi_{mn}(\vartheta), \tag{5.205}$$

$$\tau_{mn}(\pi - \vartheta) = (-1)^{m+n+1} \tau_{mn}(\vartheta), \tag{5.206}$$

$$d^n_{0m}(\pi - \vartheta) = (-1)^{m+n} d^n_{0m}(\vartheta) \tag{5.207}$$

and Eqs. (5.196)–(5.199) yield

$$Q^{11}_{mnmn'} = Q^{22}_{mnmn'} = \mathrm{Re}\,Q^{11}_{mnmn'} = \mathrm{Re}\,Q^{22}_{mnmn'} = 0 \tag{5.208}$$

unless $n+n'$ is even and

$$Q^{12}_{mnmn'} = Q^{21}_{mnmn'} = \mathrm{Re}\,Q^{12}_{mnmn'} = \mathrm{Re}\,Q^{21}_{mnmn'} = 0 \tag{5.209}$$

unless $n+n'$ is odd, in full agreement with Eqs. (5.39) and (5.40). Equations (5.208) and (5.209) reduce the number of non-vanishing matrix elements by a factor of 2. Furthermore, the non-vanishing elements are computed twice as fast because one can restrict the summation in Eq. (5.202) to $1 \le p \le N_{\mathrm{G}}/2$ (assuming that N_{G} is even) and then double the result.

5.8.4 Convergence

Although expansions (5.2), (5.3) and (5.6), (5.7) and hence the T matrix are infinite, in general, in practical computer calculations they must be cut off to a finite size by truncating all expansions at an $n = n_{\max}$. This size depends on the required accuracy of computations and is found by increasing the size of the $\mathbf{Q}$ and $\mathrm{Re}\mathbf{Q}$ matrices in Eq. (5.191) until an accuracy criterion is satisfied. As an example, the dotted curve in Fig. 5.5(a) shows the quantity

$$\max\left\{\frac{\left|\langle C_{\mathrm{ext}}(n_{\max})\rangle - \langle C_{\mathrm{ext}}(n_{\max}-1)\rangle\right|}{\langle C_{\mathrm{ext}}(n_{\max})\rangle}, \frac{\left|\langle C_{\mathrm{sca}}(n_{\max})\rangle - \langle C_{\mathrm{sca}}(n_{\max}-1)\rangle\right|}{\langle C_{\mathrm{sca}}(n_{\max})\rangle}\right\} \tag{5.210}$$

versus $n_{\max}$ for randomly oriented oblate spheroids with an aspect ratio of 3, relative refractive index $m = 1.5 + \mathrm{i}0.02$, and surface-equivalent-sphere size parameter $x_{\mathrm{s}} = 2\pi r_{\mathrm{s}}/\lambda_1 = 15$, where r_{s} is the surface-equivalent-sphere radius and $\lambda_1 = 2\pi/k_1$ is the wavelength of the incident light in the surrounding medium. The results were obtained with a FORTRAN code employing double-precision (REAL*8 and COMPLEX*16) floating-point variables. The matrix $\mathbf{Q}$ was inverted using the standard Gaussian elimination scheme with partial pivoting (Forsythe *et al.* 1977). It is apparent that, for these particles, the EBCM provides a good convergence rate and excellent numerical accuracy.

It turns out, however, that numerical stability of the EBCM can become significantly worse in calculations for (partially) concave particles and particles with very large real and/or imaginary parts of the relative refractive index, large size parameters, and/or extreme geometries such as spheroids or cylinders with large aspect ratios. The broken curve in Fig. 5.5(a) exemplifies the unstable behavior of the double-precision EBCM calculations for a more challenging case of randomly oriented prolate spheroids with an aspect ratio of 4, relative refractive index $m = 1.5 + \mathrm{i}0.02$, and surface-equivalent-sphere size parameter $x_{\mathrm{s}} = 16$. The instability arises because different elements of the matrix $\mathbf{Q}$ can differ by many orders of magnitude, thereby making the numerical calculation of the inverse matrix $\mathbf{Q}^{-1}$ an ill-conditioned

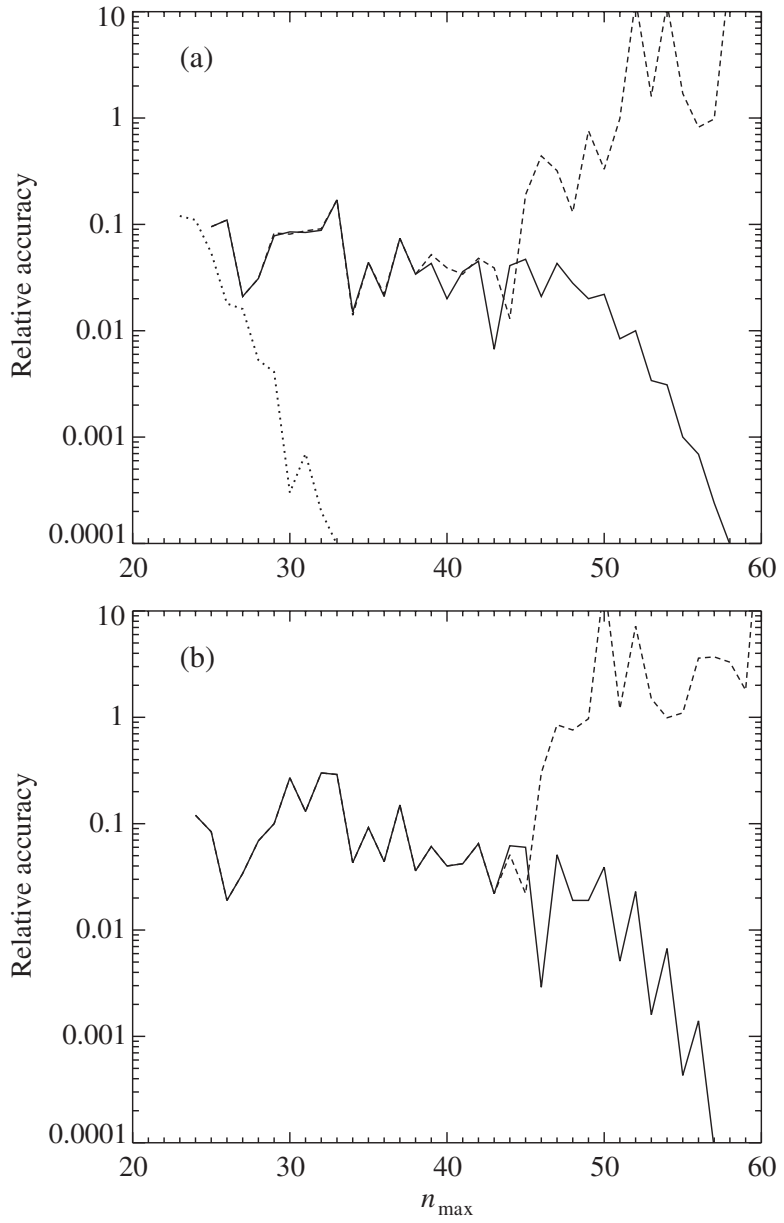

Figure 5.5. Convergence of different EBCM codes in computations for various kinds of particle (see text).

process strongly influenced by round-off errors. Because of this ill-conditioned nature, even small numerical errors in the computed elements of the $\mathbf{Q}$ matrix can result in large errors in the elements of the inverse matrix $\mathbf{Q}^{-1}$. The round-off errors become increasingly significant with increasing particle size parameter and/or aspect ratio and rapidly accumulate with increasing size of the $\mathbf{Q}$ matrix. As a result, the EBCM computations can become very slowly convergent or even divergent (Barber 1977; Varadan and Varadan 1980; Wiscombe and Mugnai 1986).

Efficient approaches for overcoming the numerical-instability problem in computing the T matrix for highly elongated particles are the so-called iterative EBCM (IEBCM) and a closely related multiple multipole EBCM (otherwise known as the null-field method with discrete sources) (Iskander *et al.* 1983, 1989b; Doicu and Wriedt 1997a,b; Wriedt and Doicu 1998a; Doicu 1999; Doicu *et al.* 2000). The main idea of the IEBCM is to represent the internal field by several sub-domain spherical function expansions centered on the major axis of an elongated scatterer. These sub-domain expansions are linked to each other by being explicitly matched in the appropriate overlapping zones. The IEBCM has been used to compute light scattering and absorption by highly elongated, absorbing and weakly absorbing dielectric scatterers with aspect ratios as large as 17. In some cases the use of the IEBCM instead of the regular EBCM has permitted stable computations at more than quadruple the former maximal convergent size parameter.

The disadvantage of the IEBCM is that its numerical stability is achieved at the expense of a considerable increase in computer code complexity and required computer time. Moreover, the IEBCM does not generate a single-expansion T matrix that could be used in the analytical orientation-averaging procedures. The latter problem was specifically addressed by Doicu and Wriedt (1999).

Mishchenko and Travis (1994a) showed that an efficient general approach to stabilizing the numerical process of inverting the $\mathbf{Q}$ matrix is to improve the accuracy with which this matrix is calculated and inverted. Specifically, they suggested calculating the elements of the $\mathbf{Q}$ matrix and performing the matrix inversion using extended-precision (REAL*16 and COMPLEX*32) instead of double-precision floating-point variables. As an example, the solid curve in Fig. 5.5(a) was computed using an extended-precision EBCM code and shows a good convergence rate and a quite acceptable accuracy for the same particles that could not be handled by the double-precision code (the broken curve). Extensive checks have demonstrated that using the extended-precision EBCM code more than doubles the maximal size parameter for which convergent results can be obtained. Timing tests performed on IBM RISC workstations have shown that the use of extended-precision arithmetic slows down computations by a factor of only 5–6. The key features of this approach are its simplicity and the fact that little additional programming effort and extra memory are required.

The numerical instability of the EBCM becomes especially noticeable for nonabsorbing or weakly absorbing particles. To ameliorate this problem, Waterman (1973) and Lakhtakia *et al.* (1984, 1985a) proposed to exploit the unitarity property of the T matrix for nonabsorbing scatterers, Eq. (5.59). Their technique is based on the so-called iterative orthogonalization of the T matrix and generates numerically stable results for elongated and flattened spheroids with large aspect ratios. The obvious disadvantage of this technique is that it applies only to particles with zero absorption. Wielaard *et al.* (1997) demonstrated that a superior approach is to invert the $\mathbf{Q}$ matrix using a special form of the so-called LU-factorization method. This approach is applicable to absorbing as well as nonabsorbing particles and increases the maximal

convergent size parameter for nonabsorbing and weakly absorbing scatterers several times. Figure 5.5(b) illustrates the performance of this technique in application to randomly oriented prolate spheroids with an aspect ratio of 4, relative refractive index $m = 1.5$, and surface-equivalent-sphere size parameter $x_s = 16$. The broken curve shows that the extended-precision EBCM code based on the Gaussian elimination scheme with partial pivoting fails to produce convergence, whereas the extended-precision code exploiting the special LU-factorization method generates very accurate results.

5.8.5 Lorenz–Mie coefficients

Consider finally the simplest case, a homogeneous spherical particle having a radius a. Using Eqs. (5.98), (5.99), and (B.17), it is easy to show that

$$\int_{-1}^{+1} \mathrm{d}(\cos\vartheta)[\pi_{mn}(\vartheta)\tau_{mn'}(\vartheta) + \tau_{mn}(\vartheta)\pi_{mn'}(\vartheta)] = 0 \tag{5.211}$$

and

$$\int_{-1}^{+1} \mathrm{d}(\cos\vartheta)[\pi_{mn}(\vartheta)\pi_{mn'}(\vartheta) + \tau_{mn}(\vartheta)\tau_{mn'}(\vartheta)] = \frac{2n(n+1)}{2n+1}\delta_{nn'}. \tag{5.212}$$

Taking also into account that $r_\vartheta(\vartheta) \equiv 0$ and defining the size parameter of the sphere as $x = k_1 a$, we derive from Eqs. (5.196)–(5.199)

$$J^{11}_{mnm'n'} \equiv 0, \quad J^{22}_{mnm'n'} \equiv 0, \quad \mathrm{Rg}J^{11}_{mnm'n'} \equiv 0, \quad \mathrm{Rg}J^{22}_{mnm'n'} \equiv 0, \tag{5.213}$$

$$J^{12}_{mnm'n'} = \delta_{mm'}\delta_{nn'}\frac{1}{k_1^2 m}\xi'_n(x)\psi_n(mx), \tag{5.214}$$

$$J^{21}_{mnm'n'} = -\delta_{mm'}\delta_{nn'}\frac{1}{k_1^2 m}\xi_n(x)\psi'_n(mx), \tag{5.215}$$

$$\mathrm{Rg}J^{12}_{mnm'n'} = \delta_{mm'}\delta_{nn'}\frac{1}{k_1^2 m}\psi'_n(x)\psi_n(mx), \tag{5.216}$$

$$\mathrm{Rg}J^{21}_{mnm'n'} = -\delta_{mm'}\delta_{nn'}\frac{1}{k_1^2 m}\psi_n(x)\psi'_n(mx), \tag{5.217}$$

where

$$\xi_n(z) = z h_n^{(1)}(z), \qquad \psi_n(z) = z j_n(z), \tag{5.218}$$

and $m = k_2/k_1$ is the relative refractive index. Equations (5.180)–(5.183), (5.186)–(5.189), and (5.191) finally yield Eqs. (5.42)–(5.44), where the Lorenz–Mie coefficients a_n and b_n are given by

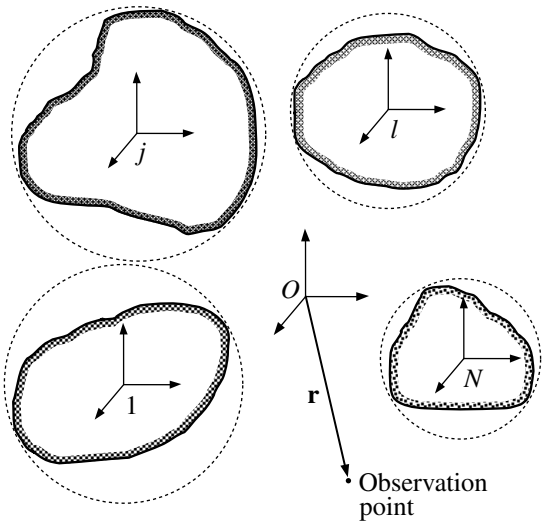

Figure 5.6. Local and common reference frames used to describe electromagnetic scattering by a cluster consisting of N arbitrarily shaped components.

$$a_n = \frac{m\psi_n(mx)\psi_n'(x) - \psi_n(x)\psi_n'(mx)}{m\psi_n(mx)\xi_n'(x) - \xi_n(x)\psi_n'(mx)}, \tag{5.219}$$

$$b_n = \frac{m\psi_n(x)\psi_n'(mx) - \psi_n(mx)\psi_n'(x)}{m\xi_n(x)\psi_n'(mx) - \psi_n(mx)\xi_n'(x)}. \tag{5.220}$$

Equations (5.219) and (5.220) are identical to Eqs. (4.56) and (4.57) of Bohren and Huffman (1983).

5.9 Aggregated and composite particles

Consider now the computation of the T matrix for a cluster consisting of N arbitrarily shaped and arbitrarily oriented components. We assume that the T matrices of all cluster components are known in their respective local coordinate systems with origins inside the components. We also assume that all these local coordinate systems have the same spatial orientation as the common reference frame of the cluster centered at O and that the smallest circumscribing spheres of the components centered at the origins of their respective local coordinate systems do not overlap (Fig. 5.6). The total electric field scattered by the cluster can be represented as a superposition of individual (partial) scattering contributions from each component:

$$\mathbf{E}^{\rm sca}(\mathbf{r}) = \sum_{j=1}^{N} \mathbf{E}_j^{\rm sca}(\mathbf{r}), \tag{5.221}$$

where $\mathbf{r}$ connects the origin of the common coordinate system and the observation point. Because of electromagnetic interactions between the components, the individual scattered fields are interdependent, and the total electric field exciting each component can be represented as a superposition of the external incident field $\mathbf{E}_0^{\rm inc}(\mathbf{r})$ and

the sum of the partial fields scattered by all other components:

$$\mathbf{E}_j^{\mathrm{inc}}(\mathbf{r}) = \mathbf{E}_0^{\mathrm{inc}}(\mathbf{r}) + \sum_{\substack{l=1 \\ l\neq j}}^{N} \mathbf{E}_l^{\mathrm{sca}}(\mathbf{r}), \qquad j = 1, ..., N. \tag{5.222}$$

To make use of the information contained in the *j*th component *T* matrix, we must expand the fields incident on and scattered by this component in vector spherical wave functions centered at the origin of the component's local coordinate system:

$$\begin{aligned}\mathbf{E}_j^{\mathrm{inc}}(\mathbf{r}) &= \sum_{nm} [a_{mn}^j \mathrm{Rg}\mathbf{M}_{mn}(k_1\mathbf{r}_j) + b_{mn}^j \mathrm{Rg}\mathbf{N}_{mn}(k_1\mathbf{r}_j)] \\ &= \sum_{nm} \left\{ \left(a_{mn}^{j0} + \sum_{l\neq j} a_{mn}^{jl} \right) \mathrm{Rg}\mathbf{M}_{mn}(k_1\mathbf{r}_j) \right. \\ &\quad \left. + \left(b_{mn}^{j0} + \sum_{l\neq j} b_{mn}^{jl} \right) \mathrm{Rg}\mathbf{N}_{mn}(k_1\mathbf{r}_j) \right\}, \qquad j = 1, ..., N, \end{aligned} \tag{5.223}$$

$$\mathbf{E}_j^{\mathrm{sca}}(\mathbf{r}) = \sum_{nm} [p_{mn}^j \mathbf{M}_{mn}(k_1\mathbf{r}_j) + q_{mn}^j \mathbf{N}_{mn}(k_1\mathbf{r}_j)], \qquad r_j > r_{j>}, \qquad j = 1, ..., N, \tag{5.224}$$

where $\mathbf{r}_j$ connects the origin of the *j*th local coordinate system and the observation point, $r_{j>}$ is the radius of the smallest circumscribing sphere of the *j*th component, the coefficients a_{mn}^{j0} and b_{mn}^{j0} describe the external incident field, and the expansion coefficients a_{mn}^{jl} and b_{mn}^{jl} describe the contribution of the *l*th component to the field illuminating the *j*th component:

$$\mathbf{E}_0^{\mathrm{inc}}(\mathbf{r}) = \sum_{nm} [a_{mn}^{j0} \mathrm{Rg}\mathbf{M}_{mn}(k_1\mathbf{r}_j) + b_{mn}^{j0} \mathrm{Rg}\mathbf{N}_{mn}(k_1\mathbf{r}_j)], \qquad j = 1, ..., N, \tag{5.225}$$

$$\mathbf{E}_l^{\mathrm{sca}}(\mathbf{r}) = \sum_{nm} [a_{mn}^{jl} \mathrm{Rg}\mathbf{M}_{mn}(k_1\mathbf{r}_j) + b_{mn}^{jl} \mathrm{Rg}\mathbf{N}_{mn}(k_1\mathbf{r}_j)], \qquad j, l = 1, ..., N, \quad l \neq j. \tag{5.226}$$

The expansion coefficients of the illuminating and scattered fields are related via the *j*th component *T* matrix $\mathbf{T}^j$:

$$\begin{bmatrix} \mathbf{p}^j \\ \mathbf{q}^j \end{bmatrix} = \mathbf{T}^j \left(\begin{bmatrix} \mathbf{a}^{j0} \\ \mathbf{b}^{j0} \end{bmatrix} + \sum_{l\neq j} \begin{bmatrix} \mathbf{a}^{jl} \\ \mathbf{b}^{jl} \end{bmatrix} \right), \qquad j = 1, ..., N. \tag{5.227}$$

The field scattered by the *l*th component can also be expanded in outgoing vector spherical wave functions centered at the origin of the *l*th local coordinate system:

$$\mathbf{E}_l^{\mathrm{sca}}(\mathbf{r}) = \sum_{\nu\mu} [p_{\mu\nu}^l \mathbf{M}_{\mu\nu}(k_1\mathbf{r}_l) + q_{\mu\nu}^l \mathbf{N}_{\mu\nu}(k_1\mathbf{r}_l)], \qquad r_l > r_{l>}, \qquad l = 1, ..., N, \qquad l \neq j, \tag{5.228}$$

where $\mathbf{r}_l$ connects the origin of the lth coordinate system and the observation point. Using the translation addition theorem (C.68), the vector spherical wave functions appearing in Eq. (5.228) can be expanded in regular vector spherical wave functions centered at the origin of the jth reference frame:

$$\begin{matrix}\mathbf{M}_{\mu\nu}\\ \mathbf{N}_{\mu\nu}\end{matrix}(k_1\mathbf{r}_l)=\sum_{nm}\left[\begin{matrix}A_{mn\mu\nu}\\ B_{mn\mu\nu}\end{matrix}(k_1\mathbf{r}_{lj})\mathrm{Rg}\mathbf{M}_{mn}(k_1\mathbf{r}_j)+\begin{matrix}B_{mn\mu\nu}\\ A_{mn\mu\nu}\end{matrix}(k_1\mathbf{r}_{lj})\mathrm{Rg}\mathbf{N}_{\mu\nu}(k_1\mathbf{r}_j)\right],$$
$$r_j<r_{lj}, \quad (5.229)$$

where the vector $\mathbf{r}_{lj}=\mathbf{r}_l-\mathbf{r}_j$ connects the origins of the lth and jth local coordinate systems and the translation coefficients $A_{mn\mu\nu}(k_1\mathbf{r}_{lj})$ and $B_{mn\mu\nu}(k_1\mathbf{r}_{lj})$ are given by Eqs. (C.69) and (C.70). Using Eqs. (5.226)–(5.229), we finally derive, in matrix notation,

$$\begin{bmatrix}\mathbf{p}^j\\ \mathbf{q}^j\end{bmatrix}=\mathbf{T}^j\left(\begin{bmatrix}\mathbf{a}^{j0}\\ \mathbf{b}^{j0}\end{bmatrix}+\sum_{l\neq j}\begin{bmatrix}\mathbf{A}(k_1\mathbf{r}_{lj}) & \mathbf{B}(k_1\mathbf{r}_{lj})\\ \mathbf{B}(k_1\mathbf{r}_{lj}) & \mathbf{A}(k_1\mathbf{r}_{lj})\end{bmatrix}\begin{bmatrix}\mathbf{p}^l\\ \mathbf{q}^l\end{bmatrix}\right), \qquad j=1,\ldots,N. \quad (5.230)$$

Since the expansion coefficients of the external plane electromagnetic wave a_{mn}^{j0} and b_{mn}^{j0} and the translation coefficients $A_{mn\mu\nu}(k_1\mathbf{r}_{lj})$ and $B_{mn\mu\nu}(k_1\mathbf{r}_{lj})$ can be computed via closed form analytical formulas, Eq. (5.230) can be considered as a system of linear algebraic equations which can be solved numerically and yields the expansion coefficients of the individual scattered fields p_{mn}^j and q_{mn}^j for each of the cluster components. When these coefficients are known, Eqs. (5.224) and (5.221) give the total field scattered by the cluster.

Equation (5.230) forms the basis of the T-matrix superposition method for aggregates. It becomes especially simple for a cluster consisting of spherical components since in this case the individual component T matrices are diagonal, with standard Lorenz–Mie coefficients standing along their main diagonals (Eqs. (5.42)–(5.44)). The resulting equation becomes identical to that derived using the so-called multi-sphere superposition formulation or multi-sphere separation of variables technique (Bruning and Lo 1971a, b; Borghese *et al.* 1979; and especially Fuller and Mackowski 2000 and references therein). In this regard, the latter can be considered as a particular case of the superposition T-matrix method. Numerical solutions of Eq. (5.230) for clusters of spheres have been obtained using different techniques (direct matrix inversion, the method of successive orders of scattering, the conjugate gradients method, the method of iterations, the recursive method) and have been extensively reported in the literature (Hamid *et al.* 1991; Quinten and Kreibig 1993; Fuller, 1994, 1995a; Xu 1995; Jin and Huang 1996a; Videen *et al.* 1998a; Quinten 1999). Jin and Huang (1996b) and Huang and Jin (1998) applied the superposition T-matrix formalism to clusters of spheroids. Fikioris and Uzunoglu (1979), Borghese *et al.* (1992, 1994), Skaropoulos *et al.* (1994), Fuller (1995b), Mackowski and Jones (1995), and Auger *et al.* (2001) have extended the superposition approach to the case of internal aggregation by solving the problem of light scattering by spherical particles with eccentric spherical inclusions, whereas Videen *et al.* (1995) con-

sidered the more general case of a sphere with an irregular inclusion. Of course, particles with a single inclusion can also be treated using the standard EBCM for multilayered scatterers (Peterson and Ström 1974).

Inversion of Eq. (5.230) gives

$$\begin{bmatrix} \mathbf{p}^j \\ \mathbf{q}^j \end{bmatrix} = \sum_{l=1}^{N} \mathbf{T}^{jl} \begin{bmatrix} \mathbf{a}^{l0} \\ \mathbf{b}^{l0} \end{bmatrix}, \qquad j = 1, ..., N \tag{5.231}$$

(Mackowski 1994), where the matrix $\mathbf{T}^{jl}$ transforms the coefficients of the incident-field expansion centered at the lth origin into the jth-origin-centered expansion coefficients of the partial field scattered by the jth component. The calculation of the $\mathbf{T}^{jl}$ matrices entails the numerical inversion of a large matrix and can be a time-consuming process. However, these matrices are independent of the incident field and depend only on the cluster configuration and the shapes and orientations of the components. Therefore, they need be computed only once and then can be used in computations for any direction and polarization state of the incident field.

Furthermore, in the far-field region the scattered-field expansions from the individual components can be transformed into a single expansion centered at the origin O of the common reference frame (Fig. 5.6). This single origin can represent the average of the component particle positions but in general can be arbitrary. The first step is to expand the incident and total scattered fields in vector spherical wave functions centered at O, according to Eqs. (5.2) and (5.3). We again employ the translation addition theorem given by Eq. (C.66),

$$\mathrm{Rg}\begin{matrix}\mathbf{M}_{mn} \\ \mathbf{N}_{mn}\end{matrix}(k_1\mathbf{r}) = \sum_{\nu\mu}\left[\mathrm{Rg}\begin{matrix}A_{\mu\nu mn} \\ B_{\mu\nu mn}\end{matrix}(k_1\mathbf{r}_{Ol})\mathrm{Rg}\mathbf{M}_{\mu\nu}(k_1\mathbf{r}_l) + \mathrm{Rg}\begin{matrix}B_{\mu\nu mn} \\ A_{\mu\nu mn}\end{matrix}(k_1\mathbf{r}_{Ol})\mathrm{Rg}\mathbf{N}_{\mu\nu}(k_1\mathbf{r}_l)\right], \tag{5.232}$$

and by the reciprocal formula (C.67),

$$\begin{aligned}\begin{matrix}\mathbf{M}_{mn} \\ \mathbf{N}_{mn}\end{matrix}(k_1\mathbf{r}_j) = \sum_{\nu\mu}\Bigg[& \mathrm{Rg}\begin{matrix}A_{\mu\nu mn} \\ B_{\mu\nu mn}\end{matrix}(k_1\mathbf{r}_{jO})\mathbf{M}_{\mu\nu}(k_1\mathbf{r}) \\ & + \mathrm{Rg}\begin{matrix}B_{\mu\nu mn} \\ A_{\mu\nu mn}\end{matrix}(k_1\mathbf{r}_{jO})\mathbf{N}_{\mu\nu}(k_1\mathbf{r})\Bigg], \qquad r > r_{jO},\end{aligned} \tag{5.233}$$

where $\mathbf{r}_{Ol} = \mathbf{r} - \mathbf{r}_l$ and $\mathbf{r}_{jO} = \mathbf{r}_j - \mathbf{r}$. We then easily derive

$$\begin{bmatrix} \mathbf{a}^{l0} \\ \mathbf{b}^{l0} \end{bmatrix} = \begin{bmatrix} \mathrm{Rg}\mathbf{A}(k_1\mathbf{r}_{Ol}) & \mathrm{Rg}\mathbf{B}(k_1\mathbf{r}_{Ol}) \\ \mathrm{Rg}\mathbf{B}(k_1\mathbf{r}_{Ol}) & \mathrm{Rg}\mathbf{A}(k_1\mathbf{r}_{Ol}) \end{bmatrix} \begin{bmatrix} \mathbf{a} \\ \mathbf{b} \end{bmatrix}, \qquad l = 1, ..., N, \tag{5.234}$$

$$\begin{bmatrix} \mathbf{p} \\ \mathbf{q} \end{bmatrix} = \sum_{j=1}^{N} \begin{bmatrix} \mathrm{Rg}\mathbf{A}(k_1\mathbf{r}_{jO}) & \mathrm{Rg}\mathbf{B}(k_1\mathbf{r}_{jO}) \\ \mathrm{Rg}\mathbf{B}(k_1\mathbf{r}_{jO}) & \mathrm{Rg}\mathbf{A}(k_1\mathbf{r}_{jO}) \end{bmatrix} \begin{bmatrix} \mathbf{p}^j \\ \mathbf{q}^j \end{bmatrix}. \tag{5.235}$$

Finally, using Eqs. (5.231), (5.234), and (5.235) we obtain Eq. (5.8), in which the cluster

T matrix is given by

$$\mathbf{T} = \sum_{j,l=1}^{N} \begin{bmatrix} \mathrm{Rg}\mathbf{A}(k_1\mathbf{r}_{jO}) & \mathrm{Rg}\mathbf{B}(k_1\mathbf{r}_{jO}) \\ \mathrm{Rg}\mathbf{B}(k_1\mathbf{r}_{jO}) & \mathrm{Rg}\mathbf{A}(k_1\mathbf{r}_{jO}) \end{bmatrix} \mathbf{T}^{jl} \begin{bmatrix} \mathrm{Rg}\mathbf{A}(k_1\mathbf{r}_{Ol}) & \mathrm{Rg}\mathbf{B}(k_1\mathbf{r}_{Ol}) \\ \mathrm{Rg}\mathbf{B}(k_1\mathbf{r}_{Ol}) & \mathrm{Rg}\mathbf{A}(k_1\mathbf{r}_{Ol}) \end{bmatrix} \quad (5.236)$$

(Peterson and Ström 1973; Mackowski 1994). This cluster T matrix can be used in Eqs. (5.11)–(5.14) to compute the amplitude matrix for a fixed cluster orientation and as input to the analytical procedures for averaging scattering characteristics over cluster orientations (Mishchenko and Mackowski 1994; Mackowski and Mishchenko 1996).

In agreement with Eqs. (5.36) and (5.37), the T matrix becomes much simpler when the cluster is a rotationally symmetric scatterer in the form of a linear chain of spheres and when the z-axis of the common reference frame is directed along the line connecting the centers of the component spheres (Mishchenko and Mackowski 1994). In general, one may need to combine Eq. (5.236) with the rotation transformation rule (5.29) in order to compute efficiently the T matrix for a cluster consisting of arbitrarily oriented and arbitrarily positioned nonspherical components (Jin and Huang 1996b).

Wang and Chew (1993) developed a recursive T-matrix algorithm, which computes the T matrix for a cluster consisting of n components by using the T matrix of the newly added nth component and the T matrix of the cluster consisting of the previous $n-1$ components. The apparent advantage of this technique is that it reduces computation of the T matrix for a cluster consisting of N components into a recursive sequence of $N-1$ two-component calculations. However, for reasons alluded to previously (Section 5.1), the smallest circumscribing sphere of each newly added component must always reside outside a sphere enclosing the cluster built at the previous recursion step. This constraint appears to limit the recursive algorithm to relatively simple and sparse clusters, for example, linear chains of spheres.

5.10 Lorenz–Mie code for homogeneous polydisperse spheres

The FORTRAN code for computing the scattering characteristics of an ensemble of polydisperse, homogeneous spherical particles is based on the Lorenz–Mie theory and is available on the World Wide Web at http://www.giss.nasa.gov/~crmim. This section discusses practical aspects of Lorenz–Mie calculations, describes the input and output parameters of the code, and provides an illustrative example.

5.10.1 Practical considerations

The numerical computation of the Lorenz–Mie coefficients a_n and b_n and the angular functions π_n and τ_n appearing in Eqs. (5.149) and (5.151) is considered in detail in many publications (e.g., Wiscombe 1980; Bohren and Huffman 1983; de Rooij and van der Stap 1984, and references therein) and will not be specifically discussed here.

In practical computer calculations, the infinite series of Eqs. (5.149) and (5.151) are truncated to a finite size $n_{\max}$ that depends on the size parameter $x = k_1 r$, where r is the particle radius. A simple empirical criterion for choosing $n_{\max}$ adopted in our code is

$$n_{\max}(x) = x + 4.05x^{1/3} + 8 \tag{5.237}$$

and is somewhat more conservative (i.e., it takes more terms than may be necessary) than that proposed by Wiscombe (1980).

The basic far-field optical characteristics of a homogeneous spherical particle are the extinction cross section C_{ext}, the scattering cross section C_{sca}, and the expansion coefficients α_p^s (p = 1, 2, 3, 4) and β_p^s (p = 1, 2) appearing in Eqs. (4.75)–(4.80). All these quantities can be directly expressed in terms of the Lorenz–Mie coefficients a_n and b_n (Section 5.7) and must be averaged over an appropriate normalized distribution of sphere radii $n(r)$ (Section 3.2) in order to obtain the scattering characteristics of a particle ensemble. All other cross sections, the single-scattering albedo, the efficiency factors, the asymmetry parameter, and the elements of the normalized scattering matrix for an arbitrary set of scattering angles are then found from Eqs. (4.43)–(4.46), (4.75)–(4.80), and (4.92). The Wigner d-functions entering Eqs. (4.75)–(4.80) are computed using the recurrence relation (B.22) and the initial conditions (B.23) and (B.24).

The computation of the ensemble-averaged extinction and scattering cross sections per particle is straightforward:

$$\langle C_{\text{ext}} \rangle = \int_{r_{\min}}^{r_{\max}} \mathrm{d}r\, n(r) C_{\text{ext}}(r) \approx \sum_{i=1}^{N_r} u_i n(r_i) C_{\text{ext}}(r_i), \tag{5.238}$$

$$\langle C_{\text{sca}} \rangle = \int_{r_{\min}}^{r_{\max}} \mathrm{d}r\, n(r) C_{\text{sca}}(r) \approx \sum_{i=1}^{N_r} u_i n(r_i) C_{\text{sca}}(r_i), \tag{5.239}$$

where r_i and u_i are the division points and weights, respectively, of a quadrature formula on the interval $[r_{\min}, r_{\max}]$. The ensemble-averaged expansion coefficients can be computed similarly using Eqs. (5.160)–(5.162) and (4.109)–(4.114). However, the necessity of keeping in computer memory large arrays containing the products of Lorenz–Mie coefficients with different indices appearing in Eqs. (5.160)–(5.162) imposes a limit on the maximum size parameter $x_{\max} = k_1 r_{\max}$ that can be handled by a given computer. Therefore, instead of using Eqs. (5.160)–(5.162), we compute the ensemble-averaged expansion coefficients by evaluating numerically the angular integrals in Eqs. (4.81)–(4.86) (de Rooij and van der Stap 1984). For example,

$$\begin{aligned} \alpha_1^s &= (s+\tfrac{1}{2}) \int_{-1}^{+1} \mathrm{d}(\cos\Theta) a_1(\Theta) d_{00}^s(\Theta) \\ &\approx (s+\tfrac{1}{2}) \sum_{j=1}^{N_\Theta} w_j a_1(\arccos\mu_j) d_{00}^s(\arccos\mu_j), \end{aligned} \tag{5.240}$$

where μ_j and w_j are the division points and weights of a Gaussian quadrature formula on the interval $[-1, +1]$,

$$a_1(\Theta) = \frac{1}{\langle C_{\rm sca} \rangle} \int_{r_{\rm min}}^{r_{\rm max}} {\rm d}r\, n(r) C_{\rm sca}(r) a_1(r; \Theta)$$
$$\approx \frac{1}{\langle C_{\rm sca} \rangle} \sum_{i=1}^{N_r} u_i n(r_i) C_{\rm sca}(r_i) a_1(r_i; \Theta) \tag{5.241}$$

is the ensemble-averaged (1,1)-element of the normalized Stokes scattering matrix (cf. Eq. (4.74)), and $a_1(r; \Theta)$ is given by Eq. (5.152). Other expansion coefficients are computed similarly. This numerical procedure involves computation of the elements of the normalized Stokes scattering matrix for N_Θ scattering angles and is slower than the analytical procedure based on Eqs. (5.160)–(5.162) and (4.109)–(4.114) by a factor of 2 (de Rooij and van der Stap 1984). However, the numerical procedure is applicable to significantly larger size parameters than the analytical method, assuming that the size of the computer memory is the same in both cases. Given the high speed of modern computers and hence the relatively low cost of the Lorenz–Mie computations, the advantages of the numerical approach seem to outweigh its disadvantages. de Rooij and van der Stap (1984) showed that a good *a priori* estimate for the number of quadrature division points in Eq. (5.240) is $N_\Theta = 2n_{\rm max}(x_{\rm max})$. It is more difficult to give an *a priori* estimate of the number N_r of quadrature division points in Eqs. (5.238), (5.239), and (5.241). In practice, this number should be increased in finite steps until all scattering characteristics of interest converge within a given accuracy.

It is often convenient to approximate natural size distributions using simple analytical distribution functions. The Lorenz–Mie code allows one to choose from the following set of six analytical size distributions:

- the modified gamma distribution

$$n(r) = {\rm constant} \times r^\alpha \exp\left(-\frac{\alpha r^\gamma}{\gamma r_c^\gamma}\right); \tag{5.242}$$

- the log normal distribution

$$n(r) = {\rm constant} \times r^{-1} \exp\left[-\frac{(\ln r - \ln r_g)^2}{2 \ln^2 \sigma_g}\right]; \tag{5.243}$$

- the power law distribution

$$n(r) = \begin{cases} {\rm constant} \times r^{-3}, & r_1 \le r \le r_2, \\ 0, & {\rm otherwise}; \end{cases} \tag{5.244}$$

- the gamma distribution

$$n(r) = {\rm constant} \times r^{(1-3b)/b} \exp\left(-\frac{r}{ab}\right), \quad b \in (0, 0.5); \tag{5.245}$$

- the modified power law distribution

$$n(r)=\begin{cases}\text{constant}, & 0\le r\le r_1,\\ \text{constant}\times(r/r_1)^{\alpha}, & r_1\le r\le r_2,\\ 0, & r_2<r;\end{cases} \tag{5.246}$$

- the modified bimodal log normal distribution

$$n(r)=\text{constant}\times r^{-4}\left\{\exp\left[-\frac{(\ln r-\ln r_{g1})^2}{2\ln^2\sigma_{g1}}\right]+\gamma\exp\left[-\frac{(\ln r-\ln r_{g2})^2}{2\ln^2\sigma_{g2}}\right]\right\}. \tag{5.247}$$

The constant for each size distribution is chosen such that the size distribution satisfies the standard normalization of Eq. (3.26).

Implicitly, particle radii in the modified gamma, log normal, gamma, and modified bimodal log normal distributions extend to infinity. However, a finite $r_{\max}$ must be chosen in actual computer calculations. There are two different practical interpretations of a truncated size distribution. The first assumes that $r_{\max}$ is increased iteratively until the scattering and absorption characteristics of the size distribution converge within a prescribed numerical accuracy. In this case the converged truncated size distribution is numerically equivalent to the distribution with $r_{\max}=\infty$. In the second interpretation, the truncated distribution with a prescribed $r_{\max}$ is considered as a specific size distribution with scattering and absorption characteristics distinctly different from those for the distribution with $r_{\max}=\infty$. Similar considerations apply to the parameter $r_{\min}$, whose implicit value for the modified gamma, log normal, gamma, and modified bimodal log normal distributions is zero, but in practice can be any number smaller than $r_{\max}$. In this book, we adopt the first interpretation of a truncated size distribution, unless explicitly indicated otherwise. The actual numerical integration of scattering characteristics over a size distribution is achieved by subdividing the entire interval $[r_{\min}, r_{\max}]$ of particle radii into a number of equal subintervals and applying a Gaussian quadrature formula with a fixed number of division points to each subinterval.

We will see in later chapters that two important characteristics of a size distribution are the effective radius r_{eff} and effective variance v_{eff}, defined by

$$r_{\text{eff}}=\frac{1}{\langle G\rangle}\int_{r_{\min}}^{r_{\max}}\mathrm{d}r\,n(r)r\pi r^2, \tag{5.248}$$

$$v_{\text{eff}}=\frac{1}{\langle G\rangle r_{\text{eff}}^2}\int_{r_{\min}}^{r_{\max}}\mathrm{d}r\,n(r)(r-r_{\text{eff}})^2\pi r^2, \tag{5.249}$$

where

$$\langle G\rangle=\int_{r_{\min}}^{r_{\max}}\mathrm{d}r\,n(r)\pi r^2 \tag{5.250}$$

is the average area of the geometric projection per particle (Hansen and Travis 1974).

r_{eff} is simply the projected-area-weighted mean radius, whereas the dimensionless effective variance provides a measure of the width of the size distribution. It is straightforward to show that for the gamma distribution with $r_{\min} = 0$ and $r_{\max} = \infty$, a and b coincide with r_{eff} and v_{eff}, respectively. For the other size distributions with specific values of $r_{\min}$ and $r_{\max}$ the effective radius and effective variance must be determined either analytically or numerically.

5.10.2 Input parameters of the Lorenz–Mie code

NDISTR, AA, BB, GAM:

The parameter NDISTR specifies the type of the particle size distribution. For the modified gamma distribution (5.242), $\text{NDISTR} = 1$, $\text{AA} = \alpha$, $\text{BB} = r_c$, and $\text{GAM} = \gamma$. For the log normal distribution (5.243), $\text{NDISTR} = 2$, $\text{AA} = r_g$, $\text{BB} = \ln^2\sigma_g$, and GAM is ignored. For the power law distribution (5.244), $\text{NDISTR} = 3$, $\text{AA} = r_{\text{eff}}$, $\text{BB} = v_{\text{eff}}$, and GAM is ignored. In this case the parameters R1 and R2 (see below) are calculated from Eqs. (5.244) and (5.248)–(5.250) for given r_{eff} and v_{eff}. For the gamma distribution (5.245), $\text{NDISTR} = 4$, $\text{AA} = a$, $\text{BB} = b$, and GAM is ignored. For the modified power law distribution (5.246), $\text{NDISTR} = 5$, $\text{BB} = \alpha$, and AA and GAM are ignored. Finally, for the modified bimodal log normal distribution (5.247), $\text{NDISTR} = 6$, $\text{AA1} = r_{g1}$, $\text{BB1} = \ln^2\sigma_{g1}$, $\text{AA2} = r_{g2}$, $\text{BB2} = \ln^2\sigma_{g2}$, and $\text{GAM} = \gamma$.

R1 and R2:

$\text{R1} = r_{\min}$ and $\text{R2} = r_{\max}$ are the minimal and maximal radii in the size distribution for NDISTR = 1–4 and 6. R1 and R2 are calculated automatically for the power law distribution $\text{NDISTR} = 3$ with given r_{eff} and v_{eff}, but they must be specified explicitly for other distributions. For the modified power law distribution NDISTR=5, $r_{\min} = 0$, $\text{R1} = r_1$, and $\text{R2} = r_2 = r_{\max}$.

LAM:

$\text{LAM} = \lambda_1$ is the wavelength of the incident light in the surrounding medium.

MRR and MRI:

$\text{MRR} = \text{Re}\, m$ and $\text{MRI} = \text{Im}\, m$ are the real and imaginary parts of the relative refractive index. MRI must be non-negative.

N, NP, and NK:

N is the number of equal integration subintervals on the interval [R1, R2]. NP is the number of equal integration subintervals on the interval [0, R1] for the modified power law distribution. NK is the number of Gaussian division points on each of the

integration subintervals. In other words, $N_r = \mathrm{N} * \mathrm{NK}$ for $\mathrm{NDISTR} = 1, 2, 3, 4, 6$ and $N_r = (\mathrm{N} + \mathrm{NP}) * \mathrm{NK}$ for $\mathrm{NDISTR} = 5$ in Eqs. (5.238), (5.239), and (5.241).

NPNA:
NPNA is the number of scattering angles at which the normalized scattering matrix is computed. This parameter appears in the PARAMETER statement in the subroutine MATR. The corresponding scattering angles are given by 180*(I–1)/(NPNA–1) (degrees), where I numbers the angles. This way of choosing scattering angles can be changed in the subroutine MATR by properly modifying the following lines,

```
N = NPNA
DN = 1D0/DFLOAT(N–1)
DA = DACOS(–1D0)*DN
DB = 180D0*DN
TB = –DB
TAA = –DA
DO 500 I1 = 1, N
    TAA = TAA+DA
    TB = TB+DB
```

and leaving the rest of the subroutine intact. This flexibility is provided by the fact that after the expansion coefficients α_p^s (p = 1, 2, 3, 4) and β_p^s (p = 1, 2) are computed by the subroutine SPHER, the scattering matrix can readily be computed for any set of scattering angles (cf. Section 4.11).

DDELT:
DDELT is the desired numerical accuracy of computation of the elements of the normalized scattering matrix.

5.10.3 Output information

R1 and R2:
For the power law size distribution $\mathrm{NDISTR} = 3$, $\mathrm{R1} = r_1$ and $\mathrm{R2} = r_2$ are the minimal and maximal radii, respectively, calculated for the input values of r_{eff} and v_{eff}.

REFF and VEFF:
$\mathrm{REFF} = r_{\mathrm{eff}}$ and $\mathrm{VEFF} = v_{\mathrm{eff}}$ are the effective radius and the effective variance of the size distribution, respectively.

CEXT and CSCA:
$\mathrm{CEXT} = \langle C_{\mathrm{ext}} \rangle$ and $\mathrm{CSCA} = \langle C_{\mathrm{sca}} \rangle$ are the ensemble-averaged extinction and scattering cross sections per particle, respectively.

< COS > and ALBEDO:
$< \mathrm{COS} > = \langle \cos\Theta \rangle$ and $\mathrm{ALBEDO} = \varpi$ are the ensemble-averaged asymmetry parameter and single-scattering albedo, respectively.

< G >:
$< \mathrm{G} > = \langle G \rangle$ is the average projected area per particle defined by Eq. (5.250).

< V >:
$< \mathrm{V} > = \langle V \rangle$ is the average volume per particle defined by

$$\langle V \rangle = \int_{r_{\min}}^{r_{\max}} \mathrm{d}r\, n(r) \tfrac{4}{3} \pi r^3. \tag{5.251}$$

< R >:
$< \mathrm{R} > = \langle r \rangle$ is the average radius defined by

$$\langle r \rangle = \int_{r_{\min}}^{r_{\max}} \mathrm{d}r\, n(r) r. \tag{5.252}$$

Rvw:
$\mathrm{Rvw} = r_{\mathrm{vw}}$ is the volume-weighted average radius defined by

$$r_{\mathrm{vw}} = \frac{1}{\langle V \rangle} \int_{r_{\min}}^{r_{\max}} \mathrm{d}r\, n(r) r \tfrac{4}{3} \pi r^3. \tag{5.253}$$

ALPHA1, …, BETA2:
$\mathrm{ALPHA1(S)} = \alpha_1^s$, $\mathrm{ALPHA2(S)} = \alpha_2^s$, $\mathrm{ALPHA3(S)} = \alpha_3^s$, $\mathrm{ALPHA4(S)} = \alpha_4^s$, $\mathrm{BETA1(S)} = \beta_1^s$, and $\mathrm{BETA2(S)} = \beta_2^s$ are the expansion coefficients appearing in Eqs. (4.75)–(4.80).

F11, F33, F12, and F34:
$\mathrm{F11} = a_1$, $\mathrm{F33} = a_3$, $\mathrm{F12} = b_1$, and $\mathrm{F34} = b_2$, are the elements of the normalized Lorenz–Mie scattering matrix of Eq. (4.65).

5.10.4 Additional comments and illustrative example

It is important to remember that all input parameters having the dimension of length (i.e., r_c, r_g, r_{eff}, a, r_1, r_2, r_{g1}, r_{g2}, λ_1) must be specified in the same units. If these parameters are specified, for example, in micrometers then output parameters having the dimension of length, area, and volume are given in micrometers, square micrometers, and cubical micrometers, respectively. For given size distribution parameters, the parameters N, NP, and/or NK should be increased until convergent results are obtained for the extinction and scattering cross sections and, especially, the

expansion coefficients and the elements of the normalized scattering matrix.

To calculate the scattering characteristics of a monodisperse particle having a radius r, one may use the following options:

```
AA = r
BB = 1D–1
NDISTR = 4
NK = 1
N = 1
R1 = AA*0.9999999 D0
R2 = AA*1.0000001 D0
```

The code has been extensively tested versus a program based on Eqs. (5.160)–(5.162) and (4.109)–(4.114) as well as versus the codes independently written by Hansen and Travis (1974) and de Rooij and van der Stap (1984). Excellent agreement has been found in all cases considered. In particular, we were able to reproduce the numbers in Tables 2–4 of de Rooij and van der Stap to within ± 1 in the last decimals given.

To illustrate the performance of the Lorenz–Mie code, Tables 5.1 and 5.2 list the expansion coefficients and the elements of the normalized scattering matrix for the power law distribution (5.244) with $r_{\rm eff} = 0.6\,\mu{\rm m}$ and $v_{\rm eff} = 0.2$. The wavelength in the surrounding medium is $\lambda_1 = 0.63\,\mu{\rm m}$ and the relative refractive index is $m = 1.53 + {\rm i}0.008$. Other output parameters are as follows: $\langle C_{\rm ext}\rangle = 1.92604\,\mu{\rm m}^2$, $\langle C_{\rm sca}\rangle = 1.78033\,\mu{\rm m}^2$, $\varpi = 0.924351$, $\langle\cos\Theta\rangle = 0.703689$, $r_1 = 0.245830\,\mu{\rm m}$, $r_2 = 1.19417\,\mu{\rm m}$, $\langle G\rangle = 0.626712\,\mu{\rm m}^2$, $\langle V\rangle = 0.501369\,\mu{\rm m}^3$, $r_{\rm vw} = 0.720000\,\mu{\rm m}$, and $\langle r\rangle = 0.407726\,\mu{\rm m}$. Table 5.1 demonstrates the typical behavior of the expansion coefficients with increasing s: on average, they first grow in absolute value and then decay to values below a reasonable numerical threshold. The larger the particles relative to the wavelength, the larger the maximal absolute value of the expansion coefficients and the slower their decay (cf. Fig. 5.7).

5.11 *T*-matrix code for polydisperse, randomly oriented, homogeneous, rotationally symmetric particles

The FORTRAN code for computing the far-field scattering and absorption characteristics of a polydisperse ensemble of randomly oriented, homogeneous, rotationally symmetric particles is based on the analytical orientation-averaging method described in Sections 5.4–5.6 and the extended boundary condition method described in Section 5.8; it is available on the World Wide Web at http://www.giss.nasa.gov/~crmim. This section discusses numerical and practical aspects of *T*-matrix and EBCM computations, lists the input and output parameters of the code, and describes several illustrative examples.

Table 5.1. Expansion coefficients for a power law size distribution of homogeneous spherical particles (see text)

s	α_1^s	α_2^s	α_3^s	α_4^s	β_1^s	β_2^s
0	1.00000	0.00000	0.00000	0.89795	0.00000	0.00000
1	2.11107	0.00000	0.00000	2.17321	0.00000	0.00000
2	2.80371	3.94496	3.70286	2.68232	– 0.11397	0.04016
3	2.75088	3.26632	3.32478	2.86830	– 0.04919	– 0.13012
4	2.78642	3.29211	3.08787	2.67642	– 0.11611	– 0.09967
5	2.51483	2.71962	2.76717	2.62148	0.02311	– 0.23388
6	2.37043	2.68850	2.53377	2.29258	– 0.08347	– 0.14514
7	2.12491	2.19572	2.22264	2.21115	0.03711	– 0.22087
8	1.94158	2.17567	2.05467	1.88603	– 0.07778	– 0.16015
9	1.72589	1.74352	1.76215	1.80127	0.02696	– 0.18509
10	1.54525	1.72822	1.62493	1.50006	– 0.07066	– 0.16683
11	1.33856	1.33822	1.35592	1.40884	0.01412	– 0.14733
12	1.18264	1.32442	1.23019	1.14003	– 0.06023	– 0.16558
13	0.98046	0.97712	0.99647	1.04645	0.00414	– 0.11420
14	0.85744	0.96367	0.87607	0.81429	– 0.04833	– 0.15555
15	0.66452	0.66350	0.68361	0.72364	– 0.00131	– 0.08708
16	0.57301	0.64891	0.56980	0.53010	– 0.03585	– 0.13776
17	0.39838	0.40032	0.41870	0.44708	– 0.00135	– 0.06506
18	0.33469	0.38531	0.31822	0.29493	– 0.02181	– 0.11245
19	0.19091	0.19427	0.20871	0.22691	0.00293	– 0.04528
20	0.15885	0.18833	0.13387	0.12268	– 0.00442	– 0.07658
21	0.06616	0.06753	0.07753	0.08893	0.00548	– 0.01461
22	0.06678	0.08074	0.04492	0.04153	– 0.00413	– 0.03682
23	0.02026	0.02103	0.02698	0.03304	– 0.00277	– 0.00397
24	0.02708	0.03337	0.01144	0.01048	– 0.00297	– 0.01952
25	0.00370	0.00393	0.00553	0.00797	0.00015	– 0.00132
26	0.00906	0.01105	0.00090	0.00065	0.00137	– 0.00486
27	– 0.00088	– 0.00088	– 0.00001	0.00051	– 0.00092	0.00187
28	0.00188	0.00215	– 0.00046	– 0.00040	– 0.00097	– 0.00118
29	0.00002	0.00003	0.00006	0.00005	0.00013	– 0.00006
30	0.00001	0.00002	0.00001	0.00001	0.00001	– 0.00001
31	0.00000	0.00000	0.00000	0.00000	0.00000	0.00000

Table 5.2. Elements of the normalized Stokes scattering matrix for a power law size distribution of homogeneous spherical particles (see text)

Θ (deg)	$a_1(\Theta)$	$a_3(\Theta)$	$b_1(\Theta)$	$b_2(\Theta)$
0	30.5485	30.5485	0.00000	0.00000
10	17.5868	17.5325	0.11636	0.74705
20	6.32160	6.19549	0.10722	0.51234
30	3.17426	3.07387	0.08634	0.28530
40	1.68979	1.59809	0.10664	0.12816
50	0.98175	0.89795	0.10301	0.04929
60	0.60514	0.52727	0.09051	– 0.00844
70	0.39723	0.32358	0.07470	– 0.02873
80	0.28182	0.21282	0.05192	– 0.03907
90	0.21054	0.14274	0.03917	– 0.04148
100	0.16867	0.10289	0.02996	– 0.03777
110	0.14492	0.07875	0.02723	– 0.03832
120	0.13501	0.06582	0.03002	– 0.04153
130	0.14110	0.06037	0.04039	– 0.05465
140	0.17064	0.05901	0.06230	– 0.07784
150	0.23806	0.05207	0.10700	– 0.11341
160	0.34927	0.00673	0.17620	– 0.12169
170	0.38436	– 0.27524	0.16140	0.10428
180	0.76915	– 0.76915	0.00000	0.00000

5.11.1 Computation of the *T* matrix for an individual particle

Equations (5.196)–(5.199) and the respective formulas for $\mathrm{Rg}J^{kl}_{mnm'n'}$ contain several angular and radial functions that must be computed numerically for argument values corresponding to the quadrature division points in Eq. (5.202). The functions $r(\vartheta)$ and $r_\vartheta(\vartheta)$ are computed analytically for a given particle shape. An accurate and numerically stable way of computing the Wigner *d*-functions $d^n_{0m}(\vartheta)$ and the functions $\pi_{mn}(\vartheta)$ and $\tau_{mn}(\vartheta)$ defined by Eqs. (5.16) and (5.17) is provided by the recurrence relations (B.22) and (B.26) supplemented by the initial values given by Eqs. (B.23) and (B.24). The symmetry relations (5.205)–(5.207) reduce the computational effort by a factor of 2.

The spherical Bessel functions of the first kind, $j_n(z)$ (where z is equal to $k_1 r$ or $k_2 r$ and is, in general, complex), satisfy the recurrence relation (Abramowitz and Stegun 1964):

$$j_{n+1}(z) = \frac{2n+1}{z} j_n(z) - j_{n-1}(z). \tag{5.254}$$

Since the upward recurrence relation for $j_n(z)$ is unstable, we define

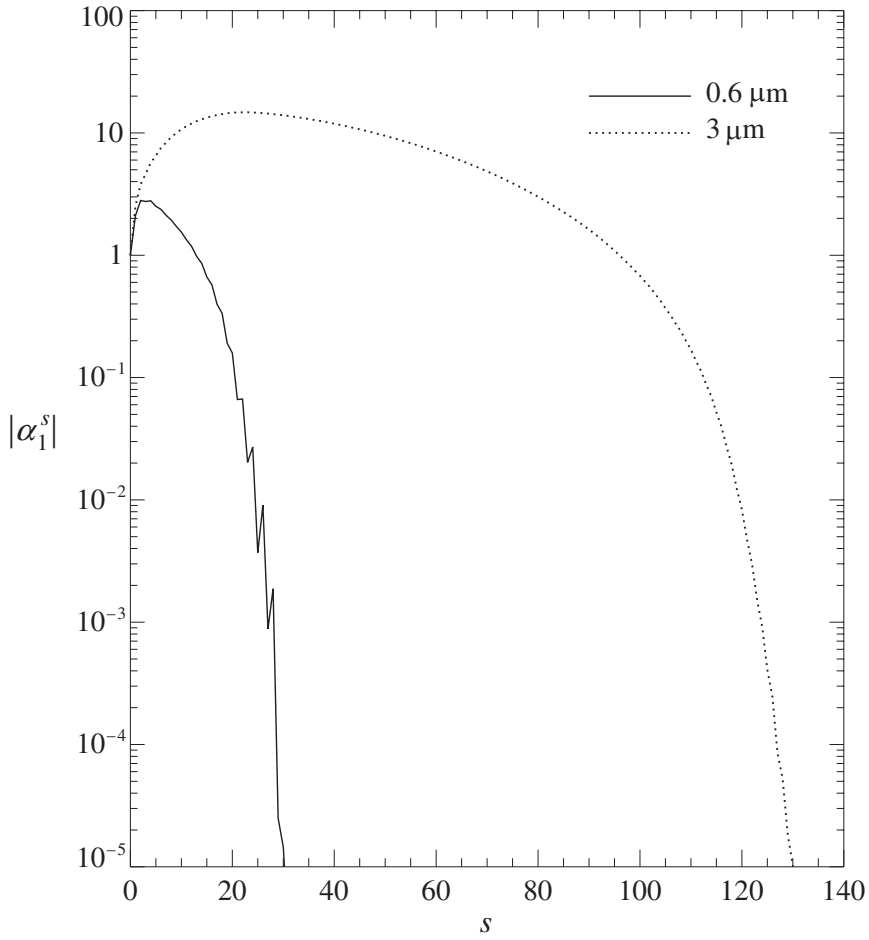

Figure 5.7. Absolute values of the coefficients α_1^s appearing in the Legendre expansion of the phase function for power law distributions of spherical particles with $r_{\text{eff}} = 0.6\,\mu\text{m}$ (solid line) and $3\,\mu\text{m}$ (dotted line), $v_{\text{eff}} = 0.2$, and $m = 1.53 + i0.008$. The wavelength in the surrounding medium is $\lambda_1 = 0.63\,\mu\text{m}$.

$$r_n(z) = \frac{j_n(z)}{j_{n-1}(z)}, \tag{5.255}$$

leading to the downward recurrence relation

$$r_n(z) = \left[\frac{2n+1}{z} - r_{n+1}(z)\right]^{-1}. \tag{5.256}$$

For $n \gg |z|$, we have

$$r_n(z) \underset{n\gg|z|}{\approx} \frac{z}{2n+1}. \tag{5.257}$$

If $n_{\max}$ is the largest n-value (cf. subsection 5.8.4), we start the downward recursion of Eq. (5.256) at $n = n_{\max} + n'$, where n' depends on the maximal particle dimension

relative to the wavelength (and, for $z = k_2 r$, the relative refractive index) and is chosen such that by the time n has been reduced to $n_{\max}$, the error in $r_{n_{\max}}(z)$ caused by using the approximate asymptotic formula (5.257) becomes negligibly small. We then compute $j_n(z)$, using the upward recursion

$$j_n(z) = r_n(z) j_{n-1}(z) \tag{5.258}$$

and starting at

$$j_0(z) = r_0(z) \frac{\cos z}{z}. \tag{5.259}$$

We also use the recurrence relation

$$\frac{1}{z}\frac{\mathrm{d}}{\mathrm{d}z}[z j_n(z)] = j_{n-1}(z) - \frac{n}{z} j_n(z), \tag{5.260}$$

which follows from Eq. (5.254) and the formula (Abramowitz and Stegun 1964)

$$(2n+1)\frac{\mathrm{d}}{\mathrm{d}z} j_n(z) = n j_{n-1}(z) - (n+1) j_{n+1}(z). \tag{5.261}$$

To compute the Hankel functions of the first kind, defined by Eq. (C.1), and their derivative we first find the spherical Bessel functions of the first kind, as described above, and then compute the spherical Bessel functions of the second kind using the numerically stable upward recurrence relation

$$y_{n+1}(z) = \frac{2n+1}{z} y_n(z) - y_{n-1}(z) \tag{5.262}$$

and the initial values

$$y_{-1}(z) = \frac{\sin z}{z}, \qquad y_0(z) = -\frac{\cos z}{z}, \tag{5.263}$$

where $z = k_1 r$ is real. Finally, we use the recurrence formula

$$\frac{1}{z}\frac{\mathrm{d}}{\mathrm{d}z}[z y_n(z)] = y_{n-1}(z) - \frac{n}{z} y_n(z), \tag{5.264}$$

derived in exactly the same way as Eq. (5.260).

As explained in subsection 5.8.3, the T matrix for rotationally symmetric particles calculated in the particle reference frame with the z-axis along the axis of rotation is block-diagonal, the different blocks $\mathbf{T}_m(P)$ corresponding to different m-values ($m = 0, 1, ..., n_{\max}$, where $n_{\max}$ is the converged n-value defined in subsection 5.8.4). Each block is computed separately by first calculating the respective $\mathbf{Q}_m$ and $\mathrm{Rg}\mathbf{Q}_m$ matrices from Eqs. (5.180)–(5.183) and (5.186)–(5.189) and then using

$$\mathbf{T}_m(P) = -(\mathrm{Rg}\mathbf{Q}_m)(\mathbf{Q}_m)^{-1}. \tag{5.265}$$

Using Eqs. (5.200) and (5.201) considerably shortens the computer time when $m = 0$. If the scatterer has a plane of symmetry perpendicular to the axis of rotation then us-

ing Eqs. (5.203)–(5.209) and restricting the integration in Eqs. (5.196)–(5.199) to $\cos\vartheta \in [-1, 0]$, with subsequent doubling of the result, further reduce the computational effort. The numerical stability and accuracy of the EBCM computations for particles with piecewise smooth surfaces, such as finite circular cylinders and osculating spheres, is improved by using special integration schemes that apply separate Gaussian quadratures to each smooth section (Barber and Hill 1990; Mishchenko *et al.* 1996a). The matrix inversion in Eq. (5.265) is performed using either standard Gaussian elimination with partial pivoting (Forsythe *et al.* 1977) or the special form of the LU-factorization method (Wielaard *et al.* 1997). As described in subsection 5.8.4, the latter provides much improved results for nonabsorbing or weakly absorbing particles. The matrices $(\mathbf{Q}_m)^{-1}$ and $\mathrm{Rg}\mathbf{Q}_m$ can be computed using either double-precision or extended-precision floating-point FORTRAN variables. As explained in subsection 5.8.4, the latter type of variable enables the code to handle significantly larger and/or more aspherical particles, albeit at the expense of increased computer time.

An important part of the code is the convergence procedure which checks whether the size of the T matrix and the number N_{G} of quadrature division points in Eq. (5.202) are sufficiently large that the scattering and absorption characteristics of interest are computed with the desired numerical accuracy (Mishchenko 1993). The procedure generates two $n_{\max}$-values: $n_{\max}$ and $\tilde{n}_{\max}$. The first, $n_{\max}$, is used to compute the matrices $\mathbf{Q}_m$, $\mathrm{Rg}\mathbf{Q}_m$, and $\mathbf{T}_m(P)$, whereas the second, $\tilde{n}_{\max}$, is used in the analytical orientation-averaging procedure described in Sections 5.4–5.6 and determines the maximal value of m. The fact that $\tilde{n}_{\max}$ is often significantly smaller than $n_{\max}$ means that a relatively large $n_{\max}$-value is required to accurately invert the $\mathbf{Q}_m$ matrices, whereas only a small number of leading T-matrix elements contribute to the orientation-averaged optical cross sections and scattering matrix elements. The code finds a reliable *a priori* estimate of both $n_{\max}$ and $\tilde{n}_{\max}$ using only the zeroth block, $\mathbf{T}_0(P)$, of the T matrix. $n_{\max}$ is increased in unit steps until the convergence criterion

$$\max\left\{\frac{|C_1(n_{\max})-C_1(n_{\max}-1)|}{|C_1(n_{\max})|}, \frac{|C_2(n_{\max})-C_2(n_{\max}-1)|}{|C_2(n_{\max})|}\right\} \le 0.1\Delta \tag{5.266}$$

is satisfied; here

$$C_1(n_{\max}) = -\frac{2\pi}{k_1^2}\mathrm{Re}\sum_{n=1}^{n_{\max}}(2n+1)[T_{0n0n}^{11}(P)+T_{0n0n}^{22}(P)], \tag{5.267}$$

$$C_2(n_{\max}) = \frac{2\pi}{k_1^2}\sum_{n=1}^{n_{\max}}(2n+1)\{|T_{0n0n}^{11}(P)|^2+|T_{0n0n}^{22}(P)|^2\}, \tag{5.268}$$

and Δ is the required absolute accuracy of computing the expansion coefficients in Eqs. (4.75)–(4.80). The parameter $\tilde{n}_{\max}$ is then found as the smallest positive integer that ensures the inequality

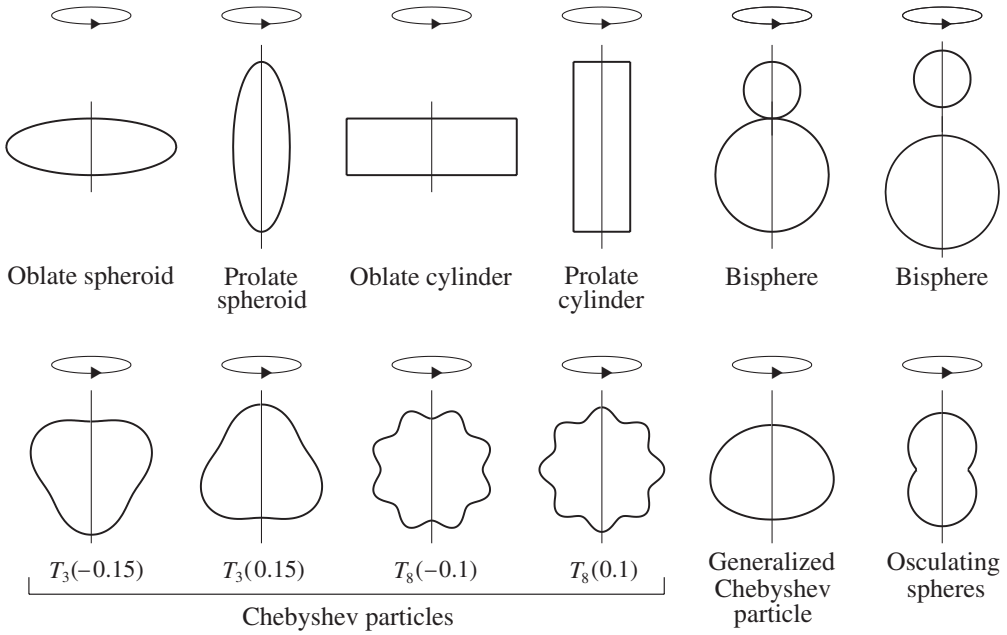

Figure 5.8. Typical rotationally symmetric shapes that can be handled by the *T*-matrix codes.

$$\max\left\{\frac{|C_1(\tilde{n}_{\max})-C_1(n_{\max})|}{|C_1(n_{\max})|},\frac{|C_2(\tilde{n}_{\max})-C_2(n_{\max})|}{|C_2(n_{\max})|}\right\}\leq 0.1\Delta. \tag{5.269}$$

After $n_{\max}$ has been determined, $N_{\rm G}$ in Eq. (5.202) is increased until $C_1(n_{\max})$ and $C_2(n_{\max})$ converge within 0.1Δ. The initial $N_{\rm G}$-value is chosen as a multiple of $n_{\max}$; the integer multiplicity factor NDGS is an important numerical parameter that must be optimized for each particle shape (see subsections 5.11.4 and 5.11.7).

5.11.2 Particle shapes and sizes

Although the *T*-matrix code can be easily tuned to handle essentially any rotationally symmetric shape, the current version of the code is directly applicable to spheroids, finite circular cylinders, and Chebyshev particles. Spheroids are formed by rotating an ellipse about its minor axis (oblate spheroid) or major axis (prolate spheroid) (Fig. 5.8). Their shape is described by the equation

$$r(\vartheta)=a\left(\sin^2\vartheta+\frac{a^2}{b^2}\cos^2\vartheta\right)^{-1/2}, \tag{5.270}$$

where b is the rotational (vertical) semi-axis and a is the horizontal semi-axis. The shape and size of a spheroid can be conveniently specified by the axis ratio a/b and the radius $r_{\rm s}$ of a sphere having the same surface area. The axis ratio is greater than 1 for oblate spheroids, smaller than 1 for prolate spheroids, and equal to 1 for spheres. Alternatively, one may use the axis ratio and the radius $r_{\rm v}$ of a sphere having the same volume.

Similarly, the shape and size of a finite circular cylinder (cf. Fig. 5.8) can be specified fully by the ratio of the diameter to the length, D/L, and the surface-equivalent-sphere radius r_s (or the volume-equivalent-sphere radius r_v). Note that D/L is smaller than 1 for prolate cylinders, equal to 1 for compact cylinders, and greater than 1 for oblate cylinders.

A Chebyshev particle is obtained by continuously deforming a sphere by means of a Chebyshev polynomial of degree n (Wiscombe and Mugnai 1986). Its shape is given by

$$r(\vartheta) = r_0[1 + \xi T_n(\cos\vartheta)], \qquad |\xi| < 1, \tag{5.271}$$

where r_0 is the radius of the unperturbed sphere, ξ is the deformation parameter, and $T_n(\cos\vartheta) = \cos n\vartheta$ is the Chebyshev polynomial of degree n (see Fig. 5.8, in which the different Chebyshev particles are indicated by the notation $T_n(\xi)$). All Chebyshev particles with $n \geq 2$ become partially concave as the absolute value of the deformation parameter increases and exhibit surface roughness in the form of waves running completely around the particle. Since the number of waves increases linearly with increasing n, the latter can be called the waviness parameter. The shape and size of a Chebyshev particle can be specified by the couplet $\{\xi, r_s\}$ (or by $\{\xi, r_v\}$).

5.11.3 Orientation and size averaging

After the T matrix for a specific shape and equivalent-sphere radius r has been computed, the orientation-averaged extinction, $\langle C_{ext}(r)\rangle$, and scattering, $\langle C_{sca}(r)\rangle$, cross sections per particle and the coefficients $\alpha_p^s(r)$ ($p = 1, 2, 3, 4$) and $\beta_p^s(r)$ ($p = 1, 2$) for identical particles in random orientation are calculated using Eqs. (5.107), (5.141), (5.126)–(5.130), and (4.109)–(4.114). Averaging over sizes is performed using straightforward numerical integration:

$$\langle C_{ext}\rangle = \int_{r_{min}}^{r_{max}} dr\, n(r)\langle C_{ext}(r)\rangle \approx \sum_{i=1}^{N_r} u_i n(r_i)\langle C_{ext}(r_i)\rangle, \tag{5.272}$$

$$\langle C_{sca}\rangle = \int_{r_{min}}^{r_{max}} dr\, n(r)\langle C_{sca}(r)\rangle \approx \sum_{i=1}^{N_r} u_i n(r_i)\langle C_{sca}(r_i)\rangle, \tag{5.273}$$

$$\begin{aligned}\alpha_p^s &= \frac{1}{\langle C_{sca}\rangle}\int_{r_{min}}^{r_{max}} dr\, n(r)\langle C_{sca}(r)\rangle\alpha_p^s(r)\\ &\approx \frac{1}{\langle C_{sca}\rangle}\sum_{i=1}^{N_r} u_i n(r_i)\langle C_{sca}(r_i)\rangle\alpha_p^s(r_i), \qquad p = 1, ..., 4,\end{aligned} \tag{5.274}$$

$$\begin{aligned}\beta_p^s &= \frac{1}{\langle C_{sca}\rangle}\int_{r_{min}}^{r_{max}} dr\, n(r)\langle C_{sca}(r)\rangle\beta_p^s(r)\\ &\approx \frac{1}{\langle C_{sca}\rangle}\sum_{i=1}^{N_r} u_i n(r_i)\langle C_{sca}(r_i)\rangle\beta_p^s(r_i), \qquad p = 1, 2,\end{aligned} \tag{5.275}$$

where $n(r)$ is an appropriate normalized distribution of equivalent-sphere radii. The use of analytical size distribution functions in actual computer calculations was discussed in subsection 5.10.1.

After the extinction and scattering cross sections and the expansion coefficients have been calculated, all other cross sections, the single-scattering albedo, the asymmetry parameter, and the elements of the normalized Stokes scattering matrix for an arbitrary set of scattering angles are found from Eqs. (4.43)–(4.45), (4.75)–(4.80), and (4.92). The Wigner *d*-functions appearing in expansions (4.75)–(4.80) are calculated using the recurrence relation (B.22) and initial values given by Eqs. (B.23) and (B.24).

5.11.4 Input parameters of the code

ICHOICE:

If ICHOICE = 1, then the code computes the inverse matrix $\mathbf{Q}^{-1}$ using the special LU-factorization scheme. If ICHOICE = 2, the inverse matrix is computed using the standard Gauss elimination procedure with partial pivoting. The execution time is roughly the same in both cases, but the LU-factorization procedure allows computations for significantly larger particles in the case of weak or no absorption (i.e., small or zero imaginary part of the relative refractive index).

RAT:

If RAT = 1, the size of the nonspherical particles is specified in terms of the equal-volume-sphere radius r_{v}. If RAT $\neq$ 1, the size is specified in terms of the surface-equivalent-sphere radius r_{s}.

NDISTR, AXI, B, GAM, NPNAX, AXMAX:

The parameter NDISTR specifies the type of the particle size distribution. For the modified gamma distribution (5.242), NDISTR = 1, AXI = α, B = r_c, and GAM = γ. For the log normal distribution (5.243), NDISTR = 2, AXI = r_g, B = $\ln^2\sigma_g$, and GAM is ignored. For the power law distribution (5.244), NDISTR = 3, AXI = r_{eff}, B = v_{eff}, and GAM is ignored. In this case the parameters R1 and R2 (see below) are calculated from Eqs. (5.244) and (5.248)–(5.250) for given r_{eff} and v_{eff}. For the gamma distribution (5.245), NDISTR = 4, AXI = a, B = b, and GAM is ignored. Finally, for the modified power law distribution (5.246), NDISTR = 5, B = α, and AXI and GAM are ignored. The code computes NPNAX size distributions of the same type and with the same values of B (and GAM for NDISTR = 1) in one run. The parameter AXI varies from AXMAX down to AXMAX/NPNAX in steps of AXMAX/NPNAX. If only one size distribution is needed, NPNAX is set to 1 and AXMAX is set equal to AXI of this size distribution.

R1 and R2:

$\mathrm{R1} = r_{\min}$ and $\mathrm{R2} = r_{\max}$ are the minimal and maximal radii of the size distribution for NDISTR = 1–4. R1 and R2 are calculated automatically for the power law distribution NDISTR = 3 with given $\mathrm{AXI} = r_{\mathrm{eff}}$ and $\mathrm{B} = v_{\mathrm{eff}}$, but must be explicitly specified for other distributions after the statements

```
DO 600 IAX = 1, NPNAX
    AXI = AXMAX – DAX * DFLOAT(IAX – 1)
```

in the main program. For the modified power law distribution NDISTR = 5, $r_{\min} = 0$, $\mathrm{R1} = r_1$, and $\mathrm{R2} = r_2 = r_{\max}$.

NKMAX:

This parameter determines the number N_r of Gaussian quadrature points in Eqs. (5.272)–(5.275). NKMAX is an integer such that NKMAX + 2 is the number of quadrature points on the interval [R1, R2] (and on the interval [0, R1] for NDISTR = 5) for particles with AXI = AXMAX. For particles with AXI = AXMAX – AXMAX/NPNAX, AXMAX – 2*AXMAX/NPNAX, etc., the number of Gaussian division points decreases linearly.

LAM:

$\mathrm{LAM} = \lambda_1$ is the wavelength of the incident light in the surrounding medium.

MRR and MRI:

$\mathrm{MRR} = \mathrm{Re}\, m$ and $\mathrm{MRI} = \mathrm{Im}\, m$ are the real and imaginary parts of the relative refractive index, respectively. MRI must be non-negative.

EPS and NP:

These parameters specify the particle shape (cf. subsection 5.11.2). For spheroids, NP = –1, and EPS = a/b is the ratio of the horizontal to the rotational semi-axes. For circular cylinders, NP = –2 and EPS = D/L is the diameter-to-length ratio. For Chebyshev particles, NP, which must be positive, is the degree of the Chebyshev polynomial n in Eq. (5.271), while EPS = ξ is the deformation parameter.

DDELT:

This parameter enters the convergence criteria of Eqs. (5.266) and (5.269) and specifies the required numerical accuracy of the T-matrix calculations.

NPNA:

NPNA is the number of scattering angles at which the scattering matrix is computed. The corresponding scattering angles are given by 180*(I–1)/(NPNA–1) (in degrees), where I = 1, …, NPNA numbers the angles. This way of choosing scattering angles can be readily changed in the subroutine MATR (see subsection 5.10.2).

NDGS:
This integer parameter controls the initial value of the number N_G of Gaussian division points in the numerical evaluation of the integrals over the particle surface (cf. Eq. (5.202) and subsection 5.11.1)). For compact particles, the recommended value of NDGS is 2. For highly aspherical particles, larger values (NDGS = 3, 4, ...) may be necessary to obtain convergence (cf. subsection 5.11.7). Although the code checks the convergence over the number of Gaussian division points N_G (cf. subsection 5.11.1), it does not check the convergence over the initial value of N_G, which is equal to the product of n_{max} and NDGS. Therefore, too small a value of NDGS may cause false convergence in some cases, especially for highly elongated or flattened particles, and control comparisons of results obtained with different NDGS values are recommended.

5.11.5 Output information

R1 and R2:
For the power law size distribution (NDISTR = 3), $R1 = r_1$ and $R2 = r_2$ are the minimal and maximal radii, respectively, calculated for the input values of r_{eff} and v_{eff}.

REFF and VEFF:
$REFF = r_{eff}$ and $VEFF = v_{eff}$ are the effective radius and the effective variance of the size distribution, respectively.

CEXT and CSCA:
$CEXT = \langle C_{ext} \rangle$ and $CSCA = \langle C_{sca} \rangle$ are the orientation- and size-averaged extinction and scattering cross sections per particle, respectively.

< COS > and W:
$< COS > = \langle \cos\Theta \rangle$ and $W = \varpi$ are the orientation- and size-averaged asymmetry parameter and the single-scattering albedo, respectively.

ALPHA1, …, BETA2:
$ALPHA1(S) = \alpha_1^s$, $ALPHA2(S) = \alpha_2^s$, $ALPHA3(S) = \alpha_3^s$, $ALPHA4(S) = \alpha_4^s$, $BETA1(S) = \beta_1^s$, and $BETA2(S) = \beta_2^s$ are the coefficients appearing in the expansions (4.75)–(4.80).

F11, F22, F33, F44, F12, and F34:
$F11 = a_1$, $F22 = a_2$, $F33 = a_3$, $F44 = a_4$, $F12 = b_1$, and $F34 = b_2$ are the elements of the normalized Stokes scattering matrix (4.51).

5.11.6 Additional comments and recipes

The input parameters r_c, r_g, r_{eff}, a, r_1, r_2, and λ_1 must be specified in the same units of length. If these parameters are specified, for example, in micrometers then the extinction and scattering cross sections generated by the code are given in square micrometers.

The physical correctness of the numerical results is tested using inequalities derived by van der Mee and Hovenier (1990). Although the message that the test of van der Mee and Hovenier is satisfied does not guarantee the correctness of the results, the message that the test is not satisfied means that the results are likely to be wrong.

The required execution time rapidly increases with increasing values of the ratio radius/wavelength and/or with increasing particle asphericity. This should be taken into account in planning massive computations. The use of an optimizing compiler on IBM RISC workstations has been found to save about 70% of computer time compared with unoptimized code.

Execution can be automatically terminated if dimensions of certain arrays are not large enough. In all cases, a message appears explaining the cause of termination. The message "WARNING: NGAUSS = NPNG1" means that convergence over the parameter N_{G} cannot be obtained for the NPNG1 value specified in the PARAMETER statement. Often, however, this does not indicate a serious problem, especially for compact particles.

Larger and/or more aspherical particles may require larger values of the parameters NPN1, NPN4, and NPNG1. It is recommended that the relations NPN1 = NPN4 + 25 and NPNG1 = (NDGS+1)*NPN1 be maintained. Note that the memory requirement increases as the third power of NPN4. If the memory of a computer is too small to accommodate the code in its current setting then the parameters NPN1, NPN4, and NPNG1 should be reduced. However, this will decrease the maximal particle size parameter that can be handled by the code.

In some cases any increase of NPN1 will not make the *T*-matrix computations convergent. This means that the particle is too extreme in terms of size parameter and/or aspect ratio for a given value of the relative refractive index. The main program contains several PRINT statements which are currently commented out. If uncommented, these statements will produce the ratios that enter the convergence criteria of Eqs. (5.266) and (5.269) and can be used to determine whether the *T*-matrix computations for given particle parameters will converge at all.

The recommended value of the parameter DDELT is 0.001 (Mishchenko 1993) because larger values can generate false convergence. The message "WARNING: W IS GREATER THAN 1" means that the single-scattering albedo exceeds the maximal possible value, unity. If W is greater than 1 by significantly more than DDELT, this message can be an indication of numerical instability caused by extreme values of particle parameters.

Some of the common blocks are used to save memory rather than to transfer data. Therefore, if a compiler generates a warning message that the lengths of a common block are different in different subroutines, this is not a manifestation of a programming error.

In computations for spheres, one should use EPS = 1.000001 instead of EPS = 1 because the use of EPS = 1 can cause overflows in some rare cases. To calculate scattering by a monodisperse particle in random orientation, one may use the options

```
NPNAX = 1
AXMAX = r
B = 1D–1
NKMAX = –1
NDISTR = 4
⋮
DO 600 IAX = 1, NPNAX
    AXI = AXMAX – DAX*DFLOAT(IAX–1)
    R1 = 0.9999999*AXI
    R2 = 1.0000001*AXI
    ⋮
```

where r is the equivalent-sphere radius.

When there is no definite preference for a specific size distribution, we recommend using the power law or the modified power law size distribution rather than the gamma, modified gamma, or log normal distributions, because this can render convergent solutions for larger $r_{\rm eff}$ and $v_{\rm eff}$ values (Mishchenko and Travis 1994c). If results for many different size distributions are required and the relative refractive index is fixed, then an alternative approach can be more efficient than running this code many times. Specifically, scattering results should be computed for monodisperse particles with sizes ranging from essentially zero to some maximal value with a small step size. The results should be stored on disk and then can be used along with spline interpolation to compute the scattering characteristics of particles with intermediate sizes and to evaluate numerically the integrals in Eqs. (5.272)–(5.275). Scattering patterns for monodisperse nonspherical particles in random orientation are smoother than those for monodisperse spheres (e.g., Mishchenko and Travis 1994b and Section 10.1), and spline interpolation usually produces satisfactory results. In this way, averaging over any new size distribution can be a matter of a few seconds of computer time.

Table 5.3. Maximal convergent size parameters x_s and x_a and the respective NDGS values in extended-precision EBCM calculations for monodisperse oblate spheroids with relative refractive index 1.311 and axis ratios a/b varying from $3/2$ to 20

a/b	x_s	x_a	NDGS
20	12	17	30
10	17	24	15
5	27	37	5
3	42	54	4
2	92	111	3
$3/2$	>160	>180	2

5.11.7 Illustrative examples

As for all exact techniques for calculating electromagnetic scattering by nonspherical particles, the performance of the *T*-matrix code depends on the numerical options used and particle characteristics such as shape, size parameter, and relative refractive index. Table 5.3 shows the values of the maximum convergent surface-equivalent-sphere size parameter $x_s = 2\pi r_s/\lambda_1$ for monodisperse oblate spheroids with relative refractive index 1.311 and axis ratios a/b varying from 3/2 to 20. The results are obtained for DDELT = 0.001 using the extended-precision version of the *T*-matrix code and the LU-factorization matrix inversion scheme. Note that the maximal size parameter $x_a = 2\pi a/\lambda_1$ measured along the major semi-axis *a* can be significantly larger than the maximal surface-equivalent-sphere size parameter, especially for highly flattened spheroids. Table 5.3 also shows the respective values of the parameter NDGS, which controls the initial number of Gauss points in Eq. (5.202). Table 5.4 is analogous to Table 5.3, but is computed for prolate spheroids and shows the major-axis size parameter $x_b = 2\pi b/\lambda_1$ rather than x_a. It is clear that the maximal convergent size parameters strongly depend on the spheroid axis ratio and significantly increase as the particles become less aspherical. Tables 5.3 and 5.4 also demonstrate that converged computations for highly flattened and elongated spheroids may require large values of the parameter NDGS. Table 5.5 shows that the maximal convergent size parameters also depend on the particle relative refractive index and can significantly decrease with increasing m_R and/or m_I. Table 5.6 demonstrates the advantage of using extended-precision instead of double-precision computer arithmetic and using the special LU-factorization-based matrix inversion procedure in place of the traditional Gauss elimination scheme with partial pivoting. Finally, comparison of Tables 5.6 and 5.7 shows that although cylinders are particles with sharp rectangular edges, they can be handled by the *T*-matrix code almost as efficiently as smooth spheroids with a similar aspect ratio.

Table 5.4. Maximal convergent size parameters x_s and x_b and the respective NDGS values in extended-precision EBCM calculations for monodisperse prolate spheroids with relative refractive index 1.311 and axis ratios a/b varying from $2/3$ to $1/20$

a/b	x_s	x_b	NDGS
1/20	3	15	30
1/10	7	25	25
1/5	14	35	10
1/3	30	57	5
1/2	73	112	2
2/3	> 150	> 194	2

Table 5.5. Maximal convergent size parameters x_s and x_a and the respective NDGS values in extended-precision EBCM calculations for monodisperse oblate spheroids with axis ratio $a/b = 3$ and varying relative refractive index

Refractive index	x_s	x_a	NDGS
1.311	42	54	4
1.53 + i0.008	38	48	4
1.78 + i0.005	32	41	4
2 + i0.6	25	32	4

Table 5.6. Maximal convergent size parameter x_s versus axis ratio a/b in different types of EBCM computations for monodisperse oblate spheroids with relative refractive index 1.311

a/b	Extended precision LU-factorization	Double precision LU-factorization	Double precision Gauss elimination
20	12	4	4
10	17	7	5
5	27	12	7
3	42	19	10
2	92	38	14
3/2	> 160	97	24

Extensive comparisons of EBCM results with results generated by the separation of variables method for spheroids have shown that (i) the internal convergence of EBCM computations with increasing n_{max} is a reliable indication of their absolute convergence, and (ii) the EBCM is capable of producing very accurate numbers suit-

Table 5.7. Maximal convergent size parameter x_s versus diameter-to-length ratio D/L in different types of EBCM computations for monodisperse oblate cylinders with relative refractive index 1.311

D/L	Extended precision LU-factorization	Double precision LU-factorization	Double precision Gauss elimination
20	7	1.5	0.8
10	13	3	0.9
5	24	10	1.2
3	43	17	5
2	70	30	12
1	>180	93	21

able for use as benchmarks in testing the performance of other theoretical as well as experimental techniques (Kuik *et al.* 1992; Hovenier *et al.* 1996). Benchmark numbers for randomly oriented spheroids, circular cylinders, and Chebyshev particles have been published by Mishchenko (1991a), Kuik *et al.* (1992), Mishchenko *et al.* (1996a), and Wielaard *et al.* (1997). They cover the range of equivalent-sphere size parameters from a few units up to 60 and are given with up to nine correct decimals.

To supplement the existing set of benchmark results, we list in Table 5.8 the expansion coefficients α_p^s ($p = 1, 2, 3, 4$) and β_p^s ($p = 1, 2$) and in Table 5.9 the elements of the normalized Stokes scattering matrix for a polydispersion of randomly oriented oblate spheroids with an aspect ratio of 1.8 and a relative refractive index of $1.53 + i0.008$. The size distribution is given by Eq. (5.244); r_1 and r_2 correspond to the effective surface-equivalent-sphere radius $r_{\rm eff} = 0.6\,\mu{\rm m}$ and the effective variance $v_{\rm eff} = 0.2$. The wavelength of the incident light in the surrounding medium is $\lambda_1 = 0.63\,\mu{\rm m}$. The integrals in Eqs. (5.272)–(5.275) were evaluated using 500 Gauss quadrature points. Other output parameters are as follows:

$$\langle C_{\rm ext}\rangle = 1.87101\,\mu{\rm m}^2, \qquad \langle C_{\rm sca}\rangle = 1.73760\,\mu{\rm m}^2,$$
$$\varpi = 0.928698, \qquad \langle\cos\Theta\rangle = 0.702091,$$
$$r_1 = 0.245830\,\mu{\rm m}, \qquad r_2 = 1.194170\,\mu{\rm m}.$$

The entire calculation took five minutes on an IBM RISC model 397 workstation. All output numbers are expected to be accurate to within ± 1 in the last decimals given.

5.12 *T*-matrix code for a homogeneous, rotationally symmetric particle in an arbitrary orientation

The FORTRAN *T*-matrix code for computing the amplitude and phase matrices for a homogeneous rotationally symmetric particle in an arbitrary orientation is available

Table 5.8. Expansion coefficients for a power law size distribution of homogeneous, randomly oriented oblate spheroids (see text)

s	α_1^s	α_2^s	α_3^s	α_4^s	β_1^s	β_2^s
0	1.00000	0.00000	0.00000	0.89928	0.00000	0.00000
1	2.10627	0.00000	0.00000	2.14323	0.00000	0.00000
2	2.79060	3.87999	3.71405	2.77094	– 0.05078	0.11537
3	3.00175	3.43981	3.37319	2.99128	– 0.09531	– 0.16185
4	2.83538	3.40580	3.34945	2.82333	– 0.04264	– 0.10973
5	2.60924	2.83160	2.81673	2.63846	– 0.02124	– 0.12877
6	2.39351	2.67150	2.60857	2.38094	– 0.04844	– 0.15852
7	2.12900	2.26075	2.23342	2.13666	– 0.00214	– 0.15971
8	1.89793	2.05330	2.02056	1.90065	– 0.02984	– 0.13873
9	1.67405	1.75096	1.72982	1.68165	– 0.01212	– 0.14309
10	1.47871	1.57690	1.54673	1.47595	– 0.02144	– 0.13788
11	1.27239	1.32218	1.31043	1.28250	– 0.01149	– 0.11999
12	1.10939	1.17407	1.14826	1.10498	– 0.01821	– 0.12428
13	0.92807	0.96196	0.95375	0.93662	– 0.01070	– 0.10080
14	0.79349	0.83674	0.81484	0.78766	– 0.01320	– 0.10570
15	0.64122	0.66391	0.65900	0.64845	– 0.00874	– 0.07936
16	0.53774	0.56598	0.54728	0.53055	– 0.00853	– 0.08365
17	0.41897	0.43337	0.43096	0.42479	– 0.00687	– 0.05712
18	0.34603	0.36382	0.34899	0.33914	– 0.00630	– 0.06120
19	0.25939	0.26825	0.26772	0.26439	– 0.00693	– 0.03890
20	0.21083	0.22196	0.21000	0.20432	– 0.00589	– 0.04365
21	0.14967	0.15492	0.15512	0.15334	– 0.00643	– 0.02593
22	0.11751	0.12443	0.11526	0.11193	– 0.00501	– 0.02989
23	0.07529	0.07824	0.07872	0.07778	– 0.00506	– 0.01639
24	0.05545	0.05944	0.05252	0.05057	– 0.00289	– 0.01953
25	0.02894	0.03041	0.03051	0.02993	– 0.00154	– 0.00847
26	0.01933	0.02088	0.01713	0.01637	– 0.00062	– 0.00899
27	0.00773	0.00822	0.00802	0.00776	0.00028	– 0.00288
28	0.00451	0.00492	0.00380	0.00359	0.00015	– 0.00236
29	0.00144	0.00154	0.00138	0.00130	0.00024	– 0.00066
30	0.00069	0.00074	0.00049	0.00046	0.00008	– 0.00035
31	0.00017	0.00018	0.00014	0.00013	0.00004	– 0.00009
32	0.00010	0.00011	0.00003	0.00003	0.00003	– 0.00004
33	0.00001	0.00001	0.00001	0.00001	0.00000	0.00000
34	0.00000	0.00000	0.00000	0.00000	0.00000	0.00000

Table 5.9. Elements of the normalized Stokes scattering matrix for a power law size distribution of homogeneous, randomly oriented oblate spheroids (see text)

Θ (deg)	$a_1(\Theta)$	$a_2(\Theta)$	$a_3(\Theta)$	$a_4(\Theta)$	$b_1(\Theta)$	$b_2(\Theta)$
0	30.8948	30.8569	30.8569	30.8190	0.0000	0.0000
10	17.7021	17.6717	17.6513	17.6282	0.0837	0.5816
20	6.7304	6.7047	6.6468	6.6343	0.0846	0.4295
30	3.1470	3.1251	3.0620	3.0572	0.0839	0.2200
40	1.5974	1.5778	1.5155	1.5151	0.0859	0.1116
50	0.8639	0.8454	0.7853	0.7872	0.0786	0.0365
60	0.5079	0.4895	0.4320	0.4353	0.0670	– 0.0069
70	0.3337	0.3146	0.2566	0.2614	0.0529	– 0.0356
80	0.2529	0.2319	0.1686	0.1755	0.0382	– 0.0585
90	0.2244	0.1997	0.1242	0.1338	0.0244	– 0.0833
100	0.2255	0.1947	0.1037	0.1166	0.0085	– 0.1089
110	0.2344	0.1963	0.0941	0.1106	– 0.0111	– 0.1256
120	0.2318	0.1870	0.0862	0.1063	– 0.0267	– 0.1192
130	0.2137	0.1647	0.0724	0.0956	– 0.0271	– 0.0927
140	0.1924	0.1415	0.0499	0.0753	– 0.0107	– 0.0665
150	0.1780	0.1281	0.0210	0.0464	0.0120	– 0.0512
160	0.1652	0.1222	– 0.0109	0.0103	0.0295	– 0.0306
170	0.1610	0.0994	– 0.0658	– 0.0187	0.0161	0.0319
180	0.2876	0.1526	– 0.1526	– 0.0176	0.0000	0.0000

on the World Wide Web at http://www.giss.nasa.gov/~crmim. Many relevant aspects of *T*-matrix computations were discussed in the preceding section. Therefore, below we mostly focus on issues specific to particles in a fixed orientation, list the input and output parameters of the code, and provide several benchmark results.

The general scheme for computing the single-particle *T*-matrix in the particle reference frame having its *z*-axis along the axis of particle symmetry was described in subsection 5.11.1. The only difference is that now the parameter $\widetilde{n}_{\max}$ is ignored, so that the maximal value of m is equal to $n_{\max}$ and the entire *T*-matrix is used in amplitude and phase matrix computations.

The current version of the *T*-matrix code is directly applicable to spheroids, finite circular cylinders, Chebyshev particles, and so-called generalized Chebyshev particles (Fig. 5.8). The latter are described by the expansion

$$r(\vartheta) = r_0 \left[1 + \sum_{n=0}^{N} c_n T_n(\cos\vartheta) \right] \tag{5.276}$$

and are often used to model the shape of distorted falling raindrops (Chuang and Beard 1990). The size of either type of particle is specified by the surface-equivalent-sphere radius r_s or the volume-equivalent-sphere radius r_v.

The orientation of a scattering particle with respect to the laboratory reference

frame is specified by the Euler angles of rotation (α, β, γ) that describe the transformation of the laboratory reference frame into the particle reference frame (cf. Section 2.4). Since the particle is assumed to be rotationally symmetric, the amplitude scattering matrix with respect to the laboratory reference frame is given by Eq. (2.72) with $\gamma = 0$. The formulas for computing the amplitude scattering matrix with respect to the particle reference frame follow from Eqs. (5.11)–(5.17) and (5.36)–(5.37):

$$S_{11}^{P}(\hat{\mathbf{n}}^{\rm sca}, \hat{\mathbf{n}}^{\rm inc}) = \frac{1}{k_1}\sum_{n=1}^{n_{\max}}\sum_{n'=1}^{n_{\max}}\sum_{m=0}^{\min(n,\,n')}(2-\delta_{m0})$$
$$\times \mathrm{i}^{n'-n-1}\left[\frac{(2n+1)(2n'+1)}{n(n+1)n'(n'+1)}\right]^{1/2}\cos[m(\varphi_P^{\rm sca}-\varphi_P^{\rm inc})]$$
$$\times[T_{mnmn'}^{11}(P)\pi_{mn}(\vartheta_P^{\rm sca})\pi_{mn'}(\vartheta_P^{\rm inc}) + T_{mnmn'}^{21}(P)\tau_{mn}(\vartheta_P^{\rm sca})\pi_{mn'}(\vartheta_P^{\rm inc})$$
$$+ T_{mnmn'}^{12}(P)\pi_{mn}(\vartheta_P^{\rm sca})\tau_{mn'}(\vartheta_P^{\rm inc}) + T_{mnmn'}^{22}(P)\tau_{mn}(\vartheta_P^{\rm sca})\tau_{mn'}(\vartheta_P^{\rm inc})], \tag{5.277}$$

$$S_{12}^{P}(\hat{\mathbf{n}}^{\rm sca}, \hat{\mathbf{n}}^{\rm inc}) = \frac{2}{k_1}\sum_{n=1}^{n_{\max}}\sum_{n'=1}^{n_{\max}}\sum_{m=1}^{\min(n,\,n')}\mathrm{i}^{n'-n-1}\left[\frac{(2n+1)(2n'+1)}{n(n+1)n'(n'+1)}\right]^{1/2}\sin[m(\varphi_P^{\rm sca}-\varphi_P^{\rm inc})]$$
$$\times[T_{mnmn'}^{11}(P)\pi_{mn}(\vartheta_P^{\rm sca})\tau_{mn'}(\vartheta_P^{\rm inc}) + T_{mnmn'}^{21}(P)\tau_{mn}(\vartheta_P^{\rm sca})\tau_{mn'}(\vartheta_P^{\rm inc})$$
$$+ T_{mnmn'}^{12}(P)\pi_{mn}(\vartheta_P^{\rm sca})\pi_{mn'}(\vartheta_P^{\rm inc}) + T_{mnmn'}^{22}(P)\tau_{mn}(\vartheta_P^{\rm sca})\pi_{mn'}(\vartheta_P^{\rm inc})], \tag{5.278}$$

$$S_{21}^{P}(\hat{\mathbf{n}}^{\rm sca}, \hat{\mathbf{n}}^{\rm inc}) = -\frac{2}{k_1}\sum_{n=1}^{n_{\max}}\sum_{n'=1}^{n_{\max}}\sum_{m=1}^{\min(n,\,n')}\mathrm{i}^{n'-n-1}\left[\frac{(2n+1)(2n'+1)}{n(n+1)n'(n'+1)}\right]^{1/2}\sin[m(\varphi_P^{\rm sca}-\varphi_P^{\rm inc})]$$
$$\times[T_{mnmn'}^{11}(P)\tau_{mn}(\vartheta_P^{\rm sca})\pi_{mn'}(\vartheta_P^{\rm inc}) + T_{mnmn'}^{21}(P)\pi_{mn}(\vartheta_P^{\rm sca})\pi_{mn'}(\vartheta_P^{\rm inc})$$
$$+ T_{mnmn'}^{12}(P)\tau_{mn}(\vartheta_P^{\rm sca})\tau_{mn'}(\vartheta_P^{\rm inc}) + T_{mnmn'}^{22}(P)\pi_{mn}(\vartheta_P^{\rm sca})\tau_{mn'}(\vartheta_P^{\rm inc})], \tag{5.279}$$

$$S_{22}^{P}(\hat{\mathbf{n}}^{\rm sca}, \hat{\mathbf{n}}^{\rm inc}) = \frac{1}{k_1}\sum_{n=1}^{n_{\max}}\sum_{n'=1}^{n_{\max}}\sum_{m=0}^{\min(n,\,n')}(2-\delta_{m0})$$
$$\times \mathrm{i}^{n'-n-1}\left[\frac{(2n+1)(2n'+1)}{n(n+1)n'(n'+1)}\right]^{1/2}\cos[m(\varphi_P^{\rm sca}-\varphi_P^{\rm inc})]$$
$$\times[T_{mnmn'}^{11}(P)\tau_{mn}(\vartheta_P^{\rm sca})\tau_{mn'}(\vartheta_P^{\rm inc}) + T_{mnmn'}^{21}(P)\pi_{mn}(\vartheta_P^{\rm sca})\tau_{mn'}(\vartheta_P^{\rm inc})$$
$$+ T_{mnmn'}^{12}(P)\tau_{mn}(\vartheta_P^{\rm sca})\pi_{mn'}(\vartheta_P^{\rm inc}) + T_{mnmn'}^{22}(P)\pi_{mn}(\vartheta_P^{\rm sca})\pi_{mn'}(\vartheta_P^{\rm inc})]. \tag{5.280}$$

The angular functions $\pi_{mn}(\vartheta)$ and $\tau_{mn}(\vartheta)$ defined by Eqs. (5.16) and (5.17) are found from recurrence relations (B.22) and (B.26) and initial conditions (B.23) and (B.24). After the amplitude matrix with respect to the laboratory reference frame has been computed, the phase matrix is calculated using Eqs. (2.106)–(2.121).

The *T*-matrix code has the following *input* parameters.

ICHOICE:
If ICHOICE = 1 then the code computes the inverse matrix $\mathbf{Q}^{-1}$ using the special LU-factorization scheme. If ICHOICE = 2, the inverse matrix is computed using the standard Gauss elimination procedure with partial pivoting.

RAT:
If RAT = 1 then the size of the nonspherical particle is specified in terms of the volume-equivalent-sphere radius $r_{\rm v}$. If RAT $\neq 1$ then the size is specified in terms of the surface-equivalent-sphere radius $r_{\rm s}$.

AXI:
AXI is the equivalent-sphere radius $r_{\rm v}$ or $r_{\rm s}$.

LAM:
LAM $= \lambda_1$ is the wavelength of the incident light in the surrounding medium. LAM must be specified in the same units of length as AXI.

MRR and MRI:
MRR $= {\rm Re}\, m$ and MRI $= {\rm Im}\, m$ are the real and imaginary parts of the relative refractive index, respectively. MRI must be non-negative.

EPS and NP:
These parameters specify the shape of the particle. For a spheroid, NP = –1 and EPS $= a/b$ is the ratio of the horizontal to the rotational semi-axis. For a circular cylinder, NP = –2 and EPS $= D/L$ is the diameter-to-length ratio. For a Chebyshev particle, NP must be positive and is the degree of the Chebyshev polynomial *n* in Eq. (5.271), while EPS = ξ is the deformation parameter. For a generalized Chebyshev particle, NP = –3 and the expansion coefficients entering Eq. (5.276) are specified in the subroutine DROP.

DDELT:
This parameter enters the convergence criterion (5.266) and specifies the required numerical accuracy of the *T*-matrix calculations.

NDGS:
This integer parameter controls the initial value of the number $N_{\rm G}$ of Gaussian division points in the numerical evaluation of integrals over the particle surface (cf. subsection 5.11.4).

ALPHA and BETA:
ALPHA $= \alpha$ and BETA $= \beta$ are the Euler angles (in degrees) specifying the orientation of the axially symmetric particle with respect to the laboratory reference frame.

THET0, PHI0, THET, and PHI:
The angles THET0 = $\vartheta_L^{\rm inc}$, PHI0 = $\varphi_L^{\rm inc}$, THET = $\vartheta_L^{\rm sca}$, and PHI = $\varphi_L^{\rm sca}$ (in degrees) specify the incidence and scattering directions with respect to the laboratory reference frame (cf. Section 2.4).

The parameters ALPHA, BETA, THET0, PHI0, THET, and PHI are specified at the end of the main program before the line

CALL AMPL (NMAX, ...)

The part of the main program following the line

C COMPUTATION OF THE AMPLITUDE AND PHASE MATRICES

can be repeated any number of times for different directions of illumination and scattering and different particle orientations because by this time the $\mathbf{T}(P)$ matrix for the given scattering particle has already been computed.

As the *output*, the code generates the four complex-valued elements of the amplitude scattering matrix $\mathbf{S}^L(\vartheta_L^{\rm sca}, \varphi_L^{\rm sca}; \vartheta_L^{\rm inc}, \varphi_L^{\rm inc}; \alpha, \beta, \gamma = 0)$ and the 16 real-valued elements of the Stokes phase matrix $\mathbf{Z}^L(\vartheta_L^{\rm sca}, \varphi_L^{\rm sca}; \vartheta_L^{\rm inc}, \varphi_L^{\rm inc}; \alpha, \beta, \gamma = 0)$ with respect to the laboratory reference frame. If AXI and LAM are specified, e.g., in micrometers, then the dimensions of the elements of the amplitude and phase matrices are micrometers and square micrometers, respectively.

To demonstrate the performance of the code, we applied it to the following four particle models:

- prolate spheroid with $a/b = 1/2$;
- prolate circular cylinder with a diameter-to-length ratio $1/2$;
- Chebyshev particle, Eq. (5.271), with $n = 4$ and $\xi = 0.1$;
- generalized Chebyshev particle with shape given by Eq. (5.276) with N =10, c_0 = –0.0481, c_1 = 0.0359, c_2 = –0.1263, c_3 = 0.0244, c_4 = 0.0091, c_5 = –0.0099, c_6 = 0.0015, c_7 = 0.0025, c_8 = –0.0016, c_9 = –0.0002, and c_{10} = 0.0010 (cf. Fig. 5.8).

The surface-equivalent-sphere radius for the first three particles and the volume-equivalent-sphere radius for the fourth particle is 10 μm. All particles have the same relative refractive index, 1.5 + i0.02, and the same orientation with respect to the laboratory reference frame, given by $\alpha = 145°$ and $\beta = 52°$. The directions of the incident and scattered beams relative to the laboratory reference frame are given by the angles $\vartheta_L^{\rm inc} = 56°$, $\varphi_L^{\rm inc} = 114°$, $\vartheta_L^{\rm sca} = 65°$, and $\varphi_L^{\rm sca} = 128°$. The wavelength of the incident light in the surrounding medium is 6.283185 μm. The respective amplitude scattering matrices (with elements given in micrometers) are as follows:

$$\begin{bmatrix} -5.0941 + {\rm i}24.402 & -1.9425 + {\rm i}1.9971 \\ -1.1521 - {\rm i}3.0978 & -6.9323 + {\rm i}24.748 \end{bmatrix}, \tag{5.281}$$

$$\begin{bmatrix} -1.727 + \mathrm{i}19.706 & -0.562 + \mathrm{i}0.247 \\ -2.013 - \mathrm{i}2.398 & -3.088 + \mathrm{i}20.401 \end{bmatrix}, \tag{5.282}$$

$$\begin{bmatrix} 4.5123 + \mathrm{i}18.092 & -1.6350 + \mathrm{i}3.5274 \\ -3.0970 - \mathrm{i}0.9215 & 3.2658 + \mathrm{i}18.617 \end{bmatrix}, \tag{5.283}$$

$$\begin{bmatrix} 11.307 + \mathrm{i}9.6184 & -2.6519 + \mathrm{i}2.3589 \\ -4.9044 - \mathrm{i}0.6241 & 9.9947 + \mathrm{i}11.295 \end{bmatrix}. \tag{5.284}$$

These numbers are expected to be accurate to within ± 2 in the last decimals given.

In order to provide an additional test of the accuracy of the computer code for particles in a fixed orientation, the authors have used it to calculate the elements of the normalized Stokes scattering matrix for a uniform orientation distribution by first numerically evaluating the angular integrals in Eq. (5.108) and then using Eq. (4.51). These results were then compared with those rendered by the code based on the analytical averaging method for randomly oriented particles (Section 5.11). Since the latter code completely avoids the evaluation of the amplitude scattering matrix for specific particle orientations and illumination and scattering directions, it provides an excellent independent check. The perfect agreement that was found (to five and more significant digits) suggests that both codes provide high numerical accuracy and can be used in practical applications and as sources of benchmark results for testing alternative numerical techniques.

5.13 Superposition *T*-matrix code for randomly oriented two-sphere clusters

The World Wide Web site http://www.giss.nasa.gov/~crmim provides access to a superposition *T*-matrix code for computing the far-field scattering characteristics of a monodisperse two-sphere cluster (bisphere) in random orientation, as described in Section 5.9. The component spheres can be identical or different in terms of their size and relative refractive index and can be touching or separated. The *T* matrices of the component spheres are diagonal, the diagonal elements being the respective Lorenz–Mie coefficients (Eqs. (5.42)–(5.44)). The cluster *T* matrix is expanded about the geometrical center of the cluster (i.e., the center of the smallest sphere that encloses the cluster) and is diagonalized by means of directing the *z*-axis of the particle coordinate system along the line connecting the component sphere centers. The $\mathbf{T}_m$ blocks are computed sequentially for $m = 0, 1, ..., n_{\max}(1)$, where $n_{\max}(1)$ is the maximal order of numerically significant Lorenz–Mie coefficients for the larger sphere. $n_{\max}(1)$ and $n_{\max}(2)$ for the larger and the smaller sphere, respectively, are computed as (cf. Eq. (5.237))

$$n_{\max}(i) = x_i + 4.05x_i^{1/3} + \mathrm{NODR1}, \qquad i = 1, 2, \tag{5.285}$$

where x_i is the size parameter of sphere i and NODR1 is an input integer parameter (see below). The code does not check convergence over the parameter $n_{\max}$ specifying the size of the cluster T matrix (subsection 5.8.4) but rather uses an *a priori* estimate computed from

$$n_{\max} = x_{12} + 4.05x_{12}^{1/3} + \text{NODRT1}, \tag{5.286}$$

where $x_{12} = 2\pi r_{12}/\lambda_1$, r_{12} is the distance between the centers of the component spheres, and NODRT1 is another input integer parameter.

The code has the following *input* parameters.

LAM:
$\text{LAM} = \lambda_1$ is the wavelength of the incident light in the surrounding medium.

R, N, and K:
$\text{R(I)} = r_i$, $\text{N(I)} = \text{Re}\, m_i$, and $\text{K(I)} = \text{Im}\, m_i$ are the radius and the real and imaginary parts of the relative refractive index, respectively, for sphere i (i = 1, 2). K must be non-negative. If the spheres are of unequal size, the larger sphere must be number 1 and the smaller must be number 2.

R12:
$\text{R12} = r_{12}$ is the distance between component sphere centers. In general, R12 ≥ R(1) + R(2). Touching spheres have R12 = R(1) + R(2).

NODR1 and NODRT1:
NODR1 and NODRT1 are integers entering Eqs. (5.285) and (5.286). Usually NODR1 = 2 and NODRT1 = 2 provide acceptable accuracy. However, we recommend occasional checks of convergence of the solution over these parameters.

NPNA:
NPNA is the number of scattering angles at which the scattering matrix is computed. The corresponding scattering angles are given by 180*(I–1)/(NPNA–1) (in degrees), where I = 1, …, NPNA numbers the angles. This way of choosing scattering angles can be readily changed in the subroutine MATR (see subsection 5.10.2).

The code provides the following *output* information.

CEXT and CSCA:
$\text{CEXT} = \langle C_{\text{ext}} \rangle$ and $\text{CSCA} = \langle C_{\text{sca}} \rangle$ are the orientation-averaged extinction and scattering cross sections, respectively.

< COS > and W:
$\text{< COS >} = \langle \cos\Theta \rangle$ and $\text{W} = \varpi$ are the orientation-averaged asymmetry parameter and single-scattering albedo, respectively.

ALPHA1, …, BETA2:
ALPHA1(S) = α_1^s, ALPHA2(S) = α_2^s, ALPHA3(S) = α_3^s, ALPHA4(S) = α_4^s, BETA1(S) = β_1^s, and BETA2(S) = β_2^s are the coefficients appearing in expansions (4.75)–(4.80).

F11, F22, F33, F44, F12, and F34:
F11 = a_1, F22 = a_2, F33 = a_3, F44 = a_4, F12 = b_1, and F34 = b_2 are the elements of the normalized Stokes scattering matrix (4.51).

The input parameters LAM, R(1), R(2), and R12 must be specified in the same units of length. If they are specified, for example, in micrometers then the extinction and scattering cross sections generated by the code are given in square micrometers. The general physical correctness of the numerical results is tested using inequalities derived by van der Mee and Hovenier (1990). The correctness and expected accuracy of the code is also demonstrated by the following additional tests (Mishchenko and Mackowski 1996).

(1) *T*-matrix computations for a bisphere with components of different size converge to the regular Lorenz–Mie solution for the bigger component as the size of the smaller component approaches zero.

(2) *T*-matrix computations for a bisphere with increasing distance between identical components converges to the Lorenz–Mie solution for independent spheres. The only exception is the direction of exact forward scattering, where the interference of light singly scattered by the bisphere components is constructive for any bisphere orientation and nearly doubles the height of the forward-scattering phase function peak as compared to that of a single sphere (Mishchenko *et al.* 1995).

(3) The computation of the *T* matrix for a bisphere in the particle coordinate system with the *z*-axis connecting the component sphere centers requires specification of the size parameters of the upper and lower components. If the size parameters are different then one has a choice of assigning the larger size parameter to the upper or to the lower sphere. However, the scattering results for randomly oriented bispheres must be independent of the choice, and, indeed, the code produces the same results whatever the choice is. Similarly, bisphere components can have different relative refractive indices, and, as expected, the code produces results that do not depend on assigning a particular relative refractive index to the upper or to the lower component.

(4) For nonabsorbing particles (i.e., particles for which the imaginary part of the relative refractive index is equal to zero) the scattering and extinction cross sections must be equal. The code reproduces this equality with very high accuracy.

(5) The accuracy of computing the bisphere *T* matrix was tested by using the numerical data for a fixed bisphere orientation reported by Flatau *et al.* (1993), who computed the scattered field without computing the *T* matrix. Agreement of up to four significant digits was found.

(6) Analytical *T*-matrix computations of the phase function and the degree of linear

polarization for randomly oriented bispheres with touching and separated components show agreement of up to three significant digits with the calculations of Tishkovets (1994), who employed the standard orientation-averaging method based on numerical angle integrations.

These tests indicate that the superposition *T*-matrix code is capable of producing very accurate numerical results. Mishchenko and Mackowski (1996) used the code to tabulate benchmark results for the following two models:

- monodisperse, randomly oriented bispheres, with touching identical components having size parameter 10;
- monodisperse, randomly oriented bispheres, with identical separated components having the size parameter 5. The distance between the sphere centers is twice their diameter.

The relative refractive index for both models is 1.5 + i0.005.

Further reading

Bohren (1974) and He and Cao (1998) developed analytical solutions for electromagnetic scattering by optically active (chiral) and bi-isotropic spheres, respectively. The computation of the Lorenz–Mie coefficients for concentric core–mantle spheres was considered by Kerker (1969), Toon and Ackerman (1981), Fuller (1993), and Kaiser and Schweiger (1993). Mikulski and Murphy (1963), Wait (1963), Bhandari (1985), and Mackowski *et al.* (1990) developed (recursive) algorithms for concentric multilayered spheres, whereas Wyatt (1962) and Perelman (1996) studied the problem of scattering by inhomogeneous spheres with a radially symmetric distribution of the refractive index. The scattering and absorption of light by a sphere imbedded in an absorbing host medium have been discussed by Chýlek (1977), Bohren and Gilra (1979), Bruscaglioni *et al.* (1993), Quinten and Rostalski (1996), Lebedev *et al.* (1999), Fu and Sun (2001), and Sudiarta and Chýlek (2001). Gouesbet *et al.* (1991) developed a so-called generalized Lorenz–Mie theory describing the scattering of an arbitrarily shaped incident beam by an arbitrarily located homogeneous spherical particle. The special case of a focused Gaussian beam has been considered, among others, by Gouesbet *et al.* (1988), Barton *et al.* (1989), and Lock (1995).

An interesting method for computing the *T* matrix for spheroids was developed by Schulz *et al.* (1998a). They first derived the *T* matrix in spheroidal coordinates using the separation of variables method and then converted it into the regular *T* matrix in spherical coordinates. Mishchenko and Videen (1999) reported the results of EBCM computations of electromagnetic scattering by randomly oriented osculating spheres. Kahnert *et al.* (2001a, b) have developed an efficient EBCM algorithm for computing the scattering and absorption properties of finite polyhedral cylinders.

Tsang *et al.* (1992), Zurk *et al.* (1995, 1996), and Siqueira and Sarabandi (2000) used the superposition *T*-matrix method to compute the extinction rate, effective permittivity, and scattering properties of media composed of densely packed, randomly positioned spheres. A modified version of the superposition *T*-matrix approach has been applied to

the problem of electromagnetic scattering by a particle or a cluster of particles located above or below (with respect to the incident wave) a plane interface separating two homogeneous half-spaces with different refractive indices. We refer the reader to the pioneering paper by Kristensson (1980) and recent publications by Videen (1996), Wriedt and Doicu (1998b), Denti *et al.* (1999a, b), Doicu *et al.* (1999), and Moreno and González (2000), where further literature citations can be found. Mackowski (2001) developed an approximate method to compute the T matrix for large-scale clusters of spheres by combining the superposition T-matrix method and an effective medium theory (see also Botet *et al.* 1997). He showed that this approximation can provide accurate predictions of the scattering and absorption properties of clusters containing a large number of uniformly packed spheres using only a fraction of the computer time required for the exact solution. Hamid (1996) and Saija *et al.* (2001) simulated electromagnetic scattering by spheroids and hexagonal cylinders by applying the superposition T-matrix method to clusters of appropriately arranged small spheres.

Appendix B of Bohren and Huffman (1983) contains a FORTRAN code for computing the Lorenz–Mie coefficients for a concentric core–mantle sphere and discusses its range of applicability. Additional codes for multilayered spheres are listed in Flatau (2000) and Wriedt (2000). The World Wide Web site ftp://ftp.eng.auburn.edu/pub/dmckwski/scatcodes/index.html provides access to two multi-sphere superposition T-matrix codes. The code SCSMFO is designed to calculate the Stokes scattering matrix and optical cross sections for a large-scale sphere cluster in a fixed orientation relative to the incident plane wave. On-line documentation provides the formulation and description of the code and a sample data input file. The code SCSMTM calculates the T matrix of a sphere cluster and the orientation-averaged scattering matrix and optical cross sections, as described by Mackowski and Mishchenko (1996). The on-line directories created and maintained by Wriedt (2000) and Flatau (2000) provide links to several Lorenz–Mie codes for homogeneous and concentrically layered spheres, single-particle EBCM codes, and superposition T-matrix codes for aggregated spheres and spheres with asymmetrically located spherical inclusions.

Numerous practical applications of the T-matrix method have been reviewed by Mishchenko *et al.* (1996b, 2000d). Further applications to biophysics, geophysics, astrophysics, and particle characterization can be found in the monographs by Lopatin and Sid'ko (1988) and Borghese *et al*. (2003) and papers by Quirantes and Delgado (1995), Borrmann *et al.* (1996, 2000), Doicu *et al.* (1997, 1998), Astafieva and Babenko (1999), Aydin and Walsh (1999), Bantges *et al.* (1999), Czekala *et al.* (1999, 2001), Ding and Xu (1999), Francis *et al.* (1999), Kouzoubov *et al.* (1999), Krotkov *et al.* (1999), Liu *et al.* (1999), Petrova (1999), Porstendorfer *et al.* (1999), Prodi *et al.* (1999), Ruppin (1999), Stubenrauch *et al.* (1999), Tsias *et al.* (1999), Vermeulen (1999), Volten *et al.* (1999), Wirth *et al.* (1999), Carey *et al.* (2000), Gledhill and McCall (2000), Hogan *et al.* (2000), Petrova *et al.* (2000), Reichardt *et al.* (2000a), Shvalov *et al.* (2000), Voshchinnikov *et al.* (2000), Zrnić *et al.* (2000), Alpers *et al.* (2001), Keenan *et al.* (2001), Kerola and Larson (2001), Prigent *et al.* (2001), and Vargas and Niklasson (2001). Nieminen *et al.* (2001) used the T-matrix method to compute laser trapping forces on a glass spheroid immersed in water.

A comprehensive list of peer-reviewed T-matrix publications was compiled by Mishchenko *et al*. (2004b) and is available at http://www.giss.nasa.gov/~crmim/publications.

Chapter 6

Miscellaneous exact techniques

All needs of a practitioner interested in light scattering by spherical particles are served well by the Lorenz–Mie theory, whereas those interested in exact calculations for nonspherical objects must resort to one of the more general and complex solutions. Although exact techniques for computing electromagnetic scattering by nonspherical particles may seem to be innumerable, some of them have been re-derived several times under different names, and most of them belong to one of two broad categories. Differential equation methods compute the scattered field by solving the Maxwell or the vector wave equations, subject to appropriate boundary conditions, in the time domain (Eqs. (1.1)–(1.4)) or in the frequency domain (Eqs. (1.17)–(1.20)). Integral equation methods are based on the volume or surface integral counterparts of the Maxwell equations; the boundary conditions are included in the solution automatically. A third category of methods includes hybrid techniques and methods that can be derived using different approaches.

This chapter briefly reviews several widely used exact theoretical approaches. Because of space limitations, the discussion here is much more concise than that in the previous chapter on the *T*-matrix method and Lorenz–Mie theory. More detailed information on specific numerical techniques can be found in the literature cited. In most cases we mention a recent review or a monograph providing further references. A general updated source of information on electromagnetic scattering techniques for nonspherical particles is the recent book edited by Mishchenko *et al.* (2000a).

Most theoretical methods yield the scattered electric field for a single particle in a fixed orientation, whereas practical applications often require the knowledge of size-, shape-, and orientation-averaged quantities such as the optical cross sections and phase and scattering matrix elements. Therefore, we will specifically indicate how ensemble averaging affects the performance of a technique. Since conventional ver-

sions of many techniques are applicable only to homogeneous, isotropic, optically inactive particles, we will mention explicitly possible extensions to inhomogeneous, anisotropic, and/or chiral scatterers. We will not discuss specifically theoretical techniques for such peculiar two-dimensional scatterers as infinite cylinders because our interest is in three-dimensional scattering by finite objects.

In what follows, scattering particles will be often characterized by: (i) the size parameter $x = 2\pi a/\lambda_1$, where a is a characteristic particle size (e.g., the semi-major dimension or the radius of a surface- or volume-equivalent sphere) and λ_1 is the wavelength of the incident light in the surrounding medium; (ii) the aspect ratio ε, which is the ratio of the maximum to minimum particle dimensions; and (iii) the index of refraction m relative to the surrounding medium. The efficiency of a numerical technique will be described usually in terms of its computational complexity, i.e., the dependence of the number of computer operations on the particle size parameter. It should be realized, however, that although the computational complexity of two different techniques can be proportional to the same power of the size parameter, the respective proportionality factors can be quite different, thereby making one technique much slower than the other.

6.1 Separation of variables method for spheroids

The separation of variables method (SVM) for single, homogeneous, isotropic spheroids was pioneered by Oguchi (1973), Asano and Yamamoto (1975), and Sinha and MacPhie (1977). With this method, the electromagnetic scattering problem is solved for a prolate or an oblate spheroid in the respective spheroidal coordinate system by expanding the incident, internal, and scattered fields in vector spheroidal wave functions (Flammer 1957). The expansion coefficients of the incident field are computed analytically, whereas the unknown expansion coefficients of the internal and scattered fields are determined through the requirement of continuity of the tangential electric and magnetic field components on the spheroid boundary (Eqs. (1.13) and (1.15)). Because the vector spheroidal wave functions are not orthogonal on the spheroidal surface, this procedure results in an infinite set of linear algebraic equations for the unknown expansion coefficients, which must be truncated and solved numerically. Farafonov (1983) (see also Voshchinnikov and Farafonov 1993) developed a version of the SVM in which one finds separately the axisymmetric part of the solution (i.e., the part independent of the azimuthal angle) and the non-axisymmetric part of the solution and uses a modified set of expansion functions.

For spheroids significantly larger than a wavelength and/or for large relative refractive indices, the system of linear equations becomes large and ill-conditioned. Furthermore, the computation of the vector spheroidal wave functions is a difficult mathematical and numerical problem, especially for absorbing particles (i.e., those with non-zero imaginary part of the relative refractive index). These factors have

limited the applicability of the SVM to equivalent-sphere size parameters less than about 40. Another obvious limitation of the technique is that it is applicable only to spheroidal scatterers. The main advantage of the SVM is that it can produce very accurate results. Furthermore, the version of the SVM developed by Farafonov provides numerically stable results for spheroids with extreme aspect ratios. The computational complexity of the SVM is $O(x^3)-O(x^4)$.

Various improvements of the SVM have been discussed by Asano (1979), Kurtz and Salib (1993), Do-Nhat and MacPhie (1997), Li *et al.* (1998a, 2001), Eide *et al.* (1999), and Qingan *et al.* (1999). The SVM has been extended to core–mantle spheroids by Onaka (1980), Cooray and Ciric (1992), Sebak and Sinha (1992), and Farafonov *et al.* (1996) (see also Gurwich *et al.* 2000), and to optically active spheroids by Cooray and Ciric (1993). Schulz *et al.* (1998a) developed an analytical technique for computing electromagnetic scattering by an ensemble of randomly oriented spheroids. They first used the Asano and Yamamoto version of the SVM to compute the T matrix in the spheroidal coordinate system, then converted it into a T matrix in the spherical coordinate system, and finally used the orientation-averaging approach described in Chapter 5. SVM computations for homogeneous and core–mantle spheroids have been reported by Asano (1979, 1983), Rogers and Martin (1979), Asano and Sato (1980), Schaefer (1980), de Haan (1987), Stammes (1989), Voshchinnikov and Farafonov (1994), Kim and Martin (1995), Somsikov (1996), Voshchinnikov (1996), Il'in and Voshchinnikov (1998), Li *et al.* (1998b), Schulz *et al.* (1998b, 1999b), Ciric and Cooray (1999), Eide *et al.* (2000), Kang *et al.* (2000), and Voshchinnikov *et al.* (2000). Available SVM computer codes are listed in Flatau (2000) and Wriedt (2000). An extensive review of the SVM is provided by Ciric and Cooray (2000).

6.2 Finite-element method

The finite-element method (FEM) is a differential equation technique that computes the scattered time-harmonic electric field by solving numerically the vector Helmholtz equation subject to the standard boundary conditions (Morgan and Mei 1979; Silvester and Ferrari 1996). The particle is imbedded in a finite computational domain that is discretized into many small-volume cells called elements, with about 10 to 20 elements per wavelength. The electric field values are specified at the nodes of these elements and are initially unknown. Through the requirement of the boundary conditions, the differential equation is converted into a matrix equation for the unknown node electric field values. This equation is solved using, e.g., standard Gaussian elimination (GE) or one of the preconditioned iterative methods such as the conjugate gradient method (CGM). Because of the local nature of the differential equation, electric fields at the nodes are directly related only to their neighbors, thereby making the resultant matrix equation sparse and banded, which significantly reduces

the numerical effort. The computational complexity of the FEM with sparse GE is $O(x^7)$, whereas that of the FEM with the CGM is only $O(x^4)$. The disadvantage of the FEM with the CGM is that computations must be repeated for each new direction of incidence, but the number of requisite incidence directions may be reduced by exploiting symmetries of the scattering problem and the reciprocity relation.

Although scattering in the far-field zone is an unbounded-space problem, the FEM must be implemented always in a finite computational domain in order to limit the number of unknowns to a manageable size. As a consequence, approximate absorbing boundary conditions must be imposed at the outer boundary of the computational domain in order to suppress wave reflections back into the domain and permit the numerical analogs of the outward-propagating waves to exit the domain almost as it were infinite (Mittra and Ramahi 1990). Another approach (e.g., Volakis *et al.* 1998; Sheng *et al.* 1998) is to couple the FEM with a surface integral equation in order to satisfy accurately the radiation condition at infinity (i.e., to ensure the $1/r$ decay of the transverse component and a faster than $1/r$ decay of the radial component of the scattered electric field in the far-field zone; see Section 2.2). The drawback of the latter technique is that it can destroy the sparsity of the finite-element matrix.

Another way of enforcing the radiation condition is the so-called unimoment method (Mei 1974; Morgan and Mei 1979; Morgan 1980). This modification of the FEM uses a spherical computational domain and an expansion of the scattered field outside the computational domain in outgoing spherical wave functions with unknown coefficients. The total external field is the sum of this unknown expansion and the known expansion of the incident field. The unknown expansion coefficients are found by applying the FEM scheme inside the computational domain and matching the FEM nodal fields and the spherical wave function expansions at the boundary of the computational domain. The scattered field in the far-field zone is calculated by evaluating the spherical wave function expansion and automatically satisfies the radiation condition. Since the unimoment method always uses a spherical computational domain, the volume of the domain can become much larger than the volume of the scatterer for objects with high aspect ratios, thereby making this technique inefficient.

The important advantages of the FEM are that it can be applied to arbitrarily shaped and inhomogeneous particles, is simple in concept and implementation, and avoids the singular-kernel problem typical of integral equation methods (see Section 6.5). However, FEM computations are spread over the entire computational domain rather than confined to the scatterer itself as in the integral equation methods. This tends to make FEM calculations rather time consuming and limits the maximum size parameter to values less than about 10. Features such as the finite spatial discretization and approximate absorbing boundary condition make the FEM unsuitable for applications in which achieving a very high and controllable numerical accuracy is important. Further information about the FEM and the closely related finite-difference method (FDM) can be found in Morgan (1990), Silvester and Ferrari

(1996), and Volakis *et al.* (1998). Several FEM computer codes are listed in Wriedt (2000).

6.3 Finite-difference time-domain method

Unlike the FEM, the finite-difference time-domain method (FDTDM) calculates electromagnetic scattering in the time domain by solving Maxwell's time-dependent curl equations (1.2) and (1.4) directly (Yee 1966). The space and time derivatives of the electric and magnetic fields are approximated using a finite-difference scheme with space and time discretizations selected to constrain computational errors and ensure numerical stability of the algorithm. Hence, time is approximated by a sequence of discrete steps, and a marching-in-time procedure is used to track the evolution of the fields from their initial values at some initial time. As in the FEM, the scattering object is imbedded in a finite computational domain, and absorbing boundary conditions are employed to model scattering in unbounded space (e.g., Berenger 1996; Grote and Keller 1998; Yang and Liou 1998b; Sun *et al.* 1999). The fields are specified at spatial grid points with discretization density similar to that needed for the FEM. Values at the grid points for the previous and current time steps are used to calculate the values at the next time step, thereby making the system of equations to update the fields fully explicit. As a consequence, there is no need to solve a large system of linear equations, and the memory-size requirement is proportional to the total number of grid points. The common practice of modeling scattering objects with curved boundaries using rectangular grid cells causes a so-called staircasing effect and increases numerical errors. This effect becomes especially pronounced for particles with large relative refractive indices and must be reduced using special techniques (Yang and Liou 1996a; Sun and Fu 2000). The operation count grows approximately as the fourth power of the particle size parameter. Since the FDTDM computes the near field in the time domain, a special near-zone to far-zone transformation must be invoked in order to compute the scattered far field in the frequency domain (Taflove 1995; Yang and Liou 1996a; Martin 1998).

The FDTDM has become rather popular recently, owing to its conceptual simplicity, flexibility, and ease of implementation. Since the method tracks the time-varying field throughout a volume of space, FDTDM results are well suited for animation using modern computer graphics so that the user is provided with a visual demonstration of the temporal and spatial behavior of the electromagnetic field. The FDTDM shares the advantages of the FEM with the CGM as well as its limitations in terms of accuracy, computational complexity, size parameter range, and the need to repeat all computations with changing direction of illumination. Applications of the FDTDM to far-field scattering computations have been described by Tang and Aydin (1995), Aydin and Tang (1997a, b), Yang *et al.* (1997, 2000b), Liou *et al.* (1998, 2000), Videen *et al.* (1998b), Aydin and Walsh (1999), Drezek *et al.* (1999), and Fu

et al. (1999). Additional information on the FDTDM can be found in the monographs by Kunz and Luebbers (1993) and Taflove (1995, 1998) and in the recent review by Yang and Liou (2000). Available FDTDM computer codes are listed by Wriedt (2000).

6.4 Point-matching method

The point-matching method (PMM) is a differential equation technique based on expanding the incident and internal fields in vector spherical wave functions that are regular at the origin and expanding the scattered field outside the scatterer in outgoing vector spherical wave functions. The expansion coefficients of the incident field are known (Eqs. (5.4) and (5.5)), whereas the expansion coefficients of the internal and scattered fields are found by truncating the expansions to a finite size and matching the fields at the surface of the scatterer via application of the boundary conditions. In the simple PMM, the fields are matched at as many points on the surface as there exist unknown expansion coefficients (Oguchi 1973).

The general idea of the PMM is so simple and attractive that the method continues to be reinvented (e.g., Sarkar and Halas 1997). However, it often produces poorly converging and unstable results. It is possible that such behavior may be attributed to the fact that it relies on the Rayleigh hypothesis (RH; see Section 5.1), whereas the validity of this hypothesis is questionable. For example, the results of Doicu *et al.* (1999), Ngo *et al.* (1997), and Mishchenko and Videen (1999) seem to imply that the RH may in fact be wrong.

The use of vector spherical wave functions to represent the incident, internal, and scattered fields makes the PMM similar to the *T*-matrix method. Moreover, it appears that the RH can be used to derive the extended boundary condition method (EBCM); see Chew (1995). Since the EBCM is exact, this derivation has been interpreted sometimes as evidence of the validity of the RH and of the equivalence of the RH and the EBCM (Burrows 1969; Schmidt *et al.* 1998). However, the fact that the EBCM can be derived from the RH means only that the RH is a sufficient condition of validity of the EBCM but not a necessary condition. The equivalence of the RH and the EBCM and hence the validity of the RH would follow only from reciprocal derivation of the RH from the EBCM, but this has not been accomplished so far. Therefore, one should not exclude the possibility that the RH may be violated despite the fact that the EBCM is exact (Millar 1969; Lewin 1970).

A modification of the PMM called the boundary-matching method was developed by Barton and Alexander (1991). Instead of imposing the boundary conditions at a finite number of distributed points, the boundary condition equations are expanded in spherical harmonics and matched for each angular mode. This results in a set of simultaneous algebraic equations from which the expansion coefficients can be determined. Since the method shows poor convergence for spheroids with aspect ratios

larger than 1.4, Barton and Alexander concluded that it is best suited to the analysis of near-spherical particles.

The convergence problem of the simple PMM appears to be partly ameliorated in the generalized PMM (GPMM) by the creation of an overdetermined system of equations for the unknown expansion coefficients. This is accomplished by matching the fields in the least squares sense at a number of surface points significantly greater than the number of unknowns (Morrison and Cross 1974; Oguchi and Hosoya 1974; Al-Rizzo and Tranquilla 1995a, b). The performance of the GPMM has been further improved by employing multiple spherical expansions to describe the fields both inside and outside the scattering object (Joo and Iskander 1990; Al-Rizzo and Tranquilla 1995c). This multiple-expansion GPMM (ME-GPMM) does not rely on the RH; it is also known as the generalized multipole technique, the discrete sources method, and the Yasuura method (Hafner 1990; Ludwig 1991; Eremin and Orlov 1998; Wriedt 1999). It is claimed that the ME-GPMM for rotationally symmetric scatterers is numerically stable, sufficiently accurate, and applicable to large size parameters (Al-Rizzo and Tranquilla 1995c). Piller and Martin (1998a) extended the ME-GPMM to anisotropic scatterers.

6.5 Integral equation methods

The interaction of a plane electromagnetic wave with an object of volume V_{INT} is described fully by the volume integral equation (2.16). The calculation of the scattered field using Eq. (2.16) would be straightforward except that the internal electric field is unknown. Therefore, this equation must first be solved for the internal field. The integral in Eq. (2.16) is usually approximated by discretizing the interior region into N small cubic cells of a volume ΔV with about 10 to 30 cells per wavelength and assuming that the electric field and the refractive index within each cell are constant:

$$\mathbf{E}(\mathbf{r}_i) = \mathbf{E}^{\mathrm{inc}}(\mathbf{r}_i) + k_1^2 \Delta V \sum_{j=1}^{N} \ddot{G}(\mathbf{r}_i, \mathbf{r}_j) \cdot \mathbf{E}(\mathbf{r}_j)[m^2(\mathbf{r}_j) - 1], \quad i = 1, ..., N, \tag{6.1}$$

where $\mathbf{r}_i \in V_{\mathrm{INT}}$ is the central point of the ith cell. Physically this procedure is equivalent to representing the internal field at each point of the interior region V_{INT} as a sum of the incident field and the field induced by sources at all interior points, including the self point. Equations (6.1) form a system of N linear algebraic equations for the N unknown internal fields $\mathbf{E}(\mathbf{r}_i)$ and must be solved numerically. Since the internal fields interact with each other throughout the object, the resultant matrix is full. Once the internal fields are found, the total external field is determined from

$$\mathbf{E}(\mathbf{r}) = \mathbf{E}^{\mathrm{inc}}(\mathbf{r}) + k_1^2 \Delta V \sum_{j=1}^{N} \ddot{G}(\mathbf{r}, \mathbf{r}_j) \cdot \mathbf{E}(\mathbf{r}_j)[m^2(\mathbf{r}_j) - 1], \quad \mathbf{r} \in V_{\mathrm{EXT}}. \tag{6.2}$$

Finally, the scattered field is computed by subtracting the incident field from the total external field. This version of the volume integral equation method (VIEM) is known as the method of moments (MOM). Since the free space dyadic Green's function given by Eqs. (2.13) and (2.15) becomes singular as $|\mathbf{r}-\mathbf{r}'|\to 0$, special techniques must be used to handle the self-interaction term $(j=i)$ in the sum on the right-hand side of Eq. (6.1) (Lakhtakia and Mulholland 1993).

Several modifications of the MOM have been developed under different names: the digitized Green's function algorithm (Goedecke and O'Brien 1988), the volume integral equation formulation (Iskander *et al.* 1989a; Hage *et al.* 1991; Lumme and Rahola 1998), and the variational volume integral equation method (Peltoniemi 1996). The main difference among these techniques is the way in which they treat the self-interaction term.

The straightforward approach to solving the MOM matrix equation using the standard GE entails a computational complexity of $O(N^3)\propto O(x^9)$ and is not practical for size parameters exceeding unity. The conjugate or bi-conjugate gradient method together with the fast Fourier transform (CGM-FFT or BCGM-FFT) (Gan and Chew 1995; Peterson *et al.* 1998, Chapter 4) has the computational complexity $O(N^{1+\alpha}\log N)\propto O(x^{3+3\alpha}\log x)$, where N^α with $0<\alpha<1$ is the total number of iterations required to achieve a specific accuracy; this method can be applied to significantly larger size parameters. Furthermore, the CGM-FFT (BCGM-FFT) and related techniques can significantly reduce computer memory requirements. The standard drawback of using the CGM (BCGM) and other preconditioned iterative techniques is that computations must be fully repeated for each new illumination direction.

Another version of the VIEM is the so-called discrete dipole approximation (DDA), otherwise known as the coupled dipole method. Whereas the MOM deals with the *actual* electric fields in the central points of the cells constituting the scattering object (Eq. (6.1)), the DDA exploits the concept of *exciting* field. It is based on partitioning a particle into a number N of elementary polarizable units called dipoles. The electromagnetic response of the dipoles to the local electric field is assumed to be known. The field exciting a dipole is a superposition of the external field and the fields scattered by all other dipoles. This allows one to write a system of N linear equations for N fields exciting the N dipoles. An important way in which the DDA matrix equation differs from the MOM matrix equation is that the former does not contain the troublesome self-interaction term. The numerical solution of the DDA matrix equation is then used to compute the N partial fields scattered by the dipoles and thereby the total scattered field. Although the original derivation of the DDA by Purcell and Pennypacker (1973) was heuristic, Lakhtakia and Mulholland (1993) showed that the DDA can in fact be derived from the volume integral equation and is closely related to the MOM.

Since the pioneering paper by Purcell and Pennypacker (1973), the DDA has been improved by modifying the treatment of the dipole polarizability (Draine 1988;

Dungey and Bohren 1991; Draine and Goodman 1993; Lumme and Rahola 1994; Okamoto 1995), including magnetic dipole and dielectric quadrupole terms in addition to the electric dipole term (Mulholland *et al.* 1994; Lemaire 1997), applying the CGM-FFT and other preconditioned iterative methods to solve the DDA matrix equation with a $O(x^{3+3\alpha}\log x)$ computational complexity (Goodman *et al.* 1991; Flatau 1997), and employing concepts of the sampling theory (Piller and Martin 1998b). Varadan *et al.* (1989), Lakhtakia (1992), and Piller (1999) extended the DDA to anisotropic, bi-anisotropic, and high-permittivity materials, respectively. Ku (1993) compared the numerical performance of the MOM (Iskander *et al.* 1989a) and the DDA (Dungey and Bohren 1991). Chiappetta (1980) and Singham and Bohren (1987, 1988) developed a scattering-order formulation of the DDA. Hoekstra *et al.* (1998) investigated the performance of a DDA implementation on a parallel supercomputer. McClain and Ghoul (1986), Singham *et al.* (1986), and Khlebtsov (2001) have developed analytical DDA procedures for computing the scattering of light by randomly oriented particles based on re-expanding Cartesian tensor products in terms of spherical tensor products and exploiting analytical properties of Wigner *D*-functions (Appendix B). Unfortunately, this approach involves a time-consuming matrix inversion (computational complexity $O(x^9)$) and is applicable only to particles smaller than a wavelength. Draine and Weingartner (1996) and Kimura and Mann (1998) used the DDA to compute the radiation force and torque on nonspherical particles and fluffy aggregates. Hoekstra *et al.* (2000) extended their work by deriving DDA formulas for computing the radiation force experienced by each dipole.

The major advantages of the MOM and DDA are that they automatically satisfy the radiation condition at infinity (Eq. (2.24)), are confined to the scatterer itself, thereby resulting in fewer unknowns than the differential equation methods, and can be applied to inhomogeneous, anisotropic, and/or optically active scatterers (e.g., Su 1989; Rojas 1992). However, the numerical accuracy of the methods is relatively low, especially for the scattering matrix elements, and improves slowly with increasing N, whereas the computer time grows rapidly with increasing size parameter (Singham 1989; Draine and Flatau 1994; Evans and Stephens 1995; Okamoto *et al.* 1995). A major source of numerical errors is the approximate representation of smooth particle surfaces by discrete cubical dipoles (Lemke *et al.* 1998). Another disadvantage of the above techniques is the need to repeat the entire calculation for each new direction of incidence (for the MOM and DDA with the CGM-FFT). These factors have made MOM and DDA computations time consuming, especially for particle size, shape, and/or orientation distributions, and have limited the particle size parameter to relatively small values.

The attractiveness and simplicity of the physical idea of the DDA and the public availability of the well-documented DDA code by Draine and Flatau (1997) have resulted in widespread applications of this technique during the last decade. Further information on the MOM and DDA and their applications can be found in Miller *et al.* (1991), Wang (1991), Draine and Flatau (1994), Lumme *et al.* (1997), Lemke and

Quante (1999), Murayama *et al.* (1999), and Draine (2000).

Equation (2.16) is a Fredholm-type integral equation with a singular kernel at $\mathbf{r}' = \mathbf{r}$. Holt *et al.* (1978) removed the singularity by applying the Fourier transform to the internal field and converting the volume integral into an integral in wave number coordinate space. Discretization of the latter results in a matrix equation that is solved numerically and gives the scattered field.

The scattered field obtained with this Fredholm integral equation method (FIEM) satisfies a variational principle and is claimed to be numerically stable and convergent to the exact result, even for particles with large aspect ratios, albeit the size parameter in actual computations for highly aspherical scatterers has been relatively small so far. Numerical implementation of the technique becomes much simpler for homogeneous, rotationally symmetric bodies.

The major limitation of the FIEM is that the matrix elements must be evaluated analytically, thereby requiring different programs for each type of scatterer. As a consequence, FIEM computations have been limited to only a few model shapes such as spheroids, triaxial ellipsoids, and finite circular cylinders (Evans and Holt 1977; Holt *et al.* 1978; Holt and Shepherd 1979; Shepherd and Holt 1983; Matsumura and Seki 1991, 1996). The majority of reported FIEM results pertain to size parameters smaller than 5 and tend to be rather time consuming (Holt 1982). Larger particles (volume-equivalent-sphere size parameters up to 36.7) were considered by Stamatakos *et al.* (1997). However, the relative refractive index was restricted to 1.04, and a comparison of FIEM results for a sphere with exact Lorenz–Mie computations showed poor agreement at scattering angles exceeding $25°$.

An important advantage of the FIEM is that a significant part of the calculation, the integrals, depends only on the particle size parameter and shape. Therefore, changing the relative refractive index and/or the direction and polarization state of the incident wave does not require a complete new calculation. A similar saving of computer time is achieved in performing convergence checks. Papadakis *et al.* (1990) and Karonis *et al.* (1999) extended the FIEM to anisotropic and chiral dielectric ellipsoids, while Stamatakos and Uzunoglu (1997) applied the FIEM to scattering by a linear chain of triaxial dielectric ellipsoids.

Electromagnetic scattering by homogeneous or layered dielectric bodies can be computed using a surface integral counterpart of Eq. (2.16) (Poggio and Miller 1973; Umashankar *et al.* 1986; Medgyesi-Mitschang *et al.* 1994; Swatek and Ciric 2000a, b). Although surface integral equation methods (SIEMs) cannot be applied to highly inhomogeneous scatterers, their important advantage is that the dimensionality of the problem is reduced by one, and the number of unknowns N is proportional to x^2 rather than to x^3, as in the VIEM, thereby resulting in a computational complexity of $O(x^6)$ for SIEMs with the GE and $O(x^{4+2\alpha})$ for SIEMs with the CGM.

6.6 Superposition method for compounded spheres and spheroids

The separation of variables solution for a single sphere (the Lorenz–Mie theory) can be extended to clusters of spheres by using the translation addition theorem for vector spherical wave functions (Bruning and Lo 1971a, b; Borghese *et al.* 1979; Hamid *et al.* 1990; Fuller 1991; Mackowski 1991). The total field scattered by a multi-sphere cluster can be represented as a superposition of individual fields scattered from each sphere. These individual fields are interdependent because of electromagnetic interactions between the component spheres. The external electric field illuminating the cluster and the individual fields scattered by the component spheres are expanded in vector spherical wave functions with origins at the individual sphere centers. To exploit the orthogonality of the vector spherical wave functions in the sphere boundary conditions, one uses the translation addition theorem with a vector spherical wave function centered at one sphere origin then re-expanded about another sphere origin (Appendix C). This procedure ultimately results in a matrix equation for the scattered-field expansion coefficients of each sphere. Numerical solution of this equation for the specific direction and polarization state of the incident wave gives the individual scattered fields and thereby the total scattered field.

Alternatively, inversion of the cluster matrix equation gives sphere-centered transition matrices that transform the expansion coefficients of the incident wave into the expansion coefficients of the individual scattered fields. The advantage of this approach is that the individual-sphere transition matrices are independent of the direction and polarization state of the incident field. In the far-field region, the individual scattered-field expansions can be transformed into a single expansion centered at a common origin inside the cluster. This procedure gives a matrix that transforms the incident-wave expansion coefficients into the common-origin expansion coefficients of the total scattered field. This matrix is completely equivalent to the cluster T matrix (Borghese *et al.* 1984; Mackowski 1994) and can be used in the analytical averaging of scattering characteristics over cluster orientations, as described in Section 5.9 (Fucile *et al.* 1993, 1995; Mishchenko and Mackowski 1994; Mackowski and Mishchenko 1996). Therefore, the superposition method can also be considered as a particular case of the general T-matrix method for aggregated scatterers (Section 5.9) in which the latter is applied to a cluster of spheres (Peterson and Ström 1973; Mishchenko *et al.* 1996b).

The superposition method has been extended to aggregates of concentrically layered spheres (Hamid *et al.* 1992), to spheres with one or more eccentrically positioned spherical inclusions (Fikioris and Uzunoglu 1979; Borghese *et al.* 1992, 1994; Fuller 1995b; Mackowski and Jones 1995), and to pairs of osculating spheres (Videen *et al.* 1996). Cooray and Ciric (1991) developed a superposition method for a cluster of dielectric spheroids in an arbitrary configuration by combining the SVM solution for individual spheroids with the use of appropriate rotational–translational addition theo-

rems for vector spheroidal wave functions (Cooray and Ciric 1989; see also Nag and Sinha 1995).

The computational complexity of the superposition method strongly depends on the number of components and their size parameters and configuration. Obtaining converged results for a larger number of components usually necessitates smaller values for the component size parameters, and vice versa. The superposition method is especially efficient for linear configurations of spheres, owing to the axial symmetry of such a configuration. Because of the analyticity of its mathematical formulation, this method is capable of producing very accurate results. Fuller and Mackowski (2000) gave a detailed review of the superposition method for compounded spheres, while Ciric and Cooray (2000) reviewed the superposition method for systems of spheroids.

6.7 Comparison of methods, benchmark results, and computer codes

The very existence and use of several exact techniques for computing electromagnetic scattering by nonspherical particles testifies that there is no single universal method that provides the best results in all cases. Depending on the application in hand, one particular technique may prove to be the most appropriate in terms of efficiency, accuracy, and applicability to specific particle parameters. Moreover, it is often difficult to formulate and implement simple and objective criteria for comparing the performance of different numerical techniques in a wide range of applications. Ideally, one should use the same type of computer and consider the same scattering problems using codes written by authors with comparable levels of programming skills. Even in this idealistic situation, however, the specific characteristics of the computer used can favorably enhance the performance of one technique and degrade the efficiency of another. For example, one technique may become especially efficient when implemented on a parallel computer, whereas the performance of another technique may benefit from the availability and efficient organization of double or extended precision computations. Furthermore, direct comparisons of different techniques can face serious organizational problems (e.g., Hovenier *et al.* 1996) and have always been restricted to a few techniques and a few scattering problems (Flatau *et al.* 1993; Cooper *et al.* 1996; Wriedt and Comberg 1998; Comberg and Wriedt 1999; Kimura 2001; Schuh and Wriedt 2001; Baran *et al.* 2001b). Thus, it may be that the actual decision in favor of a specific technique has often been based on indirect semi-quantitative evidence scattered over many publications (e.g., Oguchi 1981; Holt 1982) and/or on the availability of a well-documented public-domain computer code.

The paper by Hovenier *et al.* (1996) is a good example of a concerted effort to compare the accuracy and computer-time requirements of three exact techniques: the SVM for spheroids (Voshchinnikov and Farafonov 1993), the *T*-matrix method

(Mishchenko *et al.* 1996b), and the DDA (Lumme and Rahola 1994). Computations were performed for four rotationally symmetric objects: a prolate and an oblate spheroid each with aspect ratio 2, a circular cylinder with length-to-diameter ratio 2, and a bisphere with equal touching components. All particles had the same relative refractive index $m = 1.5 + \mathrm{i}0.01$ and the same volume-equivalent-sphere size parameter $x_{\mathrm{v}} = 5$. The orientation of the rotation axis of each particle with respect to the laboratory reference frame was specified by the Euler angles $\alpha = 0°$, $\beta = 50°$, and $\gamma = 0°$ (Section 2.4). The particles were illuminated by a plane electromagnetic wave incident in the direction of the positive *z*-axis of the laboratory coordinate system, the scattering directions were confined to the *xz*-halfplane with $x \geq 0$, and the comparison quantity was the phase matrix $\mathbf{Z}(\vartheta^{\mathrm{sca}}, \varphi^{\mathrm{sca}} = 0; \vartheta^{\mathrm{inc}} = 0, \varphi^{\mathrm{inc}} = 0)$ (multiplied by k_1^2, where k_1 is the wave number in the surrounding medium) as a function of the zenith angle of the scattered light $\vartheta^{\mathrm{sca}} \in [0°, 180°]$. Scattering by the prolate and oblate spheroids was computed using all three techniques, whereas that by the cylinder and the bisphere was calculated using only the *T*-matrix method and the DDA. The numbers of dipoles *N* in the DDA representation of the scattering objects were 8320, 8664, 6656, and 8448 for the prolate spheroid, the oblate spheroid, the cylinder, and the bisphere, respectively. For the DDA computations, the final results were averages over four discrete orientations of the dipole arrays about the axis of rotational symmetry; this approach was used to reduce the errors incurred in modeling the smooth rotationally symmetric particles by groups of discrete dipoles.

The comparison showed that the results of the SVM and *T*-matrix computations for the spheroids converged to within nine significant figures. Since these two techniques are completely independent, the excellent agreement is an indication of their superb absolute accuracy. The computer time and memory requirements for these two techniques were also comparable, whereas the DDA computations were more time consuming and less accurate. Figure 6.1 (adapted from Hovenier *et al.* 1996) compares the results of *T*-matrix calculations (solid curves) and DDA calculations (diamonds) of the ratio $-Z_{21}/Z_{11}\,(\%)$ for the four scattering models considered. It is evident that the DDA results deviate noticeably from the *T*-matrix curves, although the general trends and features are reproduced with accuracy perhaps good enough for many practical applications.

The evidence accumulated in the published literature suggests that, besides the Lorenz–Mie theory, the only methods capable of providing very accurate results (to five and more correct significant figures) for particles comparable to and larger than a wavelength are the SVM, the *T*-matrix method, and the superposition method. Each of these techniques incorporates an internal convergence test that provides a good measure of the absolute accuracy (Kuik *et al.* 1992; Hovenier *et al.* 1996). Benchmark results for monodisperse and polydisperse spheroids, finite circular cylinders, Chebyshev particles, and two-sphere clusters in fixed and random orientations have been reported by Mishchenko (1991a, 2000), Kuik *et al.* (1992), Hovenier *et al.* (1996), Mishchenko and Mackowski (1996), Mishchenko *et al.* (1996a), Wielaard *et al.*

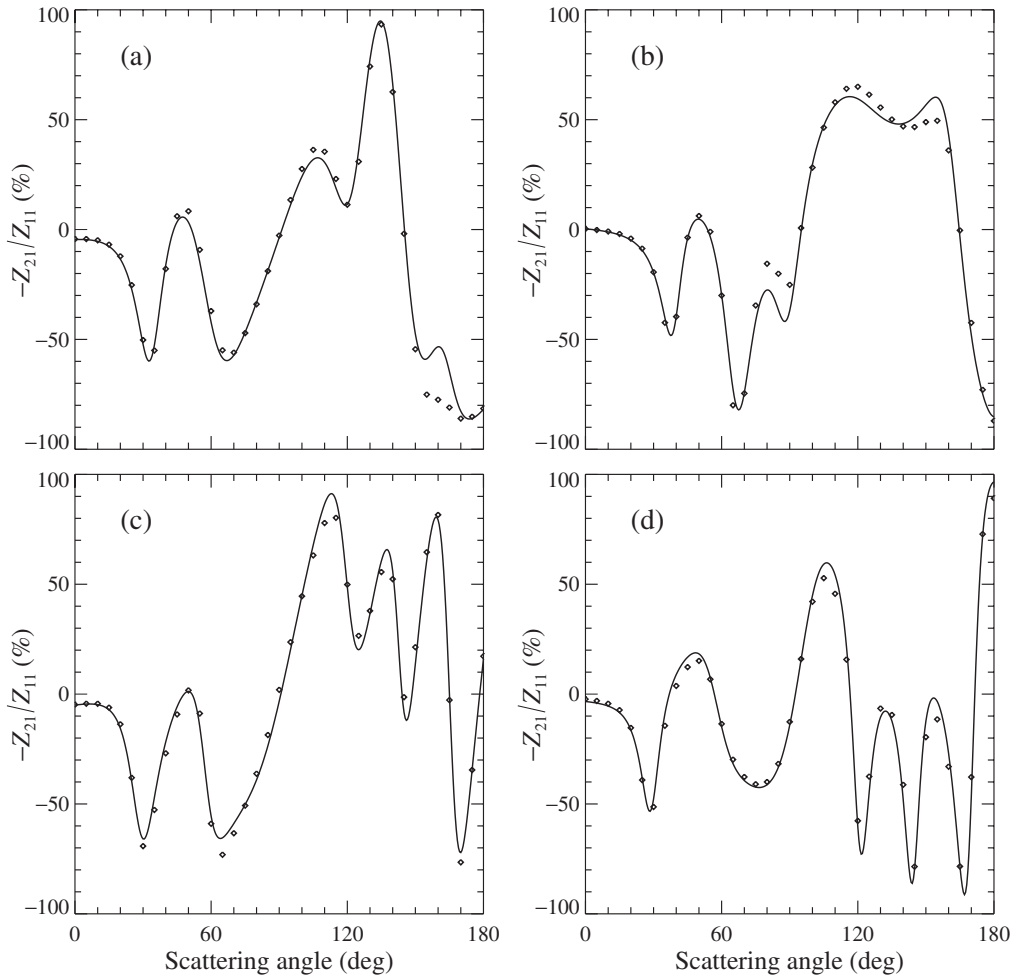

Figure 6.1. The ratio $-Z_{21}/Z_{11}$ as a function of the zenith angle of the scattering direction for (a) a prolate spheroid, (b) an oblate spheroid, (c) a finite circular cylinder, and (d) a bisphere, as specified in the text. The solid curves and the diamonds depict the results of *T*-matrix and DDA computations, respectively.

(1997), and Voshchinnikov *et al.* (2000). Additional benchmark cases were considered in subsection 5.11.7 and Section 5.12. These data cover a wide range of equivalent-sphere size parameters from a few units to 60 (Wielaard *et al.* 1997) and are given correct up to nine significant figures. Since these numbers are accurate to a few units in the last digit, they provide an important tool for testing the accuracy of other exact and approximate theoretical approaches.

The SVM, the *T*-matrix method, the superposition method, the GPMM, and the ME-GPMM are the only techniques that have been used extensively in computations for particles significantly larger than a wavelength. The first three techniques appear to be the most efficient methods for computing electromagnetic scattering by homogeneous and composite objects of revolution (i.e., having rotational symmetry). The availability of the analytical orientation-averaging procedure makes the *T*-matrix

method the fastest technique for randomly oriented symmetric particles (e.g., rotationally symmetric particles, ellipsoids, and polyhedral cylinders) with moderate aspect ratios and also for randomly oriented clusters of spheres. Scattering by particles with larger aspect ratios can be computed with the improved version of the SVM for spheroids developed by Farafonov (1983), the iterative EBCM (cf. subsection 5.8.4), and the ME-GPMM. SIEMs (e.g., Zuffada and Crisp 1997) and the FIEM can also be applied to homogeneous, rotationally symmetric particles with large aspect ratios, although they appear to be slower and less accurate than the other techniques.

Computations for anisotropic objects and homogeneous and inhomogeneous asymmetric particles often may have to rely on more flexible techniques such as the FEM, FDM, FDTDM, MOM, and DDA. All these techniques are simple in concept and computer implementation and appear to have comparable performance characteristics (e.g., Wriedt and Comberg 1998), although often their simplicity and flexibility are accompanied by a loss in efficiency and accuracy and by stronger practical limitations on the maximal particle size parameter. Further effort is obviously required in order to develop improved exact approaches that are both efficient, flexible, and applicable to a wide range of size parameters.

A number of software implementations of the techniques described in this chapter are currently available, and many of them are in the public domain. Extensive lists of available computer codes have been compiled by Flatau (2000) and Wriedt (2000).

Further reading

Farafonov *et al.* (1999) developed a surface integral equation technique for homogeneous rotationally symmetric objects that closely resembles the EBCM but employs a different set of functions to expand the incident, scattered, and internal fields.

Rother and Schmidt (1996) and Rother (1998) developed a differential equation technique called the discretized Mie formalism (DMF), which solves the vector Helmholtz equation for homogeneous scatterers using a method of lines. The main advantage of this method is its analytic incorporation of the radiation condition at infinity. Like many other exact techniques, the DMF becomes much more efficient when the scattering object is rotationally symmetric.

Kattawar *et al.* (1987) found the solution of Eq. (2.16) by first solving a simpler equation for a resolvent kernel matrix. An attractive feature of their approach is that the resolvent kernel matrix is computed only once for the entire range of relative refractive indices.

Vechinski *et al.* (1994) developed a time-domain SIEM to compute the scattering from arbitrarily shaped homogeneous dielectric bodies. The advantage of their technique over the FDTDM is that the radiation condition at infinity is satisfied automatically and the memory requirement is reduced (see also Pocock *et al.* 1998).

Further information on exact scattering methods can be found in the review by Kahnert (2003), in the collection of selected papers edited by Kerker (1988), and in special journal issues edited by Shafai (1991), Barber *et al.* (1994), Hovenier (1996), Lumme (1998), Mishchenko *et al.* (1999a), and Videen *et al.* (2001).

Chapter 7

Approximations

The practical importance of approximate theories of electromagnetic scattering and absorption by small particles diminishes as various exact techniques mature and become applicable to a wider range of problems and as computers become ever more powerful. This is of course especially true of spherical particles, for which the Lorenz–Mie theory can be used to generate accurate numerical results for essentially any size parameter and relative refractive index. Nonetheless, approximate theories still remain a valuable source of physical insight into the processes of scattering and absorption of electromagnetic radiation. Furthermore, it is likely that at least one approximation, the geometrical optics approach, will never become obsolete because its accuracy can only improve as the particle size parameter grows whereas all exact theoretical techniques for nonspherical particles cease to be practical whenever the size parameter exceeds a certain threshold value.

7.1 Rayleigh approximation

Rayleigh (1897) derived an approximation for scattering in the small-particle limit by assuming that the incident field inside and near the particle behaves almost as an electrostatic field and the internal field is homogeneous. Hence the conditions of validity of the Rayleigh approximation (RA) are $x \ll 1$ and $|mx| \ll 1$, where $x = 2\pi a/\lambda_1$, a is the semi-major particle dimension, λ_1 is the wavelength of the incident light in the surrounding medium, and m is the relative refractive index. A detailed account of the RA was given by Kleinman and Senior (1986). A completely analytical solution exists for only a few simple shapes, including triaxial ellipsoids. For general shapes, one must solve numerically a simple integral equation for the polari-

zability tensor. Bohren and Huffman (1983, Chapter 5) gave analytical formulas for the optical cross sections and the scattering matrix elements of randomly oriented spheroids. Note that direct use of the optical theorem (Section 2.8) in the framework of the RA yields only the absorption component of the extinction cross section and must be supplemented by the computation of the scattering cross section via Eq. (2.160).

Kerker *et al.* (1978) and Ku and Felske (1984) compared approximate and exact Lorenz–Mie results for the scattering matrix and the extinction and scattering efficiency factors of small homogeneous spheres and concluded that the range of validity of the RA in terms of the maximal size parameter varied with relative refractive index and scattering angle. Mishchenko (1990b, 1991b) and Voshchinnikov and Farafonov (2000) used the exact T-matrix and the separation of variables methods to analyze the range of validity of RA computations of the extinction matrix and extinction, scattering, and absorption efficiencies for homogeneous spheres and perfectly and partially aligned as well as randomly oriented spheroids.

Farafonov (2000) derived the formulas of the RA for multilayered ellipsoids. Muinonen (1996, 2000) and Battaglia *et al.* (1999) applied the RA to so-called Gaussian random spheres. Jones (1979) extended the RA to clusters of small spheres (see also Mackowski 1995, and references therein).

Stevenson (1953) generalized the RA by expanding the internal and scattered electric fields in powers of the size parameter x. The first term, which is $O(x^2)$, gives the RA whereas the second term, $O(x^4)$, gives the so-called Rayleigh–Gans–Stevenson approximation. This approach was extended to inhomogeneous objects by von Ross (1971) and applied to various scattering problems by Stevenson (1968) and Khlebtsov (1979).

Another way of deriving the formulas of the Rayleigh or higher-order approximations is to analyze an exact solution in the limit $x \to 0$. For example, one can use the expansions

$$j_n(z) = \frac{z^n}{1\times 3\times 5\times\cdots\times(2n+1)}\left\{1-\frac{\frac{1}{2}z^2}{1!(2n+3)}+\frac{(\frac{1}{2}z^2)^2}{2!(2n+3)(2n+5)}-\cdots\right\}, \tag{7.1}$$

$$y_n(z) = -\frac{1\times 3\times 5\times\cdots\times(2n-1)}{z^{n+1}}\left\{1-\frac{\frac{1}{2}z^2}{1!(1-2n)}+\frac{(\frac{1}{2}z^2)^2}{2!(1-2n)(3-2n)}-\cdots\right\}, \quad n=0,1,2,... \tag{7.2}$$

for the spherical Bessel functions of the first and second kind (Abramowitz and Stegun 1964, p. 437) along with Eq. (C.1) and Lorenz–Mie formulas of Section 5.7 and subsection 5.8.5 to derive the following classical equations of the RA for small homogeneous spheres:

$$Q_{\rm sca} \underset{x\to 0}{=} \frac{8}{3}x^4\left|\frac{m^2-1}{m^2+2}\right|^2, \tag{7.3}$$

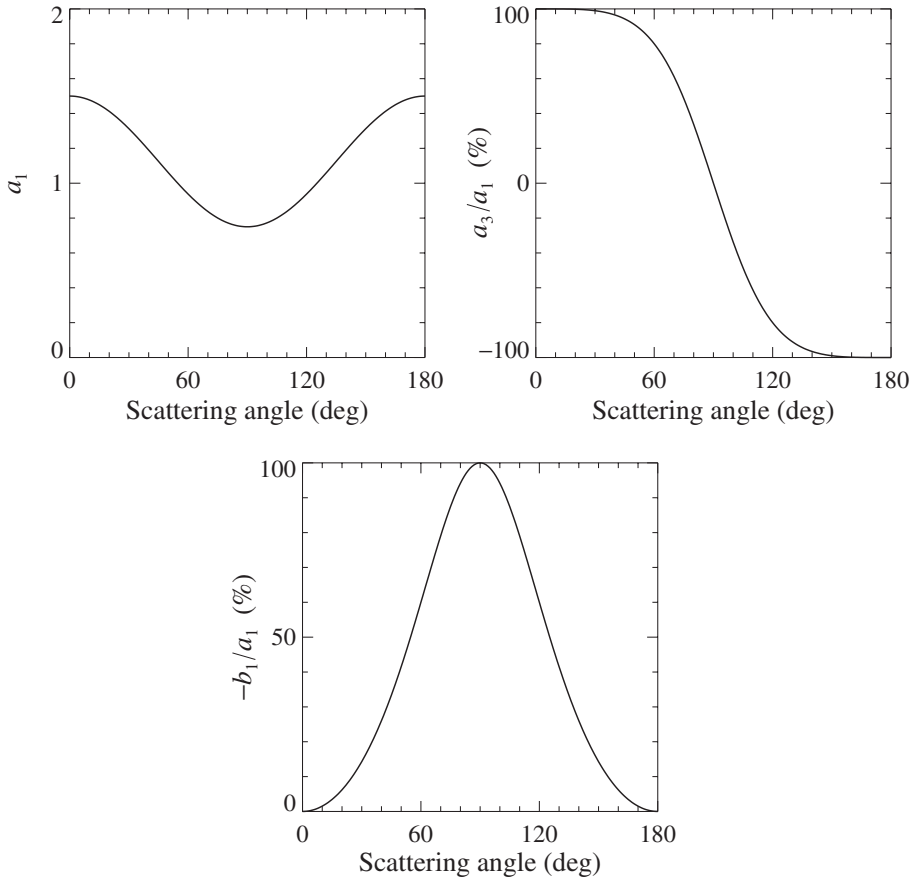

Figure 7.1. The phase function $a_1(\Theta)$ and the ratios $a_3(\Theta)/a_1(\Theta)$ and $-b_1(\Theta)/a_1(\Theta)$ versus scattering angle Θ for a homogeneous sphere in the Rayleigh limit.

$$Q_{\text{abs}} \underset{x\to 0}{=} 4x\,\text{Im}\left(\frac{m^2-1}{m^2+2}\right), \tag{7.4}$$

$$\widetilde{\mathbf{F}}(\Theta) \underset{x\to 0}{=} \frac{3}{4}\begin{bmatrix} 1+\cos^2\Theta & -\sin^2\Theta & 0 & 0 \\ -\sin^2\Theta & 1+\cos^2\Theta & 0 & 0 \\ 0 & 0 & 2\cos\Theta & 0 \\ 0 & 0 & 0 & 2\cos\Theta \end{bmatrix}, \tag{7.5}$$

where $x = 2\pi r/\lambda_1$ is the size parameter and r is the sphere radius (Bohren and Huffman 1983). Figure 7.1 visualizes the elements of the normalized Stokes scattering matrix of Eq. (7.5), whereas Table 7.1 lists the respective expansion coefficients (de Rooij 1985). The scattering efficiency factor in the Rayleigh approximation is inversely proportional to the fourth power of the wavelength, the absorption efficiency factor is inversely proportional to the wavelength, and the absorption cross section $C_{\text{abs}} = \pi r^2 Q_{\text{abs}}$ is proportional to the particle volume $V = \frac{4}{3}\pi r^3$:

Table 7.1. Expansion coefficients for the normalized Stokes scattering matrix of a homogeneous sphere in the Rayleigh limit

s	α_1^s	α_2^s	α_3^s	α_4^s	β_1^s	β_2^s
0	1	0	0	0	0	0
1	0	0	0	$3/2$	0	0
2	$1/2$	3	0	0	$\sqrt{3/2}$	0

$$Q_{\rm sca} \underset{x\to 0}{\propto} \frac{1}{\lambda_1^4}, \qquad Q_{\rm abs} \underset{x\to 0}{\propto} \frac{1}{\lambda_1}, \qquad C_{\rm abs} \underset{x\to 0}{\propto} V. \tag{7.6}$$

Equations (7.3) and (7.4) indicate that for small particles with at least moderate absorption, extinction is dominated by absorption. The rapid increase in the scattering cross section with decreasing wavelength causes air molecules to scatter more blue than red light and transmit more red than blue light. This behavior explains the blue color of the clear sky and the familiar reddening of the sunset. The Rayleigh phase function (the upper left panel in Fig. 7.1) is nearly isotropic and is symmetric with respect to the scattering angle $\Theta = 90°$, thereby yielding an asymmetry parameter equal to zero:

$$\langle \cos\Theta \rangle \underset{x\to 0}{=} 0. \tag{7.7}$$

The degree of linear polarization of scattered light for unpolarized incident light, $P_Q(\Theta) = -Q^{\rm sca}(\Theta)/I^{\rm sca}(\Theta) = -b_1(\Theta)/a_1(\Theta)$ (the panel at the lower level in Fig. 7.1), is always positive, has the classical bell-like shape, and reaches 100% at the scattering angle $\Theta = 90°$.

In a similar fashion, the extended boundary condition method can be used to derive closed-form analytical formulas of the RA for very small spheroids (Tsang *et al.* 1985, pp. 192–3).

7.2 Rayleigh–Gans approximation

The conditions of validity of the Rayleigh–Gans approximation (RGA) (otherwise known as the Rayleigh–Debye or Born approximation; e.g., Ishimaru 1997, Section 2.6) are $x|m-1| \ll 1$ and $|m-1| \ll 1$. In other words, the particles are assumed to be not too large (although they may be larger than in the case of Rayleigh scattering) and optically "soft". The fundamental assumption of the RGA is that each volume element of the scattering object is excited only by the incident field. The scattered field is then computed from Eq. (2.22) after substituting $\mathbf{E}(\mathbf{r}') = \mathbf{E}^{\rm inc}(\mathbf{r}')$. This simplifying assumption leads to significant analytical progress in many specific cases. Also, like many other asymptotic approximations, the RGA may often be useful outside its formally defined range of validity (e.g., Barber and Wang 1978). Acquista (1976) generalized the RGA by applying the method of successive iterations (Shifrin 1968) to

Eq. (2.16). This approach was applied to spheroids and finite circular cylinders and is valid for $x|m-1| \lesssim 1$ (Haracz *et al.* 1984, 1985, 1986). Khlebtsov (1984) derived an exact integral equation of Lippman–Schwinger type by taking the Fourier transform of Eq. (2.16). Successive iterations of this equation give the RGA, the Acquista result, and higher-order approximations. This approach was extended to anisotropic scatterers and applied to suspensions of aligned particles by Khlebtsov and Melnikov (1991) and Khlebtsov *et al.* (1991). Muinonen (1996, 2000) applied the RGA to particles with Gaussian random surfaces.

7.3 Anomalous diffraction approximation

The anomalous diffraction approximation (ADA) was introduced by van de Hulst (1957, Chapter 11) as a means of computing the extinction cross section for large, optically soft spheres with $x \gg 1$ and $|m-1| \ll 1$. Since the second condition means that rays are weakly deviated as they cross the particle boundary and there is negligible reflection, the ADA implies that extinction is caused by (i) absorption of light passing through the particle and (ii) interference of the light passing through the particle and the light passing around the particle. This simplification allows a general representation of the extinction and absorption cross sections as simple integrals over the particle projection on the plane perpendicular to the incident beam. The integrals can be evaluated numerically or, in some special cases, analytically. The ADA has been applied to prismatic columns (Chýlek and Klett 1991a, b), hexagonal ice crystals (Chýlek and Videen 1994; Sun and Fu 1999), spheroids (Evans and Fournier 1994; Baran *et al.* 1998), cubes (Masłowska *et al.* 1994), ellipsoids (Streekstra *et al.* 1994), and finite circular cylinders (Liu *et al.* 1998). Comparisons of the ADA and the exact *T*-matrix results (Liu *et al.* 1998) suggest that the ADA estimate of extinction is more accurate for randomly oriented nonspherical particles than for spheres, and that the ADA errors in absorption decrease with increasing imaginary part of the relative refractive index. Meeten (1982) and Khlebtsov (1993) extended the ADA to scattering by anisotropic particles and fractal clusters, respectively. The ADA and the closely related Wentzel–Kramers–Brillouin and eikonal approximations belong to the family of high-energy approximations (e.g., Perrin and Lamy 1986; Bourrely *et al.* 1989; Klett and Sutherland 1992; Sharma and Somerford 1999; Shepelevich *et al.* 1999).

7.4 Geometrical optics approximation

The geometrical optics approximation (GOA) (otherwise known as the ray-tracing or ray optics approximation) is a universal approximate method for computing light scattering by arbitrarily shaped and arbitrarily oriented particles with sizes much larger than the incident wavelength. The GOA is based on the assumption that the

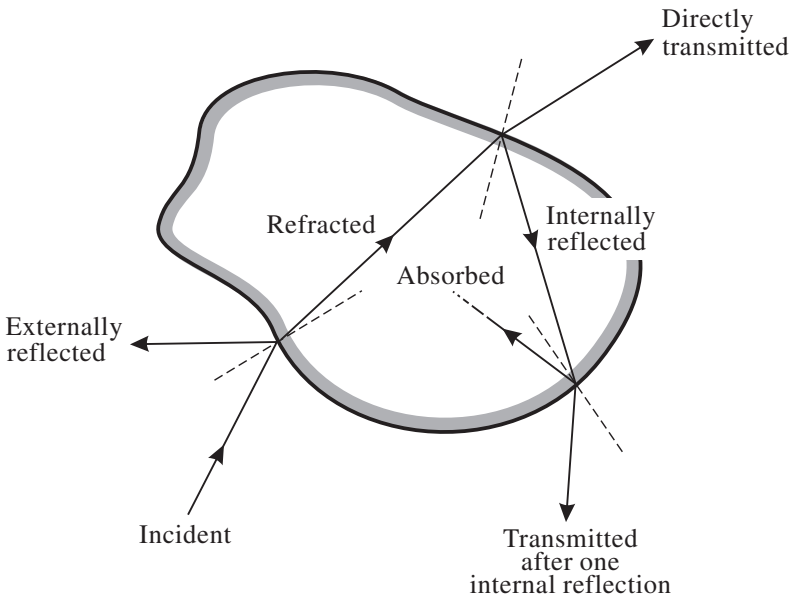

Figure 7.2. Ray-tracing diagram for scattering at a single particle.

incident plane wave can be represented as a collection of parallel rays which pursue independent paths and that it is possible to distinguish between rays striking different local regions on the particle's surface. Numerical results are obtained by tracing the histories of a large number of uniformly spaced rays striking the particle. Each incident ray is partially refracted into the particle and partially reflected (Fig. 7.2). The Stokes parameters of the refracted and reflected parts of the ray and the direction of the refracted part are determined using Fresnel's formula and Snell's law, respectively (Jackson 1998, Section 7.3). The refracted ray may emerge after another refraction, possibly following one or more internal reflections, and it may be attenuated by absorption inside the particle. Each internal ray is traced until its intensity decreases below a prescribed cut-off value. Varying the polarization state of the incident rays, sampling all escaping rays into predefined narrow angular bins, and adding incoherently the respective Stokes parameters yields a quantitative representation of the particle scattering properties in terms of the ray-tracing phase matrix $\mathbf{Z}^{\mathrm{RT}}$. Because all rays impinging on the particle surface are either scattered or absorbed irrespective of their polarization state, the ray-tracing extinction matrix is always diagonal and is given by

$$\mathbf{K}^{\mathrm{RT}} = C_{\mathrm{ext}}^{\mathrm{RT}} \boldsymbol{\Delta}, \tag{7.8}$$

where $\boldsymbol{\Delta}$ is the 4×4 unit matrix. The ray-tracing extinction cross section $C_{\mathrm{ext}}^{\mathrm{RT}}$ does not depend on the polarization state of the incident light and is equal to the geometrical area G of the particle projection on the plane perpendicular to the incidence direction:

$$C_{\mathrm{ext}}^{\mathrm{RT}} = G. \tag{7.9}$$

Since the presence of the particle modifies the incident plane wave front by eliminating a part that has the shape and size of the geometrical projection of the particle, the ray-tracing scattering pattern must be supplemented by the computation of Fraunhofer diffraction of the incident wave on the particle projection. The diffraction component of the phase matrix $\mathbf{Z}^{\rm D}$ is confined to a narrow angular cone centered at the exact forward-scattering direction and is usually computed in the Kirchhoff approximation (Jackson 1998), thereby contributing only to the diagonal elements of the total phase matrix (Muinonen 2000). The diffraction component $\mathbf{K}^{\rm D}$ of the total geometrical optics extinction matrix $\mathbf{K}^{\rm GO}$ is simply the product of G and the 4×4 unit matrix and is equal to the ray-tracing component $\mathbf{K}^{\rm RT}$. We thus have

$$\mathbf{Z}^{\rm GO} = \mathbf{Z}^{\rm RT} + \mathbf{Z}^{\rm D} = \mathbf{Z}^{\rm RT} + Z_{11}^{\rm D}\boldsymbol{\Delta}, \tag{7.10}$$

$$\mathbf{K}^{\rm GO} = \mathbf{K}^{\rm RT} + \mathbf{K}^{\rm D} = C_{\rm ext}^{\rm GO}\boldsymbol{\Delta}, \tag{7.11}$$

where

$$C_{\rm ext}^{\rm GO} = C_{\rm ext}^{\rm RT} + C_{\rm ext}^{\rm D} = 2G. \tag{7.12}$$

The geometrical optics scattering cross section is the sum of the ray-tracing and diffraction components:

$$C_{\rm sca}^{\rm GO} = C_{\rm sca}^{\rm RT} + C_{\rm sca}^{\rm D}. \tag{7.13}$$

Since the diffracted energy is not absorbed, the diffraction scattering cross section is equal to the diffraction extinction cross section:

$$C_{\rm sca}^{\rm D} = C_{\rm ext}^{\rm D} = G. \tag{7.14}$$

The ray-tracing scattering cross section $C_{\rm sca}^{\rm RT}$ is found from $\mathbf{Z}^{\rm RT}$ and Eq. (2.160). Energy conservation requires that it be always smaller than or equal to the ray-tracing extinction cross section:

$$C_{\rm sca}^{\rm RT} \leq C_{\rm ext}^{\rm RT} = G. \tag{7.15}$$

GOA computations are particularly straightforward for spheres because the ray paths always remain in a plane (Liou and Hansen 1971), thereby simplifying the ray-tracing part of the computation, while the diffraction component of the phase matrix is given by a closed-form analytical formula (cf. Bohren and Huffman 1983, p. 110)

$$\mathbf{Z}^{\rm D}(\hat{\mathbf{n}}^{\rm sca}, \hat{\mathbf{n}}^{\rm inc}) \underset{x\to\infty}{=} \frac{Gx^2}{16\pi}\left[\frac{2J_1(x\sin\Theta)}{x\sin\Theta}\right]^2 (1+\cos\Theta)^2\boldsymbol{\Delta}, \tag{7.16}$$

where x is the size parameter of the sphere, $\Theta = \arccos(\hat{\mathbf{n}}^{\rm sca}\cdot\hat{\mathbf{n}}^{\rm inc})$ is the scattering angle, and $J_1(z)$ is the Bessel function of order unity. Figure 7.3 shows the quantity $[2J_1(x\sin\Theta)/(x\sin\Theta)]^2$ as a function of $x\sin\Theta$. It is seen that for $x \gg 1$ essentially all the diffracted light is confined within an angular cone of half-width $\Theta \cong 7/x$. The respective ray-tracing asymmetry parameter is equal to unity to high precision:

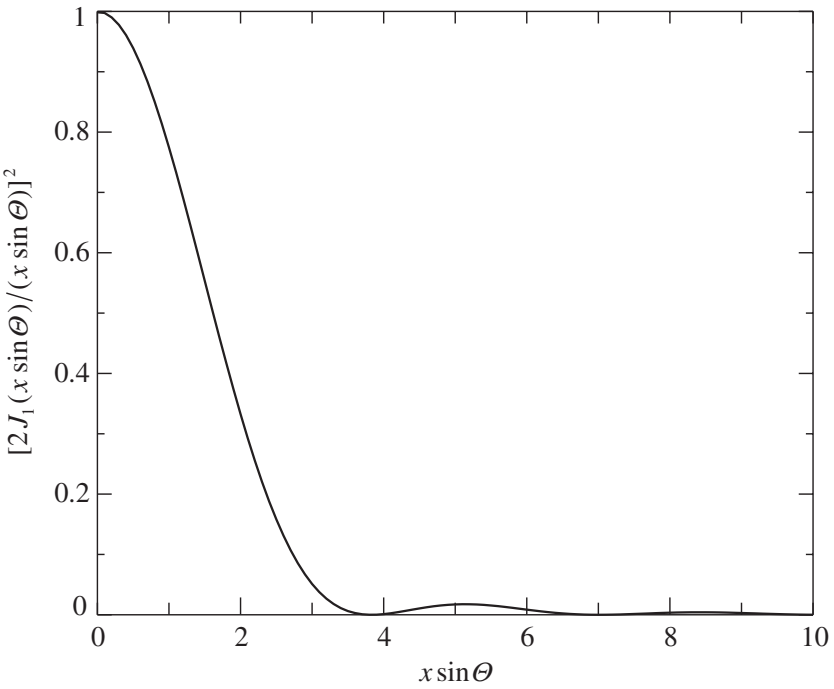

Figure 7.3. Angular distribution of the diffracted intensity.

$$\langle \cos\Theta \rangle^{\mathrm{RT}} \underset{x\to\infty}{\to} 1. \tag{7.17}$$

For nonspherical particles, ray tracing is usually performed using a Monte Carlo approach, whereas the diffraction is often approximated by Eq. (7.16) evaluated for an equal-projected-area sphere (more accurate approaches have been discussed by Takano and Asano (1983), Muinonen (1989), Petrushin (1994), and Yang and Liou (1998a)). Wendling *et al.* (1979), Cai and Liou (1982), Volkovitsky *et al.* (1984), Takano and Jayaweera (1985), Rockwitz (1989), Takano and Liou (1989a), Masuda and Takashima (1992), and Xu *et al.* (1997) applied the GOA to hexagonal columns and plates in random and horizontal orientations, whereas Yang and Cai (1991), Macke and Mishchenko (1996), and Kokhanovsky and Nakajima (1998) computed scattering by randomly oriented spheroids and finite circular cylinders. Light scattering by various polyhedral shapes has been studied by Liou *et al.* (1983), Muinonen *et al.* (1989), Macke (1993), Iaquinta *et al.* (1995), Takano and Liou (1995), Liu *et al.* (1996), Macke *et al.* (1996b), and Yang and Liou (1998a). The GOA has been applied also to distorted raindrops (Macke and Großklaus 1998; Nousiainen and Muinonen 1999; Nousiainen 2000) and large randomly shaped (stochastic) particles (Peltoniemi *et al.* 1989; Macke *et al.* 1996b; Muinonen *et al.* 1996; Hess *et al.* 1998; Yang and Liou, 1998a; Han *et al.* 1999; Grundy *et al.* 2000; Muinonen 2000).

Macke *et al.* (1996a), Mishchenko and Macke (1997), C.-Labonnote *et al.* (2000), Macke (2000), and Hillier and Buratti (2001) have used the GOA to compute scattering and absorption properties of large particles containing multiple randomly posi-

tioned small inclusions with an index of refraction different from that of the host. The ray-tracing procedure assumes that each inclusion scatters light independently of all other inclusions, thereby implying that the mean distance between the inclusions is greater than a few times their radii (Section 3.3). The inclusions are usually assumed to be spherical, and their single-scattering and absorption properties are computed using the Lorenz–Mie theory. However, nonspherical inclusions can also be accommodated. After an incident ray is refracted into the host particle, it is allowed to travel a straight random path length that depends on the number density of the inclusions and their average extinction cross section. If the ray has not reached the boundary of the host particle, its propagation direction is then changed in accordance with the average inclusion phase function and its energy is multiplied by the average inclusion single-scattering albedo. This process is continued until the ray reaches the host boundary, where it is partially refracted out of the host and partially internally reflected. The entire procedure is repeated for the internally reflected component. The history of the internal ray is traced until its energy falls below a specific threshold. This technique is in essence a Monte Carlo solution of the radiative transfer equation for the interior of the host particle subject to the Fresnel boundary conditions on the host particle surface (Section 3.4).

A collection of GOA codes applicable to a wide variety of problems has been developed by Andreas Macke and is publicly available at http://www.ifm-geomar.de/index.php?id=981&L=1.

The main advantage of the GOA is that it can be applied to essentially any shape. However, this technique is approximate by definition, and its range of applicability in terms of the smallest allowable size parameter must be checked by comparing the GOA results with exact numerical solutions of the Maxwell equations. As an example, Figs. 7.4 and 7.5 depict the results of GOA and Lorenz–Mie computations of the phase function $a_1(\Theta)$ and the ratio $-b_1(\Theta)/a_1(\Theta)$ versus scattering angle Θ for nonabsorbing homogeneous spheres with relative refractive indices m = 1.33 and m = 1.53 and size parameters x = 40, 160, and 600. The computations were performed using the ray-tracing code described by Macke and Mishchenko (1996) and the Lorenz–Mie code described in Section 5.10. In order to smooth out interference and resonance effects (Section 9.1), the Lorenz–Mie results have been averaged over a narrow size distribution given by Eq. (5.245) with b = 0.07, so that x represents the effective size parameter $2\pi r_{\rm eff}/\lambda_1$, where $r_{\rm eff}$ is given by Eq. (5.248). The ray-tracing and diffraction components of the GOA phase functions have been averaged over 1°-wide angular bins. It is clear that the GOA phase-function results for spheres become reasonably accurate only at size parameters exceeding several hundred. Furthermore, the GOA completely fails to reproduce the strong enhancement of intensity in the backscattering direction ($\Theta \cong 180°$) observed for m = 1.33 and usually associated with so-called surface waves (cf. Section 9.4). Obtaining good accuracy in GOA computations of the ratio $-b_1(\Theta)/a_1(\Theta)$ requires even larger size parameters (Fig. 7.5).

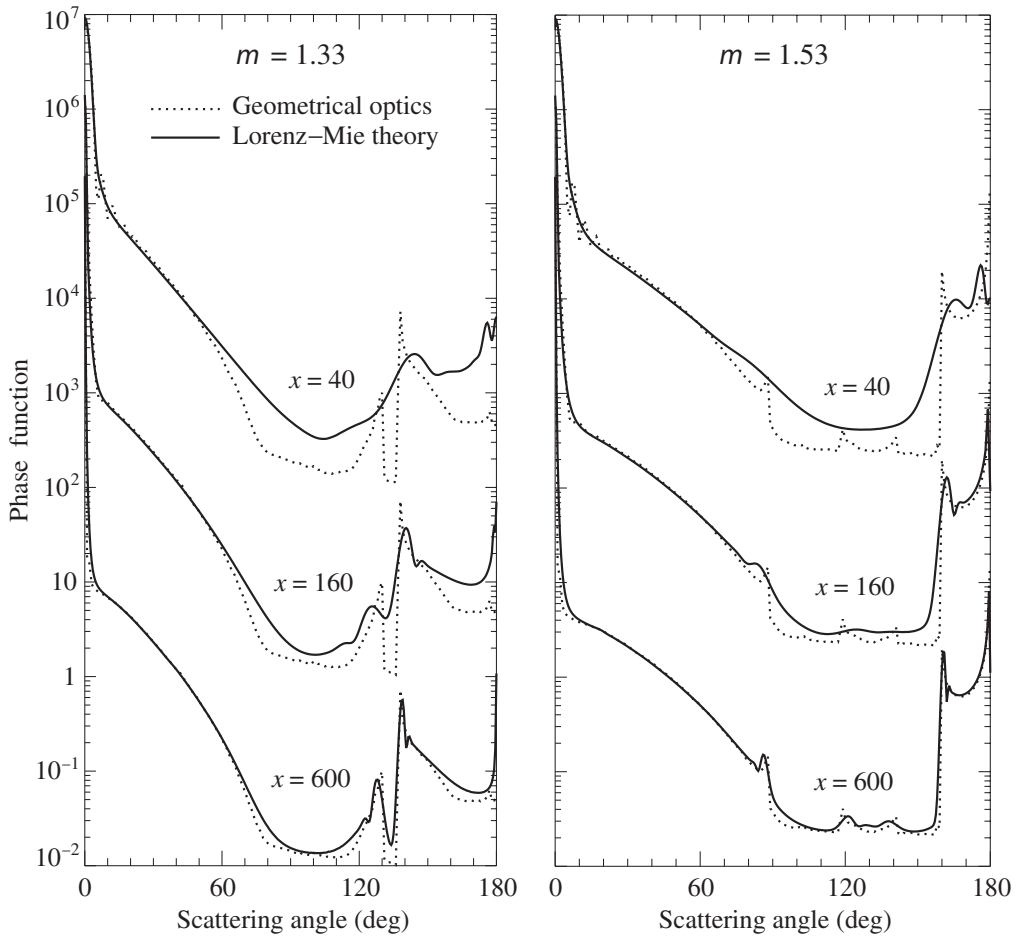

Figure 7.4. Phase function $a_1(\Theta)$ versus scattering angle Θ computed with the GOA and the Lorenz–Mie theory for homogeneous spheres with relative refractive indices $m = 1.33$ and $m = 1.53$ and size parameters $x = 40$, 160, and 600. The vertical axis scale applies to the curves with $x = 600$, the other curves being successively displaced upward by a factor of 100. (After Hansen and Travis 1974.)

Shown in Fig. 7.6 are results of GOA and *T*-matrix computations of the phase function for monodisperse, randomly oriented circular cylinders with a diameter-to-length ratio of unity, relative refractive index $m = 1.311$, and surface-equivalent-sphere size parameters x_s varying from 40 to 180; Fig. 7.7 depicts all elements of the normalized Stokes scattering matrix for $x_s = 180$. The small-amplitude ripple in the *T*-matrix curves is caused by interference effects characteristic of monodisperse particles. Averaging over cylinder orientations makes this ripple much weaker than for monodisperse surface-equivalent spheres and can be eliminated entirely by averaging over a narrow size distribution. Contrasting Figs. 7.4 and 7.5 with Figs. 7.6 and 7.7 seems to suggest that GOA results for nonspherical particles may be somewhat more accurate for a given size parameter than those for surface-equivalent spheres (Macke *et al.* 1995; Mishchenko and Macke 1999). However, it is clear that although the

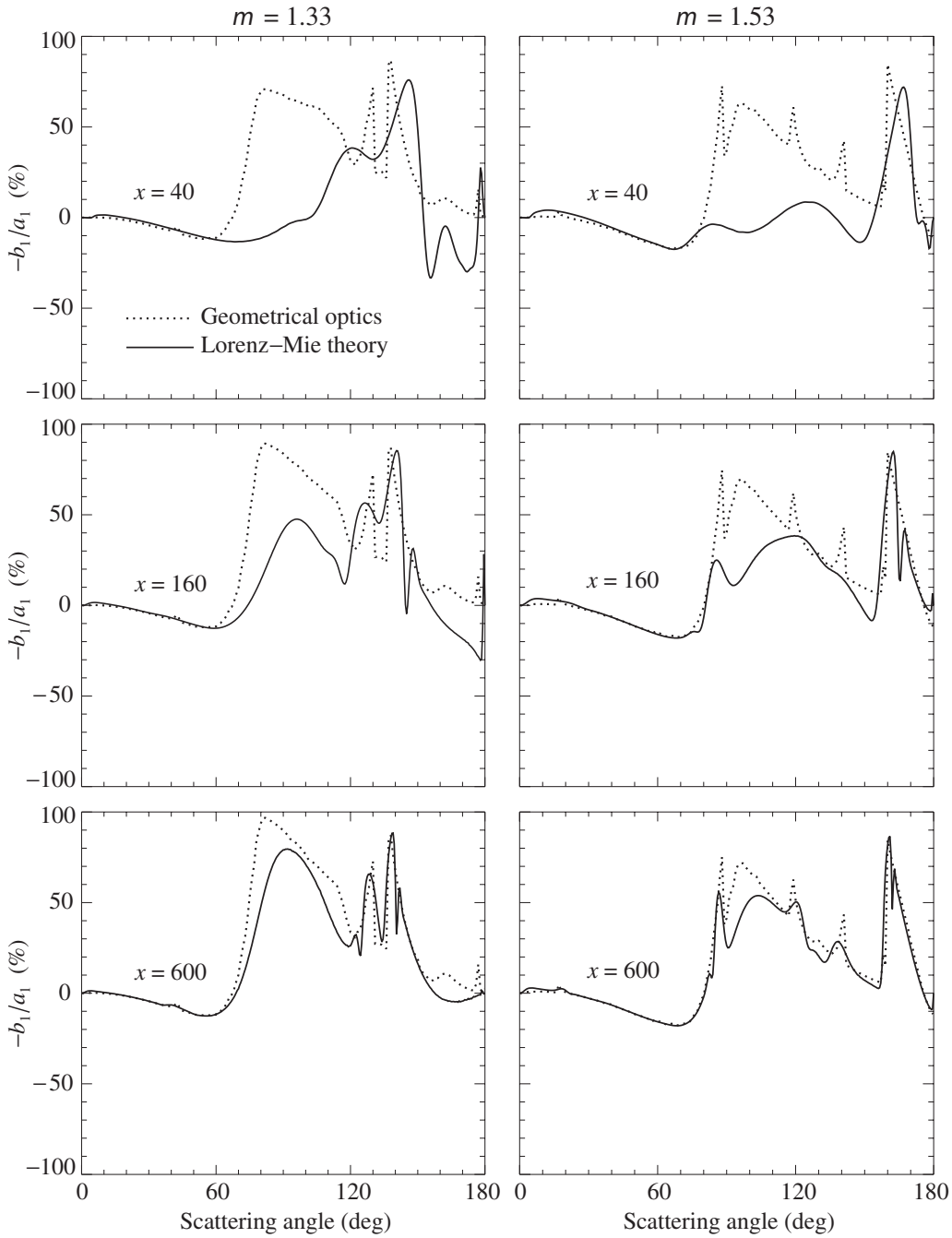

Figure 7.5. The ratio $-b_1(\Theta)/a_1(\Theta)$ versus scattering angle Θ computed with the GOA and the Lorenz–Mie theory for homogeneous spheres with relative refractive indices $m = 1.33$ and $m = 1.53$ and size parameters $x = 40$, 160, and 600. (After Hansen and Travis 1974.)

main geometrical optics features can be qualitatively reproduced by particles with size parameters less than 100, obtaining good quantitative accuracy in GOA computations of the scattering matrix for nonspherical particles still requires size parameters exceeding a few hundred.

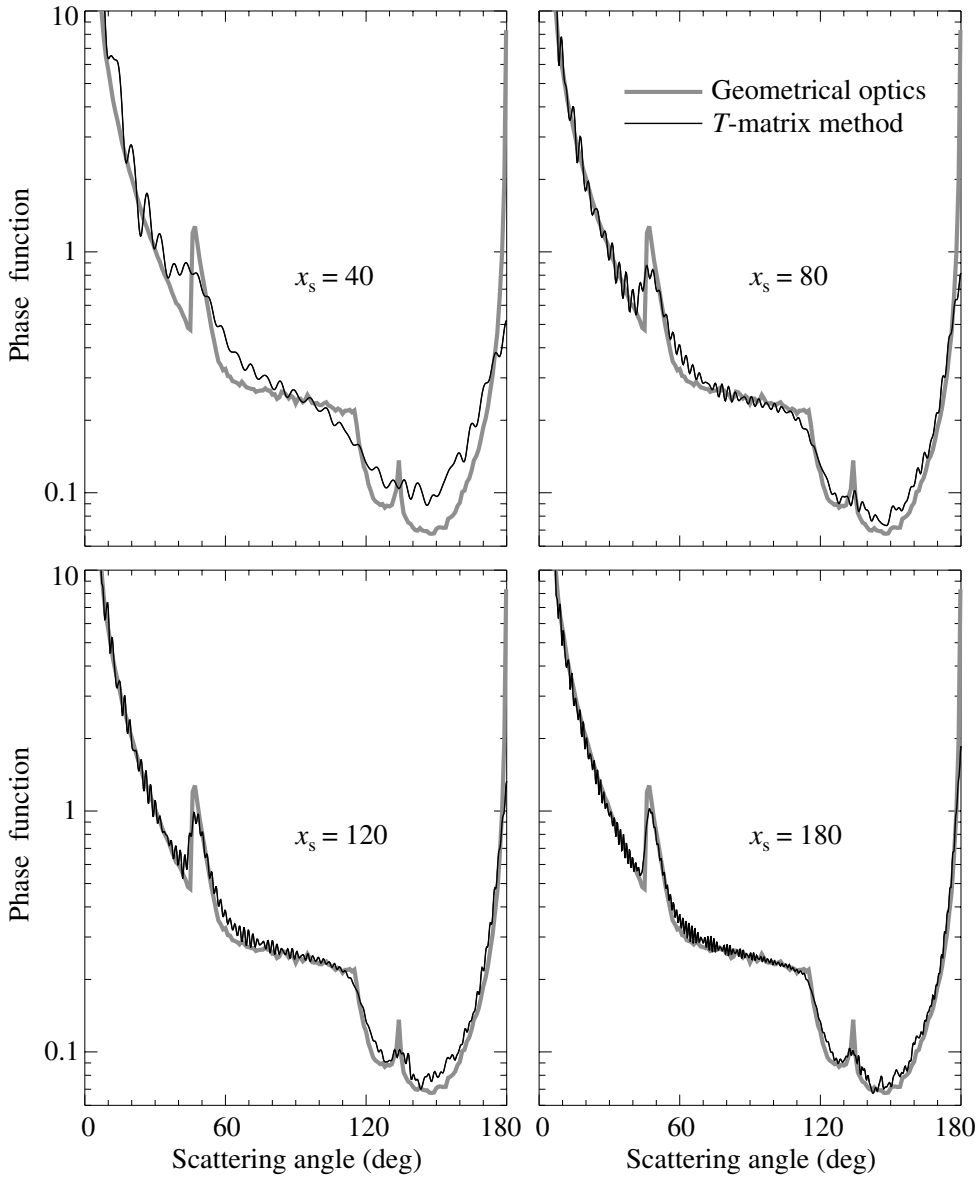

Figure 7.6. GOA and *T*-matrix phase functions for monodisperse, randomly oriented circular cylinders with surface-equivalent-sphere size parameters x_s = 40, 80, 120, and 180.

GOA computations for absorbing particles (i.e., with a non-zero imaginary part of the relative refractive index) are more complicated because in this case the refracted waves are inhomogeneous, so that the surface of constant amplitude does not coincide with the surface of constant phase. Formally, Snell's law can still be used, but it must be modified as described by Stratton (1941, Section 9.8) (see also Ulaby *et al.* 1981, Section 2-8). The consequences of this modification were discussed by Yang and Liou (1995) and Zhang and Xu (1995) and may often be neglected. The effect of absorption on the accuracy of ray-tracing computations has been analyzed further by Yang *et al.* (2001a).

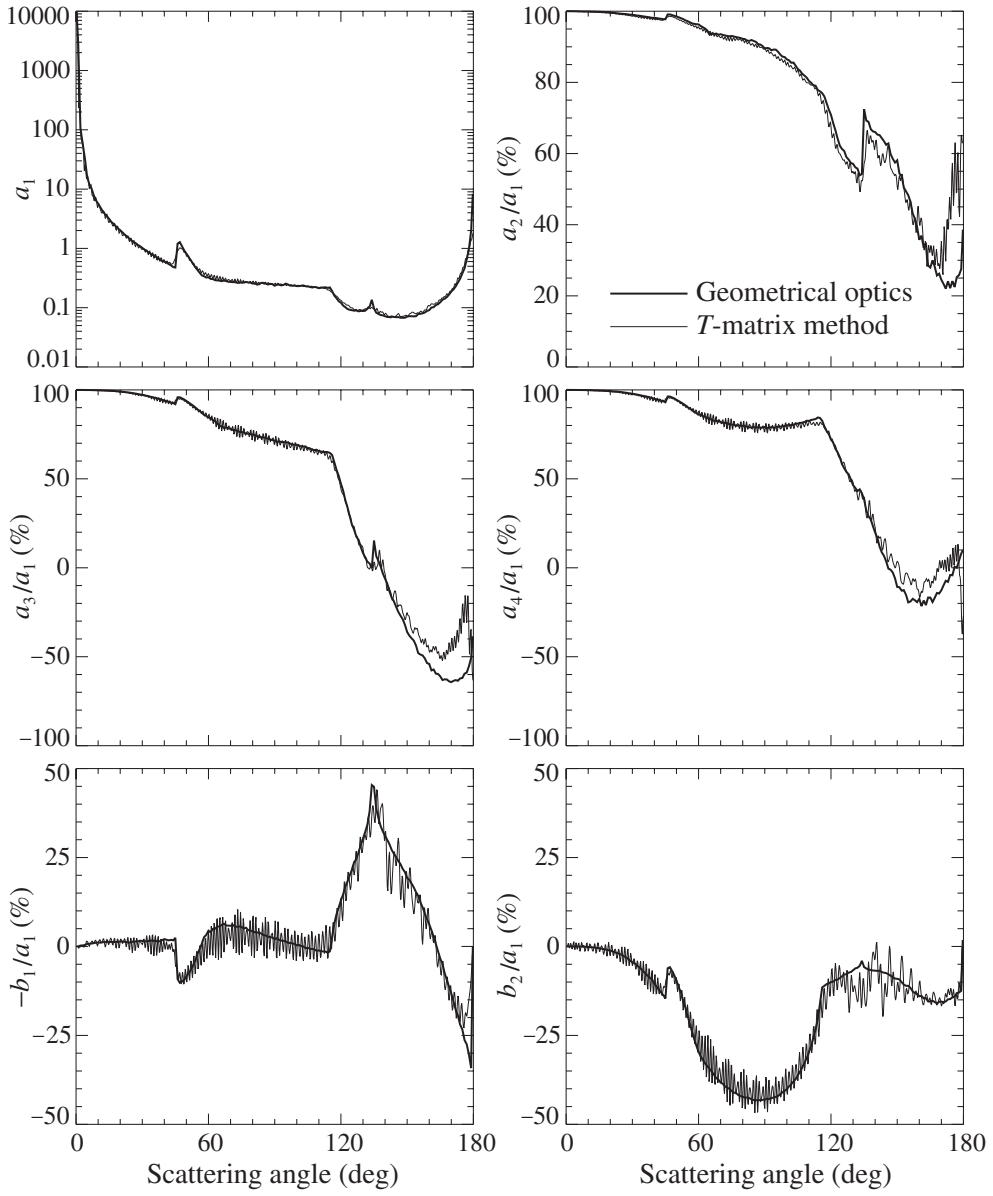

Figure 7.7. Elements of the normalized Stokes scattering matrix for monodisperse, randomly oriented circular cylinders with a surface-equivalent-sphere size parameter $x_s = 180$.

The failure to reproduce the backscattering enhancement of intensity caused by surface waves in spherical particles is not the only inherent deficiency of the GOA. For example, the GOA predicts that for crystals with parallel plane facets the ray-tracing component of the phase function should have a delta-function peak in the exact forward-scattering direction because the direction of the incident rays is not changed after they undergo two refractions through parallel plane interfaces, as demonstrated in Fig. 7.8. This effect is called the delta-function transmission (Liou 1992). It is clear, however, that the GOA predicts the infinitesimally narrow trans-

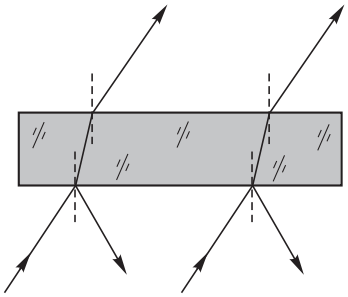

Figure 7.8. The direction of incident rays is not changed after they are refracted twice by parallel plane facets.

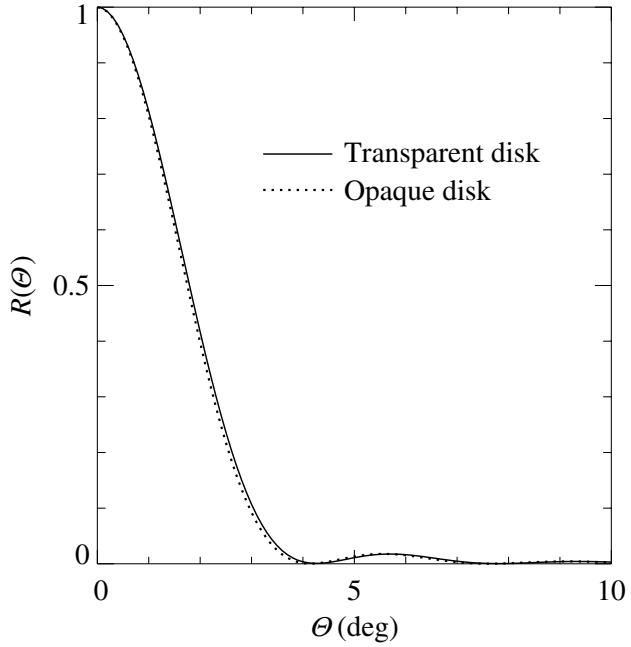

Figure 7.9. The angular profile of the ratio R defined by Eq. (7.18) for transparent and opaque circular disks.

mission peak only because it ignores physical optics effects. Figure 7.9 shows the results of exact T-matrix computations of the ratio

$$R(\Theta) = \frac{Z_{11}(\vartheta^{\rm sca} = \Theta,\, \varphi^{\rm sca} = 0;\, \vartheta^{\rm inc} = 0,\, \varphi^{\rm inc} = 0)}{Z_{11}(\vartheta^{\rm sca} = 0,\, \varphi^{\rm sca} = 0;\, \vartheta^{\rm inc} = 0,\, \varphi^{\rm inc} = 0)} \tag{7.18}$$

for two circular disks with diameter-to-length ratio 3 and size parameter $\pi D/\lambda_1 = 50$, where D is the diameter of each disk and λ_1 is the wavelength of the incident light in the surrounding medium. The first disk has a relative refractive index of 1.31 and is transparent (nonabsorbing), whereas the second disk has a relative refractive index of 1.31 + i0.1 and is rather opaque. Both disks are illuminated by unpolarized light inci-

dent along their axis of rotation, and $R(\Theta)$ is the ratio of the intensity of light scattered at an angle Θ to the intensity of light scattered in the exact forward direction. If the GOA prediction of the delta-function transmission were correct then the curve for the opaque disk would have only the diffraction component whereas that for the transparent disk would be a superposition of the diffraction pattern and a much narrower delta-function transmission component. However, the rigorous *T*-matrix computations show that although the $Z_{11}(0, 0; 0, 0)$ value for the transparent disk is almost three times greater than that for the opaque disk, the angular profiles of the ratio $R(\Theta)$ for both disks is essentially the same. This result unequivocally indicates that the delta-function transmission contribution is not a true delta function but rather has the same angular profile as the Fraunhofer diffraction peak (Mishchenko and Macke 1998).

The explanation of this result is that a wave front emerging from any finite flat crystal facet (e.g., from the top facet of the particle shown in Fig. 7.8) should spread and produce an angular intensity distribution in the far-field zone similar to the Fraunhofer diffraction pattern (Volkovitsky *et al.* 1984; Muinonen *et al.* 1989). This applies not only to the transmitted light but also to the externally reflected light. For example, the plane wave front emerging from the bottom facet of the particle shown in Fig. 7.8 also spreads and produces a Fraunhofer-like angular distribution of the specularly reflected intensity, albeit twice as narrow as the diffracted intensity distribution (Mishchenko *et al.* 1997b). Both effects can have significant ramifications for laboratory and remote sensing techniques exploiting exact forward-scattering, backscattering, and specular directions (e.g., Platt 1978; Chepfer *et al.* 1999; Reichardt *et al.* 2000b).

Since the standard ray-tracing procedure does not take into account phase relations between different rays, the GOA ignores the effect of coherent backscattering (Section 3.4). It may, therefore, underestimate the contribution of rays propagating inside the particle along the same paths but in opposite directions and exiting the particle in the direction opposite to the incidence direction. This underestimation may be especially significant for particles with multiple internal inclusions, and one should correct for it by explicitly tracing not only the energies (or, more generally, the Stokes parameters) of the rays but also their phases and by taking into account interference effects (e.g., Göbel *et al.* 1998). Although coherent backscattering does not change the optical cross sections of the composite particle and is unlikely to modify noticeably its asymmetry parameter, it may increase substantially the backscattering phase function and, therefore, affect the results of laboratory and remote sensing studies using backscattered light (e.g., the results of lidar measurements).

To improve the performance of the geometrical optics approximation, Ravey and Mazeron (1982, 1983) developed the so-called physical optics or Kirchhoff approximation. This approach is based on Eq. (5.168) supplemented by the far-field asymptotic of Eq. (2.20). Equation (5.168) expresses the scattered field in terms of the electric and magnetic fields on the exterior side of the particle surface. The latter are

computed approximately using Fresnel's formulas and the standard ray-tracing procedure. The main difference from the conventional GOA scheme is the coherent adding of fields rather than the incoherent adding of Stokes parameters of the scattered rays; this allows the Kirchhoff approximation to preserve the phase information and reproduce physical optics effects completely ignored by the GOA scheme. The physical optics approach was used, with some variations, by Muinonen (1989), Yang and Liou (1995, 1996b), Mazeron and Muller (1996), and Yang *et al.* (2000a) and was found to be rather time consuming. Since this technique is still an approximation, its accuracy as a function of size parameter should be extensively tested versus exact solutions, especially when the full scattering matrix is computed.

7.5 Perturbation theories

The idea of the perturbation theory (PT) approach is to define the surface of an irregular particle in spherical coordinates by $r(\vartheta, \varphi) = r_0[1 + \xi f(\vartheta, \varphi)]$, where r_0 is the radius of the "unperturbed" sphere, ξ is a "smallness parameter", and $f(\vartheta, \varphi)$ obeys the condition $|f(\vartheta, \varphi)| < 1$. The fields inside and outside the particle are expanded in vector spherical wave functions and the expansion coefficients, which are determined through the requirement of the standard boundary conditions, are expressed as power series in ξ (Oguchi 1960; Yeh 1964; Erma 1969). Similar approaches were developed by Ogura and Takahashi (1990) and Martin (1993). Note that the application of the boundary conditions explicitly relies on the (unproven) validity of the Rayleigh hypothesis (see Section 6.4).

Schiffer (1989, 1990) combined the PT with an analytical orientation-averaging procedure to compute the scattering properties of randomly oriented particles. He also reported many numerical results obtained with the second-order PT and compared them with exact *T*-matrix computations by Mugnai and Wiscombe (1980) and Wiscombe and Mugnai (1988) for Chebyshev particles. The second-order PT showed good accuracy only for $2\pi r_0 / \lambda_1 < 7$ and only if the surface deviations from the unperturbed sphere were much smaller than the wavelength. Similar conclusions were reached by Kiehl *et al.* (1980) on the basis of first-order PT computations. Battaglia *et al.* (1999), Muinonen (2000), and Nousiainen *et al.* (2001) have applied the second-order PT to Gaussian random particles.

Lacoste *et al.* (1998) and Lacoste and van Tiggelen (1999) considered light scattering by a Faraday-active dielectric sphere imbedded in an isotropic medium with no magneto-optical properties and subject to a homogeneous external magnetic field. They computed the amplitude and Stokes scattering matrices by using a perturbation approach and keeping only terms proportional to the first order of the magnetic field.

7.6 Other approximations

If the thickness of a particle in one of its dimensions is much smaller than a wavelength, it is often possible to approximate the integral equations describing the scattering process. This approach was applied to thin finite cylinders by Uzunoglu *et al.* (1978), to thin cylinders and disks by Schiffer and Thielheim (1979) and Fung (1994, Section 11.2), to thin disks by Weil and Chu (1980), and to thin-walled cylinders by Senior and Weil (1977).

Equation (2.16) can be used to compute the scattered field provided that the internal field is known. Le Vine *et al.* (1985) calculated the electromagnetic scattering from a homogeneous dielectric disk with a radius much larger than its thickness by approximating the internal field by the field that would exist inside an infinite homogeneous slab of the same thickness, orientation, and relative refractive index. Similarly, Karam and Fung (1988) and Seker and Schneider (1988) computed the scattering from long circular cylinders by approximating the internal field using the exact solution for an infinitely long cylinder with the same radius, orientation, and relative refractive index. A surface-field analog of this approximation was developed by Lin and Sarabandi (1995) and was extended to finite hexagonal cylinders by Rother *et al.* (1999) by virtue of computing the surface field for an infinite hexagonal cylinder using the discretized Mie formalism (Rother 1998). Because this approach ignores the contributions from the cylinder's top and bottom, it cannot reproduce such scattering features as the $46°$ halo for circular and hexagonal ice cylinders attributed to the minimal angle of deviation by $90°$ prisms and the strong backscattering enhancement caused by double internal reflections from perpendicular facets (see Fig. 7.6 and Section 10.6).

A similar approach was applied by Kuzmin and Babenko (1981) to the problem of scattering by spherical particles composed of a weakly anisotropic material. They computed the scattered field via Eq. (2.16) by approximating the internal field by that of an "equivalent" isotropic sphere.

Pollack and Cuzzi (1980) developed a semi-empirical theory based on the results of microwave analog measurements by Zerull (1976). They approximated the scattering properties of nonspherical particles with $x < x_0$ using the Lorenz–Mie results for volume-equivalent spheres, where x_0 is a tunable parameter typically close to 5. The absorption cross section for larger nonspherical particles was still computed using the Lorenz–Mie theory, while the phase function was represented as a sum of the Fraunhofer diffraction, the rays reflected from a sphere, and transmitted rays that were fitted to mimic Zerull's measurements by the use of another tunable parameter. Coletti (1984) proposed another semi-empirical theory based on his own optical measurements and similar in some respects to that of Pollack and Cuzzi.

Drossart (1990) proposed a model for calculating the scattering properties of irregular, randomly oriented particles based on modified Lorenz–Mie formulas for volume-equivalent spheres. The underlying assumption of the model is that the ampli-

tude scattering matrix for nonspherical particles can still be described by the Lorenz–Mie equations (5.149)–(5.151), but each summand on the right-hand side of Eqs. (5.149) and (5.151) experiences an independent random phase shift modeled by factors $\exp(i\alpha_n)$ and $\exp(i\beta_n)$ for S_{11} and S_{22}, respectively. An obvious deficiency of this approximation is that Eq. (5.150) is still applied despite the assumption of particle nonsphericity. As a consequence, the model preserves the Lorenz–Mie structure of the Stokes scattering matrix (Eq. (4.49)) and predicts linear and circular depolarization ratios identically equal to zero irrespective of the particle shape. Furthermore, the model does not provide a recipe for choosing the random phase factors based on particle microphysical characteristics.

Latimer (1975) developed several hybrid approximations for spheroids using the Lorenz–Mie theory and assigning an effective sphere radius and relative refractive index depending on the spheroid orientation and axis ratio. Latimer and Barber (1978) examined the accuracy of this approach by comparing its results with those obtained using the exact *T*-matrix method. Grenfell and Warren (1999) approximated the scattering and absorption properties of a long ice cylinder in random orientation using a collection of independent spheres having the same total volume and total surface area as the cylinder.

Further reading

Useful discussions of approximate theories can be found in the books by van de Hulst (1957), Kerker (1969), Bohren and Huffman (1983), Volkovitsky *et al.* (1984), Lopatin and Sid'ko (1988), and Kokhanovsky (1999) as well as in the recent review by Jones (1999). In Markel *et al.* (2000) approximate approaches are used to compute the scattering and absorption properties of smoke clusters.

The physical foundation of the geometrical optics concept of rays is explained in Chapter III of Born and Wolf (1999) and in a book by Kravtsov and Orlov (1990). Associated concepts of caustics and catastrophes are discussed by Marston (1992) and Kravtsov and Orlov (1999). A collection of selected papers on the geometrical theory of diffraction and wave fields near caustics relevant to scattering problems was edited by Marston (1994).

Chapter 8

Measurement techniques

Despite the availability of advanced theoretical techniques, laboratory and *in situ* experiments remain a useful (and sometimes the only) source of information about light scattering by many types of natural and artificial particles. Existing techniques for measuring the electromagnetic scattering characteristics of small particles traditionally fall into two categories:

- the measurement of visible and infrared light scattering by particles with sizes ranging from several hundredths of a micron to several hundred microns;
- the measurement of microwave scattering by millimeter- and centimeter-sized objects.

Measurements in the visible and infrared benefit from the availability of sensitive detectors (photomultipliers and avalanche semiconductor photodiodes), intense sources of radiation (lasers), and high-quality optical elements. They involve relatively cheap and portable instrumentation and in some cases can be performed in the field nearly as well as in the laboratory. By contrast, microwave scattering experiments require more cumbersome and expensive instrumentation and large (and often stationary) measurement facilities but typically provide better control and knowledge of the scatterer's geometrical and physical characteristics.

8.1 Measurements in the visible and infrared

We have mentioned already, in Section 2.6, that many detectors of electromagnetic energy (especially in the visible and infrared spectral regions) are polarization-insensitive, so that the detector response is determined only by the first Stokes pa-

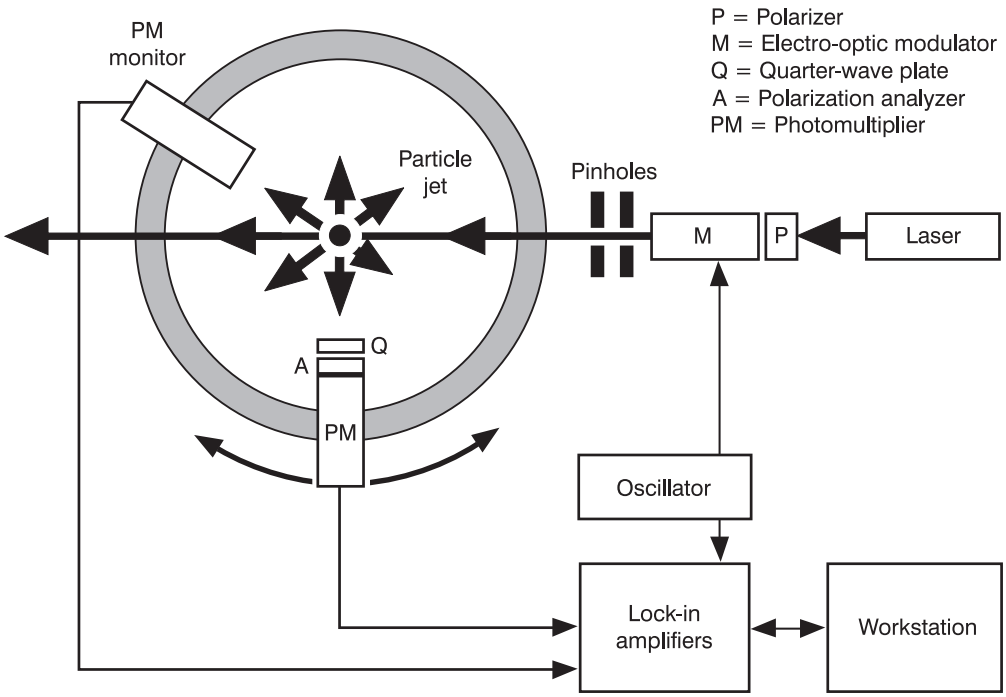

Figure 8.1. Schematic view of an experimental scattering setup using visible or infrared light. (After Hovenier 2000.)

rameter of the beam impinging on the detector. Therefore, in order to measure all elements of the scattering matrix for a particle or a collection of particles, one has to insert into the beam various optical elements that can vary the polarization state of the light, before and after scattering, in a controllable way. In Fig. 8.1, the beam generated by a light source (usually a laser) passes a linear polarizer and a polarization modulator and then illuminates particles contained in a jet stream or a scattering chamber. Light scattered by the particles at an angle Θ passes a quarter-wave plate (optionally) and a polarization analyzer before its intensity is measured by a detector. The Stokes vector of the beam reaching the detector, $\mathbf{I}'$, is given by

$$\mathbf{I}' \propto \mathbf{AQF}(\Theta)\mathbf{MPI} = \mathbf{AQ}N\langle\mathbf{F}(\Theta)\rangle\mathbf{MPI}, \tag{8.1}$$

where $\mathbf{I}$ is the Stokes vector of the beam leaving the light source, $\mathbf{A}$, $\mathbf{Q}$, $\mathbf{M}$, and $\mathbf{P}$ are 4×4 Mueller transformation matrices of the analyzer, quarter-wave plate, modulator, and polarizer, respectively, $\mathbf{F}(\Theta)$ is the total scattering matrix of the particles contributing to the scattered beam, N is the number of the particles, and $\langle\mathbf{F}(\Theta)\rangle$ is the ensemble-averaged scattering matrix per particle. It is implied that the scattering plane serves as the reference frame for defining the Stokes parameters. The Mueller matrices of the polarizer, modulator, quarter-wave plate, and analyzer depend on their orientation with respect to the scattering plane and can be varied precisely. Since the

detector measures only the first element of the Stokes vector $\mathbf{I}'$, several measurements with different orientations of the optical components with respect to the scattering plane are required for full determination of the scattering matrix. In the case of randomly oriented particles with a plane of symmetry and/or in the case of particles and their mirror counterparts in equal numbers and in random orientation, the six independent scattering matrix elements (Eq. (4.7)) can be determined using four different orientation combinations (Kuik *et al.* 1991). This procedure is repeated at different scattering angles in order to determine the angular profile of the scattering matrix.

The accuracy of an experimental setup can be tested by performing measurements for particles with known scattering characteristics such as spherical water droplets (e.g., Muñoz *et al.* 2000a). One can also check the block-diagonal structure of the scattering matrix, Eq. (4.7), which should exist when particles form a macroscopically isotropic and mirror-symmetric medium. Additional tests are provided by the general relationships for the scattering matrix elements (Hovenier and van der Mee 2000).

Early measurements of the scattering matrix used a simple subtraction method that relied on pairs of intensities measured separately with different combinations of polarizing elements; the results were subtracted in order to obtain scattering matrix elements (Pritchard and Elliott 1960; Beardsley 1968; Rozenberg *et al.* 1970). This technique has low accuracy because of the need to determine small differences between two large signals. The measurements of the two large signals are separated in time and this requires one to assume that the sensitivity of the detector and also the scattering sample (e.g., the number N of scattering particles) do not change with time, which is often not the case.

Hunt and Huffman (1973) developed the technique of high-frequency sinusoidal time modulation of the polarization of the light before it is scattered (Fig. 8.1), combined with intensity normalization. Followed by lock-in detection, this technique improves the measurement accuracy by enabling direct measurements of the scattering matrix elements normalized by the (1, 1) element of the matrix and yields the capability to determine several elements from only one detected signal. Advanced experimental setups based on this technique have been described by Bickel *et al.* (1976), Thompson (1978), Thompson *et al.* (1980), Anderson (1992), Kuik (1992), Hovenier (2000), and Kaplan *et al.* (2000).

A major advantage of measurements at visible and infrared wavelengths is that they can deal with real particle ensembles. However, they often suffer from the lack of accurate independent characterization of the particle size and shape distribution and relative refractive index, thereby making comparisons of experimental and theoretical results difficult. The number of particles N contributing to the scattered beam is also seldom known, which precludes the absolute measurement of the (1, 1) element of the ensemble-averaged scattering matrix per particle $\langle \mathbf{F}(\Theta) \rangle$ (measurements of elements other than the (1, 1) element are usually reported in the form of N-independent ratios of the elements to the (1, 1) element). Another drawback is that the arrangement of the source of light and the detector usually precludes measurements at scattering angles close to 0° and 180° (although it is possible to add a

backscattering measurement capability using a beam splitter). For example, the setup described by Hovenier (2000) has the range of scattering angles $[5°, 175°]$. This makes problematic absolute measurement of the phase function by means of satisfying the normalization condition of Eq. (4.53). As a consequence, experimental phase functions are often normalized to the value at a fixed scattering angle. An alternative way of presenting experimentally determined phase functions is to assume that the phase-function value at the smallest scattering angle available is the same as for volume- or surface-equivalent spheres. This approach may or may not be accurate, depending on the (often unknown) validity of the underlying assumption.

The error in determining the scattering cross section per particle by integrating the scattered intensities over all scattering angles also relies on a knowledge of N and depends on how much of the forward- and back-scattered energy is not detected (Anderson *et al.* 1996; Heintzenberg and Charlson 1996; Rosen *et al.* 1997). As discussed in Section 7.4, the phase function of particles larger than the wavelength of the incident light has a strong and narrow diffraction peak that may contain more than 50% of the total scattered energy (Figs. 7.3 and 7.4 and Eqs. (7.13)–7.15)). This factor alone can cause errors exceeding 50% in the measured scattering cross section.

The extinction cross section is often determined by measuring the attenuation of the directly transmitted beam. Specifically, the extinction cross section is proportional to the difference in the readings of detector 1 in Fig. 2.3 corresponding to the situations without and with the particle(s) interposed between the source of light and the detector (Sections 2.8 and 3.1). This measurement unavoidably suffers from the problem that a detector with a finite angular aperture picks up some of the light *scattered* by the particle(s) in the forward direction. Depending on the average particle size and thus the magnitude and angular width of the diffraction component of the phase function (Fig. 7.3), the extinction can be underestimated by as much as a factor of 2. Indeed, we saw in Section 7.4 that, for particles larger than the wavelength, the scattering cross section due to the diffraction peak is equal to the area of the particle's projection on the plane perpendicular to the incidence direction, Eq. (7.14), and, thus, is equal to one-half of the extinction cross section, Eq. (7.12). If the detector picks all the energy contained in the narrow diffraction cone, then the energy removed by the particle from the incident beam and thus the extinction cross section will be underestimated by 50%. Therefore, if a detector is to measure accurately the full extinction by particles with size parameters $x \gg 1$ then its acceptance angle must be much smaller than $7/x$, say less than $1/(2x)$ (see Fig. 7.3). Correction for the diffraction contamination is possible if the average particle projection is known and is large, but this is not always the case. With significant potential errors in the extinction and scattering cross sections, little may be said about the difference between the former and the latter, i.e., the absorption cross section, or about the ratio of the latter to the former, i.e., the single-scattering albedo, Eqs. (2.161) and (2.162).

Ashkin and Dziedzic (1980) obtained direct backscatter measurements by using the optical levitation technique, which involved the suspension of particles by light

pressure from the source laser beam alone. An instrument specifically designed for remote sensing measurements at the exact backscattering direction is a lidar, built of a pointing laser emitting a powerful beam and a receiving telescope–detector combination affixed to the laser (Sassen 2000). The laser beam is usually polarized either linearly $(P = 1,\ V = 0)$ or circularly $(P = 1,\ V = \pm I)$. The laser light scattered by aerosol and cloud particles is collected by the telescope, and its intensity and polarization characteristics are precisely measured. Since lidars measure backscattering from particles located at large distances (hundreds and thousands of meters) from the instrument, the scattering angle can be made arbitrarily close to 180°. Important quantities measured by a polarization lidar are the so-called linear and circular depolarization ratios. Because both ratios must vanish for spherically symmetric scatterers, the detection of non-zero ratios may directly indicate the presence of nonspherical particles (see Sections 10.2 and 10.11).

Early scattering experiments used unpolarized incident light and were limited to measurements of the scattered intensity and the degree of linear polarization (Hodkinson 1963; Napper and Ottewill 1963). The first measurements of other elements of the scattering matrix were performed using the simple subtraction method. The development of the polarization modulation technique resulted in a number of accurate measurements of the complete scattering matrix. The results of extensive measurements using visible and infrared light were reviewed by Hoekstra and Sloot (2000), Mishchenko *et al.* (2000c), and Quinby-Hunt *et al.* (2000). Among more recent results, we note measurements of the scattering matrix for iron oxide ellipsoids and latex sphere suspensions (Kaplan *et al.* 1999, 2000), rutile particles in water (Volten *et al.* 1999), olivine and Allende meteorite particles (Muñoz *et al.* 2000a), ice crystals (Bacon and Swanson 2000), various mineral aerosols (Volten 2001; Volten *et al.* 2001), and fly ash and clay particles (Muñoz *et al.* 2000b, 2001). Worms *et al.* (2000) measured the degree of linear polarization for various scattering samples under microgravity conditions. Card and Jones (1999a,b) investigated the potential of measuring polarized light scattering for characterization of irregular particles. Tavker and Kumar (2000) performed laboratory measurements of the linear depolarization ratio for artificial crystallized H_2O/H_2SO_4 acid clouds. Gerber *et al.* (2000) and Garrett *et al.* (2001) used a so-called cloud integrating nephelometer to measure the asymmetry parameter for water droplet and ice crystal clouds. Wurm *et al.* (2000) measured the intensity and polarization of light scattered by laboratory-generated dust aggregates consisting of micrometer-sized components. Barkey and Liou (2001) reported measurements of the phase function of laboratory-generated water microdroplets and ice crystals using a portable lightweight nephelometer specifically designed for deployment on a balloon-borne platform in cirrus cloud conditions.

To demonstrate the particle-characterization potential of measurements using visible light, we show in Fig. 8.2 laboratory results for the phase function $a_1(\Theta)$ and the ratio $b_1(\Theta)/a_1(\Theta)$ at two wavelengths (442 and 633 nm) measured for an artificial cloud of spherical water droplets with a refractive index m = 1.33 relative to that of

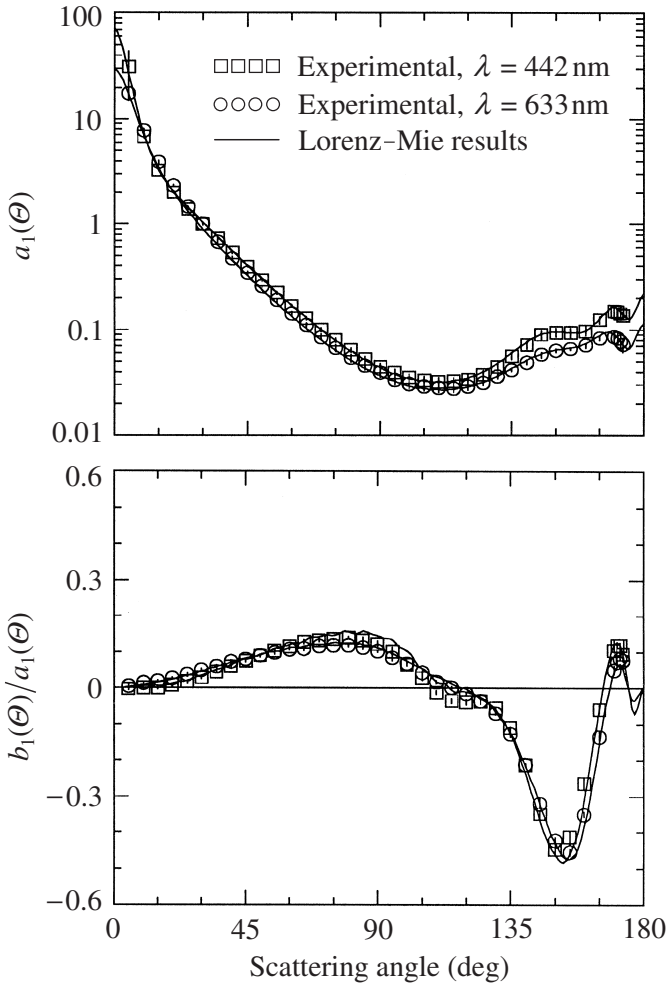

Figure 8.2. The phase function $a_1(\Theta)$ and the ratio $b_1(\Theta)/a_1(\Theta)$ measured by Muñoz *et al.* (2000a) for an artificial cloud of spherical water droplets at two wavelengths. The solid curves show the results of Lorenz–Mie computations for a log normal size distribution of water spheres, with effective radius and effective variance chosen such that they minimize the differences between the measured and calculated scattering matrix elements as functions of scattering angle.

air. The experimental phase functions are normalized to unity at $\Theta = 30°$. Measurement errors (shown by vertical error bars) are negligibly small at most scattering angles. The laboratory results are compared with the results of Lorenz–Mie calculations for a log normal size distribution, Eq. (5.243), the parameters r_g and σ_g being chosen such that the effective radius and effective variance of the distribution, Eqs. (5.248) and (5.249), are $r_{\text{eff}} = 1.1\,\mu\text{m}$ and $v_{\text{eff}} = 0.3$, respectively. These values were found to minimize the differences between the measured and calculated scattering matrix elements as functions of scattering angle. Clearly, the quantitative agreement between the measurements and the calculations is good over the entire scattering an-

gle range. The remaining differences may be due to the fact that the actual size distribution deviated somewhat from the assumed log normal distribution.

Knowledge of the scattering matrix provides a complete characterization of the angular distribution and polarization state of the scattered light for spherically symmetric or randomly oriented particles. However, averaging over orientations reduces the potential information content of the scattered light by smoothing out specific features generated by a nonspherical particle having a fixed orientation relative to the incidence and scattering directions. Therefore, several attempts have been made recently to measure the intensity of the scattered light for single nonspherical particles in a fixed orientation as a function of both the zenith and the azimuth angle and to assess the particle characterization potential of such measurements (Hirst *et al.* 1994, 2001; Hirst and Kaye 1996; Kaye *et al.* 1996, 1997; Holler *et al.* 1998, 1999, 2000; Sachweh *et al.* 1999; Borovoi *et al.* 2000; Secker *et al.* 2000; Videen *et al.* 2000a). Plate 8.1 shows four examples of two-dimensional angular scattering measurements for the case of laser light incident along the positive direction of the x-axis (cf. Fig. 1.2). The measurements show a distinctive irregular patchy structure, with the patch density per solid angle increasing with cluster diameter. Although the amount of information contained in such two-dimensional angular scattering patterns may often be overwhelming and may be difficult to interpret definitively, this technique appears to be a promising particle characterization tool and should be pursued further. An obvious improvement would be measurement of the polarization state as well as the intensity of the scattered light.

8.2 Microwave measurements

Measurements of scattering properties of millimeter- and centimeter-sized objects at microwave frequencies are important for such applications as the remote sensing of precipitation and communication technology (Oguchi 1983; Aydin 2000; Haferman 2000). In addition, the scale invariance rule (subsection 5.8.2) states that particle size in the theoretical formulation of electromagnetic scattering is only encountered as a ratio to the wavelength as long as one deals with dimensionless scattering and absorption characteristics. Therefore, the strategy of the microwave analog technique is to manufacture a centimeter-sized scattering object with the desired shape and relative refractive index, study the scattering of a microwave beam by this object, and finally extrapolate the results to other wavelengths (e.g., visible or infrared) by keeping the ratio of size to wavelength fixed (Greenberg *et al.* 1961; Lind *et al.* 1965).

In a modern microwave scattering setup, radiation from a transmitting conical horn antenna passes through a collimating lens and a polarizer (see Fig. 8.3). The lens produces a nearly flat wave front, which is scattered by an analog particle model target. The scattered wave passes through another polarizer and lens and is measured by a receiving horn antenna. The receiver end of the setup can be positioned at any

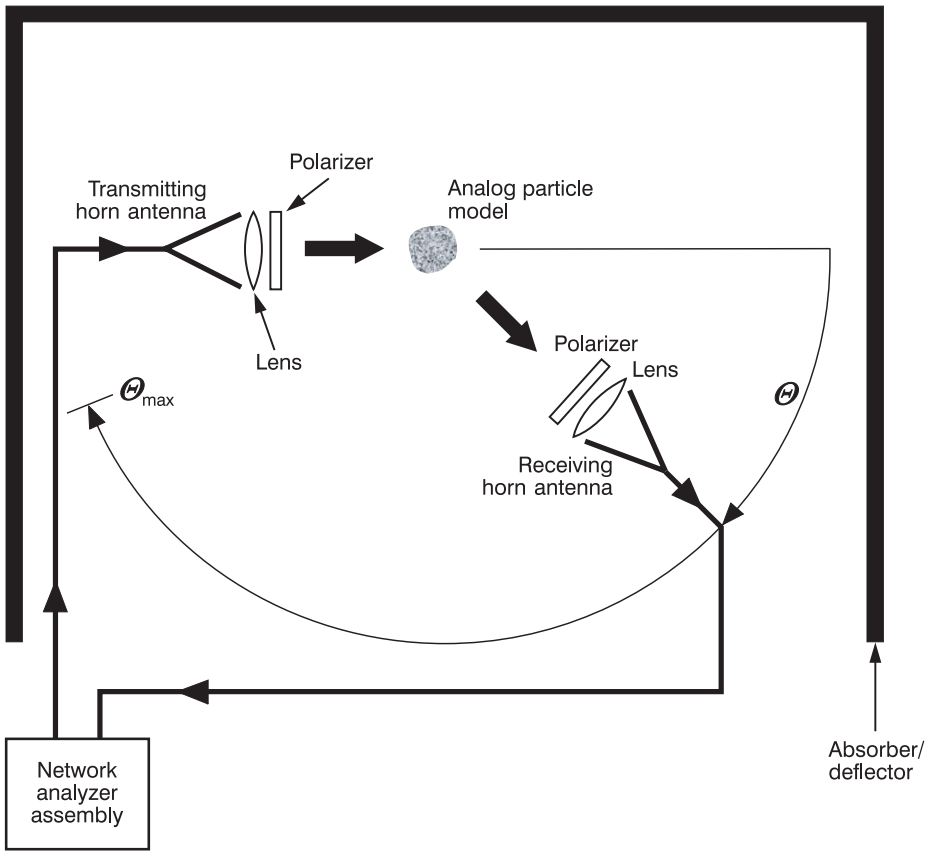

Figure 8.3. Layout of an advanced microwave analog facility. (After Gustafson 2000.)

scattering angle from $0°$ to $\Theta_{max} \cong 170°$, thereby providing measurements of the angular distribution of the scattered radiation. By precisely varying the orientations of the two polarizers, one can measure all elements of the scattering matrix. Detailed discussions of various experimental aspects of the microwave analog technique have been provided by Gustafson (1996, 2000).

Microwave measurements allow coverage of a wide range of scattering angles, including the exact forward direction, and a much greater degree of control over the target size, shape, and orientation than optical or infrared measurements. Using special techniques, even the extinction cross section (or, more generally, the extinction matrix) can be measured. Measurements at angles close to the backscattering direction are usually problematic because the transmitting and receiving antennas would overlap. It is possible, however, to add a backscattering measurement capability ($\Theta = 180°$) by using the transmitting antenna as a receiver. Because the size of the scattering object is typically of the order of centimeters for microwave analog measurements, high-precision target manufacturing is easy and can involve computer-controlled milling or stereo lithography. Therefore, the results of controlled laboratory measurements at microwave frequencies can be compared with theory easily. A

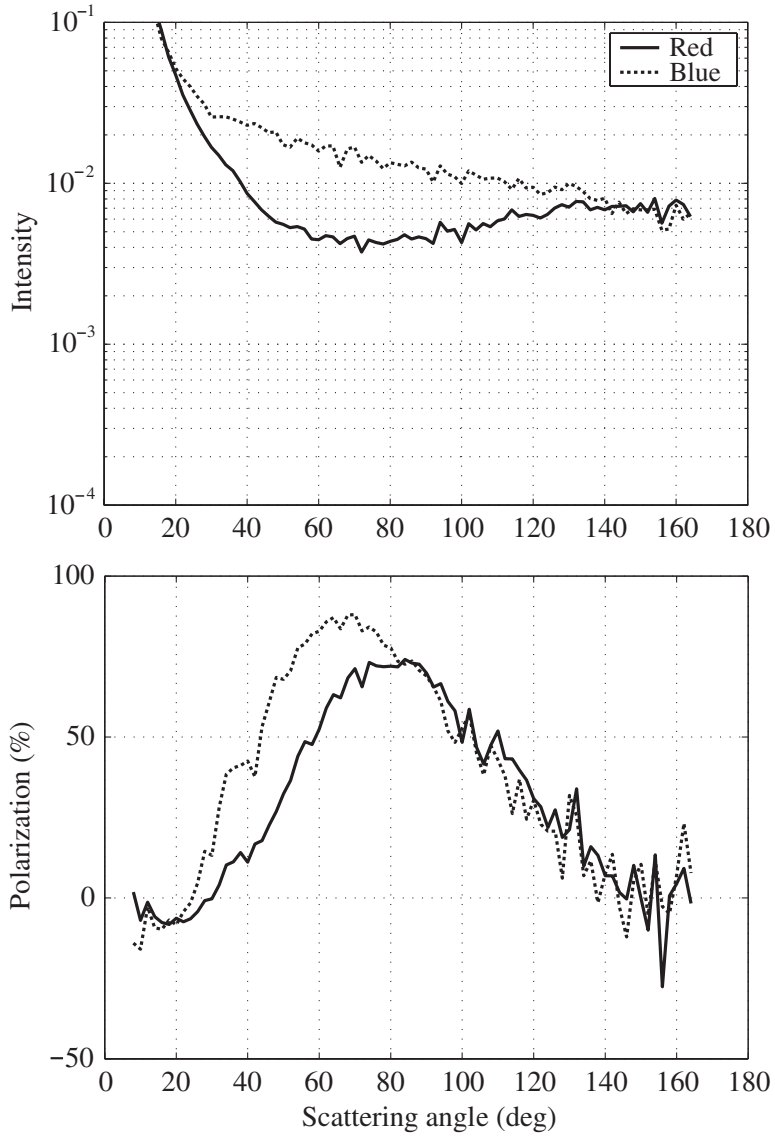

Figure 8.4. Microwave analog measurements of the scattered intensity (in arbitrary units) and the degree of linear polarization for a thin acrylic plate in random orientation (from Waldemarsson and Gustafson 2000). The diameter of the plate is 50.8 mm, the thickness is 1.52 mm, and the relative refractive index is 1.62 + i0.003. The broken and solid curves correspond to the wavelength intervals 2.7–3.0 mm and 3.5–4.0 mm, respectively.

disadvantage of microwave measurements is that they can be performed only for one particle size, shape, and orientation at a time, thereby making ensemble averaging a time-consuming procedure.

Although the microwave analog technique was introduced several decades ago, the complexity and the high cost of the equipment involved have limited the number of operating experimental facilities to only a few. Publications reporting and analyz-

ing the results of microwave analog measurements have been reviewed by Gustafson (2000) and Mishchenko *et al.* (2000c). Recent results include a laboratory comparison of the backscattering ability of raindrops and ice particles (Qingan *et al.* 1998), a systematic experimental study of the angular and wavelength dependence of the intensity and polarization of light scattered by aggregated particles (Gustafson and Kolokolova 1999), laboratory measurements of the polarimetric radar signatures of spherical and spheroidal water droplets at 30GHz (Tazaki *et al.* 2000), and the use of microwave analog measurements for heterogeneous objects in testing the validity of various effective-medium theories (Kolokolova and Gustafson 2001).

Figure 8.4 gives an example of microwave analog measurements. The scattered intensity and the degree of linear polarization $P_Q = -b_1(\Theta)/a_1(\Theta)$ are shown for unpolarized light incident on a thin acrylic plate in random orientation (Waldemarsson and Gustafson 2000). The diameter of the plate is 50.8 mm, the thickness is 1.52 mm, and the relative refractive index is 1.62 + i0.003. The total number of orientations used to simulate the uniform orientation distribution was 1620 and the tilt angle between the normal to the plane facets of the plate and the spin axis was varied in 10° steps. Measurement results were averaged over the wavelength intervals 2.7–3.0 mm and 3.5–4.0 mm. The experiment was designed to model the scattering of unpolarized visible light by randomly oriented silicate flakes with diameter 8 μm and thickness 0.25 μm in the wavelength intervals 0.44–0.49 μm ("blue") and 0.57–0.65 μm ("red"). The fine structure in the curves is mostly due to the limited number of orientations used in the ensemble averaging. The implications of these laboratory results will be discussed in Section 10.4.

Radars form a special class of instruments providing active polarization measurements for remote targets at microwave and radiowave frequencies. Monostatic radars use the same antenna to transmit and receive electromagnetic waves and are limited to measurements at the exact backscattering direction ($\Theta = 180°$). Bistatic lidars use one or more additional receiving antennas, which provide supplementary information for other scattering angles. Remote sensing applications of the radar technique have been reviewed by Aydin (2000) and Bringi and Chandrasekar (2001).